

Investigation of Nonclassical Gasdynamic Effects in Power Generation Applications

N.B.Chandrasekaran

Technische Universiteit Delft



INVESTIGATION OF NONCLASSICAL GASDYNAMIC EFFECTS IN POWER GENERATION APPLICATIONS

by

N.B.Chandrasekaran

in partial fulfillment of the requirements for the degree of

Master of Science

in Aerospace engineering

at the Delft University of Technology,

to be defended on Friday May 19, 2017 at 10:00 AM.

Supervisor: Dr. ir. C. Lettieri
Thesis committee: Prof. dr. ir. P. Colonna di Paliano
Dr. ir. C. Lettieri
Dr. ir. A. K. Sahai

An electronic version of this thesis is available at <http://repository.tudelft.nl/>.

PREFACE

This thesis is submitted in partial fulfilment of the requirements for the degree of Master of Science in Aerospace Engineering in the Flight Performance and Propulsion track from TU Delft. Over the past year, I have had the opportunity to work with a lot of people whose guidance and support have helped me successfully complete my thesis work. I would like to take this opportunity to express my thanks to all of them.

I extend my sincere thanks to Prof. Claudio Lettieri for supervising me on my thesis work and for introducing me to the promising field of non-ideal compressible fluid dynamics. I owe it to you for showing me how to perform a proper research work. I'm confident that the research skills that I gained during this thesis would help me a lot in the future. It is with your constant guidance and motivation that I have been able to bring this project to a successful end.

I would like to thank Prof. Pierro Colonna for taking time off his busy schedule to meet with me at various points during my thesis and for providing me with valuable advice and guidance. I would also like to thank Adam Head for helping me setup FluidProp and for providing me with valuable inputs on my CFD simulations. Thank you very much for taking the time to clear my doubts though you were busy with your Ph.D. work.

Most importantly, I must thank my family from the bottom of my heart for their unconditional love and support during my studies here at Delft. It is because of them that I am in this position today. I also wish to thank all my friends I made at TU Delft for staying with me through thick and thin and for supporting me during my studies. I shall always relish the wonderful memories that I get to share with you people.

*N.B.Chandrasekaran
Delft*

ABSTRACT

The global energy demand is expected to double over the next 20 years. At present, nearly one-third of the total energy that is produced is consumed by the industrial sector of which nearly 20% to 50% is lost as waste heat in the form of hot exhaust gases or cooling water. Energy-related CO₂ emissions reached an all-time high of 32 gigatonnes in 2014 and is expected to increase by more than 70% over the next two decades. The need for the future, therefore, is to not only achieve a higher energy efficiency but also to tackle the problem of greenhouse gas emissions. Waste heat recovery (WHR) systems provide an attractive opportunity as an emission free and an efficient energy source. The non-ideal behaviour of the working fluids commonly employed in these systems in the thermodynamic conditions close to saturation can lead to performance issues making the design of turbomachinery for WHR power systems challenging. It is, therefore, necessary to characterize the internal flow behaviour of such systems so as to improve their performance and stability.

The current research aims to verify the existence of non-ideal compressible fluid dynamic (NICFD) behaviour by demonstrating the formation of an expansion shock wave in the flows of molecularly complex fluids. The experiment would be performed in the Flexible Asymmetric Shock Tube (FAST), a novel Ludwig tube-type facility designed to study the propagation of waves in the dense vapours of organic fluids. The experimental setup adopts a fast opening valve (FOV) to achieve reliable and repeatable wave formation. There is little data available in the literature about the characteristics of the FOV such as its opening time and breaching velocity. The goal of this research work is to characterize the motion of the FOV in order to ensure the formation of rarefaction shock waves in the FAST setup.

In order to achieve the objectives of this research work, a two-pronged approach was followed: an analytical model to estimate the flow properties across a normal shock wave in the test fluid was developed which can guide the numerical and experimental studies. A one-dimensional model of the FOV motion was developed in parallel so as to estimate the opening time and velocity of this driver. The FOV motion obtained from the 1D model was implemented in 2D CFD simulations to study the effect of FOV motion on the flow behaviour and shock formation.

Based on the results of the analytical model, it was concluded that the experimental initial condition was within the non-classical thermodynamic regime of the working fluid. The 1D model of the conceptual design of the FOV however predicted an opening time of 18.13 ms which is more than three times the proposed opening time of 5 ms for the FOV design. The presence of an auxiliary bellow in the FOV design that blocked the gas exhaust from the primary bellow was found to cause the increased opening time. CFD simulations were performed for the cases of a diaphragm-like expansion and the FOV opening times of 5 ms and 18.13 ms. From the results, it was observed that for the case of the diaphragm-like expansion, a single reliable rarefaction shock wave was observed at the first pressure transducer pair on the test rig. For both the FOV cases, more than a single shock front with multiple trailing expansion waves were observed unlike the diaphragm-like expansion. The multiple waves disappeared when the CFL number of the simulation was increased from 0.68 to a value close to 1. This result is counter-intuitive as the accuracy of a numerical simulation increases as the CFL is decreased below 1. This result suggests that further analysis is required to identify the best possible spatial and temporal resolution for the simulation so as to obtain the desired results.

CONTENTS

Preface	iii
List of Figures	ix
List of Tables	xv
Nomenclature	xvii
1 Introduction	1
1.1 Background	1
1.2 Need for Research	2
1.3 Motivation and Thesis Objective	3
1.4 Goals of the Thesis	3
1.5 Research Questions	4
1.6 Contributions of the Thesis	4
1.7 Thesis Outline	4
2 Non-ideal Compressible Fluid Dynamics	7
2.1 Fundamental Derivative of Gasdynamics	7
2.2 Admissibility region for Rarefaction shock waves	9
2.3 Summary	12
3 Experimental Test Rig	13
3.1 Flexible Asymmetric Shock Tube	13
3.2 Outline of FAST Experiment	13
3.3 Diaphragmless Shock Tube Driver	15
3.3.1 FAST Diaphragmless Shock Tube Driver	16
3.3.2 Los Alamos National Laboratory Driver	17
3.3.3 Bellows-actuated Shock Tube Driver	19
3.3.4 New FOV for FAST - Concept Design	20
3.4 Summary	22
4 Analytical Modelling of Normal Shocks in Non-Ideal Flows	23
4.1 Real Gas Thermodynamics	23
4.1.1 Compressibility Factor	23
4.1.2 Caloric Equation of State	24
4.1.3 Isentropic Coefficient	24
4.2 Analytical Model for Normal Shocks in Real Gas Flows	25
4.3 Analytical Model for Real Gasdynamic Flows	27
4.4 Summary	27

5	Modelling of FOV Motion	31
5.1	Modelling Driver Performance	31
5.2	Model Assumptions	35
5.3	Effect of Piston Motion on Charge Tube Pressure	35
5.4	Estimation of Opening Time	36
5.5	Performance Evaluation of FOV Design	36
5.6	Effect of β_d on FOV Opening Time	39
5.7	Summary	42
6	Computational Modelling of the Fast Opening Valve	43
6.1	Reynold's Averaged Navier-Stokes Equation	43
6.2	Turbulence Modelling	44
6.3	CFD Simulation Setup	45
6.3.1	Geometry	45
6.3.2	Meshing	47
6.3.3	Solver	47
6.3.4	Problem Setup	47
6.3.5	Mesh Motion and Remeshing	48
6.4	Sensitivity Analysis	49
6.4.1	Geometry Sensitivity	49
6.4.2	Mesh Sensitivity	50
6.5	Summary	51
7	Assessment of the CFD Results	53
7.1	Diaphragm-like Expansion in D6	53
7.2	Effect of FOV motion on shock formation	55
7.3	Summary	64
8	Summary and Recommendations	65
8.1	Thesis Summary	65
8.2	Recommendations for the Future	66
	Bibliography	67
A	Flexible Asymmetric Shock Tube (FAST) User Manual	71
A.1	Charging the rig with the test fluid	71
A.2	Setting Initial Conditions - Cold Startup	73
A.3	Setting Initial Conditions - Hot Startup	74
A.4	Running a Gasdynamic Test	75
A.5	Discharging of the Setup	76

LIST OF FIGURES

1.1	Contours of Mach number showing supersonic expansion of siloxane fluid MDM in a converging-diverging nozzle close to the saturation curve. The impact of the fundamental derivative on supersonic turbomachinery designs is clearly evident in the difference between the nozzle geometries obtained when using an ideal (bottom) and a real (top) gas	2
1.2	Road map of the current thesis	5
2.1	Liquid Vapour Saturation curve and negative Γ region for a BZT fluid	8
2.2	Wave propagation in the classical and nonclassical regimes. In classical dynamics, when $\Gamma > 0$, compression waves coalesce to form a compression shock wave. In NICFD with $\Gamma < 0$, a RSW is formed. A special case is when $\Gamma = 0$ where the wave propagates unaltered	9
2.3	P-v plot showing the shock adiabat and Rayleigh lines for three cases: Only a shock wave of the expansive type is allowed between states 1 and 2 since the Rayleigh line lies completely below the adiabat. However, from state 3 to 4, a compression shock can exist in the flow while expansion waves flatten out. The expansion from 1 to 5 shows the limiting case when the Rayleigh line is tangential to the adiabat. For this condition, the shock is said to be sonic, i.e., both initial and final states have $M = 1$	11
3.1	Side-view of FAST setup showing the key geometrical components. Once the FOV is opened, the high-pressure gas in the CT accelerates via the nozzle and expands into the reservoir. Consequently, an expansion wave starts to propagate into the CT that might develop into a RSW upstream. The speed of the RSW formed in the CT is measured using the pair of pressure probes located on the walls of the CT.	14
3.2	Flexible Asymmetric Shock Tube setup commissioned at TU Delft	14
3.3	Schematic of different driver designs. a) Piston b) Piston with lip c) Piston with plug d) Sleeve	16
3.4	Schematic of cross-section of Fast Opening Valve	17
3.5	Schematic of LANL driver showing its three-staged opening motion (a) The main chamber pressure is increased to $p_{4,0}$ (b) The auxiliary chamber is evacuated through the pressure inlet/outlet. The auxiliary bellows move upwards as a result clearing the vents (c) The back-pressure p_5 releases through the vents creating a pressure imbalance across the barrier element. The main chamber and the lower intermediate chamber pressure (p_4 & p_6) thereby pushes the plug-sliding sleeve system away from the driven section till the sliding sleeve is stopped at the top of the back chamber (d) The upper intermediate chamber pressure (p_7) continues to push the piston upwards till it breaches and the main chamber pressure exhausts into the driven section.	18
3.6	Schematic of Bellow-actuated diaphragmless shock tube driver. When the bellow is pressurized with gas, the seal plate attached to the shaft seals the opening to the driven section. The seal plate is pulled away from the opening when the bellows are vented thereby allowing the high pressure gas to expand into the driven section.	20
3.7	Conceptual design of a new Fast Opening Valve for the FAST experimental setup	21

3.8	Schematic of different driver designs. a) Piston b) Piston with lip c) Piston with plug d) Sleeve	21
4.1	Contours of Γ shown in the P-v plot for D_6 with the expansion process denoted by the Hugoniot and the Rayleigh lines. The $\Gamma = 0$ line is shown in dotted lines.	28
4.2	Close-up of the Hugoniot and Rayleigh lines connecting the pre-shock and post-shock states. The Rayleigh line completely lies below the shock adiabat. Also the Rayleigh line is tangent to the adiabat in the downstream state indicating a sonic post-shock state.	28
4.3	Flow-chart of the analytical gasdynamic model	29
5.1	Cross-sectional view of the new Fast Opening Valve design showing key dimensions	32
5.2	Expansion wave caused by motion of piston in a tube. As the piston accelerates within the tube, the gas expands to fill in the space occupied by the piston creating a series of expansion waves that propagate into the tube ahead of the final shock wave	36
5.3	(Left) Initial and (Right) Breaching position of the FAST FOV driver	37
5.4	Definition of opening time for FAST FOV - time taken for the FOV to move from $x = 0$ till a distance equal to D from the breaching position	37
5.5	Displacement and velocity curves for the New FOV Design	38
5.6	Drop in pressure and temperature across expansion wave generated by initial piston motion	38
5.7	Schematic of the effect of auxiliary bellow on the exhaust of the primary bellow; As long as $\Delta x \leq \phi_{e,p}$, the rate of Helium exhausted into the LPP will be governed by the gap between the bellows.	38
5.8	Variation of the FOV displacement with time for various auxiliary bellow β_d . Given the limiting value of β_d is 0.5, these curves indicate that the exhaust diameter of the auxiliary bellow can be increased further to reduce the FOV opening time.	39
5.9	Variation of the FOV velocity with time for various auxiliary bellow β_d . Similar to the displacement curves, increasing the β_d value of the auxiliary bellow effectively displaces the curves to the left of the time axis while keeping the shape of the curve the same.	40
5.10	Variation of the FOV velocity with time for various primary bellow β_d . Unlike the auxiliary bellow, increasing the β_d of the primary bellow increases the velocity of the FOV. The time axis is normalized with the proposed design opening time of 5 ms and the displacement is normalized using the opening distance of 0.109 m.	41
5.11	Variation of the FOV velocity with time for various primary bellow β_d . Similar to the displacement profile, the FOV acceleration increases with increasing primary bellow β_d . The time axis is normalized using the proposed design opening time of 5 ms and the velocity axis is normalized by the maximum velocity of the design FOV motion.	41
5.12	Effect of the exhaust diameters of the primary and auxiliary bellows on the FOV opening time. Due to the design β_d of the primary bellow already being equal to the limiting value, it has little influence on the opening time of the FOV while increasing the auxiliary bellow exhaust diameter can effectively reduce the opening time by nearly 20%.	42
6.1	Schematic of FAST geometry with characteristic dimensions	46
6.2	Schematic of actual (left) and modelled (right) LPP geometries. The curved walls of the LPP result in the generation of poor quality meshes during mesh motion making its use unsuitable.	46
6.3	Schematic of FAST geometry showing the boundary conditions defined for the simulation.	48
6.4	Schematic of the actual position (left) and the modelled position (right) of the FOV during initialization in the FAST setup	49

6.5	(Left) CT-throat interface at which the pressures are measured and (Right) Results of the geometry sensitivity study for the straight-walled and curve-walled LPP geometries at the CT-throat interface	50
6.6	(Left) Calculation of the slope of the shock wave (left) and Results of the mesh sensitivity study for various mesh sizes comparing the shock slope (right)	50
7.1	Schematic of the CT showing the wave propagation past the pressure transducers. The wave speed is calculated by dividing the distance between the sensors by the time taken for the wave to travel that length. This is done for every point at a given pressure along the wave to obtain the local wave propagation speed.	54
7.2	Profiles of pressure measured at sensors PT1 and PT2 for the diaphragm-like expansion case. The red and black line overlays depict the nonclassical part of the expansion wave. The wave speed is measured by dividing the axial distance between the two sensors by the time taken for the wave to travel from PT1 to PT2. The time axis is normalized by the mean time taken for the wave to travel between the sensors and the pressure is normalized by the charge tube pressure	54
7.3	Variation of the wave speed with the drop in pressure across the expansion wave for a diaphragm-like expansion. The black dots signify the region of negative Γ . The wave speed is normalized by the local speed of sound in the fluid at rest in the CT.	55
7.4	(Left) Propagation of the shock wave from the throat to the CT shown at $t = 1.8$ ms. The sudden change in diameter between the two sections causes a part of the wave to diffract while the section close to the centre-line continues to propagate normal to the CT axis (Right) Reflection of the diffracted portion of the wave at the CT walls shown at $t = 3.6$ ms. The reflected waves create a system of oblique compression and rarefaction waves behind the leading shock wave. The contours shown here are for the upper-half section of the CT.	56
7.5	Flow field in the upper-half of the CT behind the leading RSW at $t = 5$ ms showing the system of compression and rarefaction waves symmetric about the axis that is created by the reflection of the diffracted portion of the initial expansion shock at the walls.	56
7.6	Pressure drop across the expansion wave in the CT shown at $t = 5$ ms. The oscillations observed in the post-shock pressure value occur due to the rarefaction/compression wave pattern created by the reflection of the diffracted initial wave at the CT walls.	56
7.7	Pressure contours of flow in the upper half-section of the charge tube for the diaphragm-like expansion case. The rarefaction shock wave is clearly seen as discontinuity between the high pressure (red) and low pressure (blue) regions in the tube.	57
7.8	Profiles of pressure measured at sensors PT1 and PT2 for a FOV opening time of 18.13 ms. The red and black line overlays depict the $\Gamma < 0$ part of the wave. Unlike the diaphragm-like case where the pressure variation across the wave is smooth, the drop in pressure is staggered in this case with successive expansion waves in the CT denoted by the sudden jumps in pressure. The time axis is normalized by the mean time taken for the wave to travel between the sensors and the pressure is normalized by the charge tube pressure	57
7.9	Variation of wave speed with the drop in pressure across the expansion wave for the opening time of 18.13 ms. Here, two regions of flatness can be observed signifying the presence of two RSWs in the flow	58

7.10 Pressure contours of flow in the charge tube for the FOV opening time of 18.13 ms. Unlike the diaphragm-like expansion case, a discernible rarefaction shock is not formed in this run but instead series of expansion waves are seen to propagate into the CT. It can be seen from the wave speed vs. pressure drop plot that the first two waves are supersonic.	58
7.11 Profiles of pressure measured at sensors PT1 and PT2 for a FOV opening time of 5 ms with the red and black lines depicting the $\Gamma < 0$ part of the wave. The presence of multiple waves even in this case indicates that these are not the effect of the large opening time of the FOV. The time axis is normalized by the mean time taken for the wave to travel between the sensors and the pressure is normalized by the charge tube pressure	59
7.12 Variation of wave speed with the drop in pressure across the expansion wave for a 5 ms opening time. Three RSWs can be observed in this plot as opposed to the two for the case of the 18.13 ms opening time.	59
7.13 Pressure contours of flow in the charge tube for the FOV opening time of 5 ms. Similar to the 18 ms case, a series of expansion waves can be seen propagating into the CT with the first three waves being supersonic.	60
7.14 Schematic of the simple shock tube geometry that is used to study the reason for the formation of multiple shock waves. The diameter of the shock tube is 0.04 m with $L/D = 50$ and $d/D = 0.6$. The initial temperature and pressure of the fluid are the same as the FAST experiment.	60
7.15 Comparison of the shock tube flow close to the diaphragm in (Left) D_6 (Case 1) and (Right) an ideal gas. In both cases, the initial wavefronts can be seen to split into diffracted and normal portions at the diaphragm edges. The image is shown here only for a qualitative comparison of the flow field. The time instants of the two contours are not the same.	61
7.16 Comparison of the shock tube flow sufficiently far from the diaphragm in (Left) D_6 (Case 1) and (Right) an ideal gas. The flow field is similar in both the cases with a leading shock wave followed by a system of compression-rarefaction waves. The image is shown here only for a qualitative comparison of the flow field. The time instants of the two contours are not the same.	61
7.17 Comparison of the pressure contours of Cases 1 & 2 in the simple shock tube. The formation of multiple waves can be observed in the contours of Case 1 while a single expansion shock wave is seen in Case 2.	61
7.18 Profiles of pressure across the expansion wave for Cases 1 & 2 at time instants (Left) 2.5 ms and (Right) 4.2 ms. The variation between the two pressure profiles across the wave can be seen to gradually evolve with time. It should be noted that the pressure readings behind the wave are in good accordance with each other.	62
7.19 Profiles of pressure across the expansion wave for Cases 1 & 2 at time instants (Left) 6 ms and (Right) 8 ms. The expansion wave of Case 1 gradually begins to split into multiple waves which can be observed as steps in the pressure profile. On the other hand, a smooth drop in pressure is seen across the wave of Case 2.	62
7.20 Comparison of the pressure contours of Cases 2 & 3 in the simple shock tube. Multiple expansion waves that were clearly visible in the contours of Case 1 are absent in Case 3 and are very similar to that of Case 1 with a single discernible expansion shock wave.	63
7.21 Profiles of pressure across the expansion wave for Cases 1 & 3 at time instants (Left) 2.5 ms and (Right) 4.2 ms. The similarity of the pressure profile of Case 3 to that of Case 2 suggests that the multiple expansion waves vanish when the CFL number is increased to close to 1.	63

7.22 Profiles of pressure across the expansion wave for Cases 1 & 3 at time instants (Left) 6 ms and (Right) 8 ms. The smooth pressure profile across the expansion wave of Case 3 shows that the spatial and temporal resolution and has a large effect on the formation of multiple waves in the computational model.	63
A.1 Image of the manual valves MV4 (left) and MV5 (right)	72
A.2 Image of the vacuum pump P-1 and the manual valve MV6 (in open position)	72
A.3 Image of the manual valves and pressure sensors MV4, PI5 (left) and MV5, PI6 (right)	72
A.4 Image showing the siloxane container (top left), the swagelok FFT-1 botte (right) and valve MV1 (bottom left)	73
A.5 Image of the vapour generator HFT-1 (right) with the liquid level indicator LIT1 (top left) and valve MV2 (bottom left)	74
A.6 Image of FAST facility showing the Reference Tube (top) and the LPP and the CT (bottom)	75
A.7 Trigger Switch for FOV (left) and manual ball valve (right) connecting the LPP and the CT	76

LIST OF TABLES

3.1	Initial Conditions for the FAST experiment with D6 working fluid using the PRSV thermodynamic model. The thermodynamic variables are normalized by the corresponding critical point values	15
4.1	Real gas compressibility functions	24
4.2	Expressions for isentropic exponents	25
4.3	Initial and post-shock thermodynamic states for FAST experiment D6. The shock Mach number is defined as $M_w = u_w/c_1$. All velocities are calculated in the laboratory frame of reference. The thermodynamic properties are normalized using the corresponding critical point values	27
5.1	Geometric Parameters of the FOV and Initial Conditions of the driver and driven gas. The geometric parameters are normalized by the corresponding diameters and the thermodynamic properties are normalized using the critical point values.	33
6.1	Characteristic dimensions of FAST geometry. All the non-dimensional parameters are expressed in terms of the throat diameter.	46
7.1	Different shock tube simulations that are performed for investigating the effect of multiple wave formation	62

NOMENCLATURE

List of Abbreviations

<i>BZT</i>	Bethe-Zeldovich-Thompson
<i>CT</i>	Charge Tube
<i>CV</i>	Control Volume
<i>DNS</i>	Direct Numerical Simulation
<i>EoS</i>	Equation of State
<i>FAST</i>	Flexible Asymmetric Shock Tube
<i>FOV</i>	Fast Opening Valve
<i>GHG</i>	Greenhouse Gas
<i>LES</i>	Large Eddy Simulation
<i>LPP</i>	Low Pressure Plenum
<i>NICFD</i>	Non-ideal Compressible Fluid Dynamics
<i>ORC</i>	Organic Rankine Cycle
<i>RANS</i>	Reynold's Averaged Navier Stokes
<i>RST</i>	Reynold Stress Term
<i>RSW</i>	Rarefaction Shock Wave
<i>RT</i>	Reference Tube
<i>SST</i>	Shear Stress Transport
<i>WHR</i>	Waste Heat Recovery

List of Symbols

β_p	Isobaric compressibility	–
β_T	Isothermal compressibility	–

\dot{m}	Mass flow rate	kg/s
ϵ	Turbulence eddy dissipation	$J/kg.s$
Γ	Fundamental derivative of gasdynamics	–
γ	Ratio of specific heats	–
\hat{u}	Specific internal energy	J/kg
ν	Specific volume	m^3/kg
ν_T	Eddy viscosity	m^2/s
ω	Turbulence dissipation rate	$J/kg.s$
ρ	Density	kg/m^3
C	Discharge coefficient	–
c	Speed of sound	m/s
c_p	Heat capacity at constant pressure	$J/kg.K$
c_v	Heat capacity at constant volume	$J/kg.K$
h	Specific enthalpy	J/kg
J	Joule-Thomson coefficient	–
J	Mass flux	$kg/m^2.s$
k	Turbulence kinetic energy	J/kg
k_b	Bellow spring constant	N/m
M	Mach number	–
n_s, m_s	Isentropic coefficients	–
P	Pressure	Pa
R	Gas constant	$J/kg.K$
s	Specific entropy	$J/kg.K$
T	Temperature	T
u	Flow velocity	m/s
V	Volume	m^3

w	Wave propagation speed	m/s
Y	Expansion factor	–
Z	Compressibility factor	–

Subscripts

1	Pre-shock thermodynamic state
2	Post-shock thermodynamic state
ab	Auxiliary Bellow
br	Breach
i, j, k	Direction
lim	Limiting
o	Reference/Total
p	Piston
pb	Primary Bellow
w	Wave

1

INTRODUCTION

This chapter discusses the background and relevance of the current thesis. Section 1.1 outlines the need for research in Waste Heat Recovery (WHR) systems followed by a description of the current state-of-the-art technology in Section 1.2. Section 1.3 provides the motivation and the objectives of this thesis work followed by Section 1.5 which presents the research questions for the thesis. Finally, Section 1.6 provides a roadmap of the topics discussed in this document.

1.1. BACKGROUND

The global demand for energy is expected to grow continuously over the next three decades, increasing by nearly 48% in the year 2040. Even though efforts are being made to utilize renewable sources of energy like solar or wind power, fossil-fuels continue to be the primary energy source worldwide and will account for nearly 78% in 2040 [1]. This extensive reliance on fossil fuels risks the rise in greenhouse gas emissions (GHG) that ultimately lead to harmful environmental effects such as global warming and climate change. In Europe alone, the industrial sector is responsible for nearly one-third of the total GHG emissions, and the contribution can be even higher when considered worldwide. It is estimated that nearly 20% to 50% of the total industrial energy input is lost as waste heat, either in the form of exhaust gases or in cooling water. Though it is not entirely possible to eliminate heat losses from industrial processes, much of this waste heat can be recovered and converted into useful energy using efficient recovery systems that can help in saving a considerable amount of the input energy. These WHR systems offer a novel method to convert this otherwise lost heat into useful mechanical work or electrical energy.

The development of WHR systems such as the Organic Rankine Cycle (ORC) and the supercritical CO_2 (s- CO_2) power systems are necessary to achieve the CO_2 emission reduction targets set for the coming years. One major limitation of these technologies is the relatively low efficiencies of their turbomachinery components, which has a negative impact on their large-scale economic viability. A primary reason for the poor efficiency is the lack of understanding of the flow physics and the property modelling of dense fluids in these systems. Current efficiency levels of ORC turbomachinery lie between 70% and 75% on average. It is estimated that a 2% increase in the characterization of the properties of the working fluids, leading to a better

understanding of the flow behaviour, can yield a 5.5% increase in turbomachinery efficiency resulting in a net increase of 10% in the electrical power output [2]. The objective of this research work is to characterize the non-ideal gasdynamic behaviour of the dense vapours of such working fluids which can eventually aid in improving the performance of ORC turbomachinery and its margin for stable operation.

1.2. NEED FOR RESEARCH

ORC systems use an organic working fluid instead of steam to convert heat into electricity. The lower specific heats of organic fluids compared to steam makes them suitable for low-heat generation applications such as renewable energy sources. However, the design of turbomachinery components for such systems is challenging due to a lack of proper understanding of the non-ideal behaviour exhibited by their organic working fluids. Since there is only little experimental information available for such flows, most of the turbomachinery design for the ORC systems is done using trial and error method which affects their performance and leads to stability issues.

Internal fluid flows in the nonclassical regime are governed by the property called as the fundamental derivative of gasdynamics (Γ). Γ dictates the relation between sound speed and density and assumes a constant value that is greater than one for ideal gases. For certain fluids though, the value of Γ varies close to the critical point and can be less than one or even negative. In the region of variable Γ , the fluid exhibits unconventional phenomena such as a different variation of sound speed with density compared to ideal gases. In the classical sense, compression waves coalesce to form shock waves of the compression type whose properties can be estimated using the Rankine-Hugoniot jump relations and the ideal gas Equation of State (EoS). In most practical applications, only compressive shocks are observed since shocks of the expansive type would violate the second law of thermodynamics that states that entropy can only increase in a process. Thompson [3] first theorised that when Γ is negative, the admissibility conditions are reversed and it is only the shocks of the expansive type that are thermodynamically admissible. The study of the flow behaviour in the thermodynamic region featuring $\Gamma < 1$ is called Non-Ideal Compressible Fluid Dynamics (NICFD). The converse fluid dynamic behaviour can lead to poor performance and stability issues in turbomachinery components.

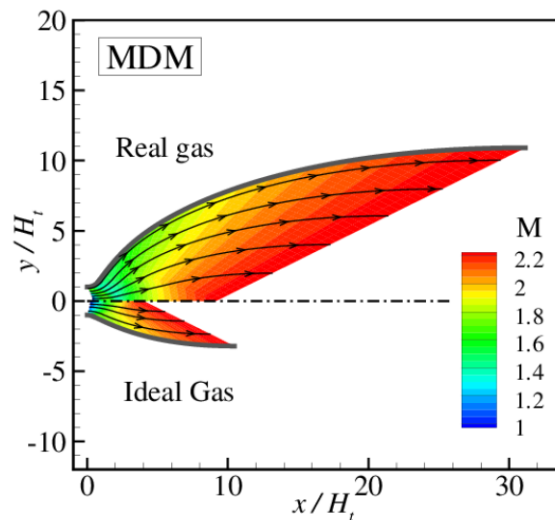


Figure 1.1: Contours of Mach number showing supersonic expansion of siloxane fluid MDM in a converging-diverging nozzle close to the saturation curve. The impact of the fundamental derivative on supersonic turbomachinery designs is clearly evident in the difference between the nozzle geometries obtained when using an ideal (bottom) and a real (top) gas [4]

1.3. MOTIVATION AND THESIS OBJECTIVE

In spite of well established theoretical knowledge in the scientific community, there has been little experimental evidence to prove the existence of nonclassical gasdynamic behavior. The first attempt to prove the existence of rarefaction shockwaves (RSW) in single-phase dense-gases was carried out by Borisov et al. [5] and Kutateladze et al. [6] in the former USSR, who claimed to have observed a RSW using Freon-13 (trifluorochloromethane, $CClF_3$) as the test fluid. However, the findings from this experiment has been refuted by Fergason [7] for not providing experimental evidence for the formation of such an expansion shock. It was shown that the model EoS for Freon-13 does not exhibit a region of negative Γ in the dense-gas region. A second experiment using a shock tube was conducted in the early 2000s by Fergason et. al. at the University of Colorado at Boulder using Perfluorofluorene (PP10, $C_{13}F_{22}$) as the working fluid. However, the experimental results were inconclusive due to the thermal degradation of PP10 at the high operating temperatures and possibly due to the presence of air and moisture within the working fluid, which are known catalysts for thermochemical decomposition [8].

The motivation for this research project arises from the need for experimental proof for the existence of nonclassical gasdynamic effects in dense-gas vapours of high molecular weight fluids. Moreover, knowledge about flow behaviour in the NICFD region can be utilized in technical applications that operate in the dense-gas regime. As mentioned in Section 1.1, one such example is the Organic Rankine Cycle where this knowledge can help mitigate the negative effects of shock formation.

1.4. GOALS OF THE THESIS

As mentioned in Section 1.3, no conclusive experimental evidence for the presence of rarefaction shock waves has been provided till date. The scope of the thesis relates to it from a scientific perspective and forms the basis of the complete research work:

To verify the existence of nonclassical gasdynamic effects by demonstrating the presence of a rarefaction shock wave in the dense-gas flows of organic fluids

This demonstration would be experimentally done in the future in the Flexible Asymmetric Shock Tube (FAST) facility that has been commissioned at TU Delft. For this thesis project, a numerical proof for the existence of nonclassical effects would be provided using computational simulations of the FAST experiment. Unlike conventional shock tubes that are fit with a diaphragm, the FAST uses a diaphragmless driver to separate the high and low pressure sections in the tube. A new conceptual design for a Fast Opening Valve (FOV) for the experimental facility has been developed to replace the existing valve which suffers from poor functionality and bad reproducibility of the experimental results. However, neither a mechanical nor a fluid dynamic characterisation of the conceptual design of the Fast Opening Valve (FOV) has been done till date making it difficult to quantify the effectiveness of the valve. The objective of the thesis is therefore framed as:

To characterize the motion of the conceptual design of the Fast Opening Valve in the experimental setup to ensure the formation of a rarefaction shock wave in D_6

1.5. RESEARCH QUESTIONS

The most important questions that guide this research work can be deduced as:

- Can the formation of a rarefaction shock wave in the FAST experiment be numerically verified?
- Is the opening time of the new FOV design sufficient to enable the formation of a RSW in the setup?
- If formed, what effect does the FOV have on the formation of a RSW, compared to that of a conventional diaphragm opening?

In order to answer these questions, a two pronged approach has been devised: firstly, an analytical model that predicts the thermodynamic properties across an expansion shock in the dense vapour flows of the test fluid is developed. Secondly, a one-dimensional model for the motion of the FOV is formulated and is implemented in the two-dimensional computational simulations to study the effect of the FOV opening time on shock formation. The results of the CFD analysis along with those of the analytical and 1D model will provide a conclusive answer to the research questions mentioned above.

1.6. CONTRIBUTIONS OF THE THESIS

The primary contributions of this research work are:

- The characterisation of the motion of the Fast Opening Valve using its mechanical properties. This is done by developing a one-dimensional compressible flow model of the valve to study its behaviour under the given conditions. This model allows for the assessment of the motion of the valve and its effect on the nearby flow field. Based on this model, the conceptual FOV design is shown to have a opening time that is nearly 3.5 times larger than the intended design opening time of 5 ms.
- The successful demonstration of the formation of a nonclassical rarefaction shock wave in the dense vapour flows of D_6 in the FAST setup using 2D RANS CFD simulations. This enables the study of the effect of the FOV opening action on the formation of the shock wave and its propagation. The results of this model suggest the formation of RSWs in the test rig for the computed FOV opening time of 18.13 ms but indicate that multiple expansion shocks and waves can be encountered in the setup.

1.7. THESIS OUTLINE

This thesis report is structured as follows. Chapter 2 provides the theoretical background for this thesis work and discusses the literature relevant to the NICFD. This brings the reader up-to-date with the current research in the field of non-ideal flow dynamics. Chapter 3 provides a description of the FAST facility and the experimental procedure and outlines the literature relevant to the design and functioning of the FOV. Following this, Chapters 4 and 5 describe the implementation of the analytical and 1D models to characterize supersonic real gas flow and FOV motion respectively. Chapter 6 provides a detailed description of the application of computational fluid dynamics to study the motion of the FOV and its effect on shock formation. Chapter 7 discusses the results of the 1D and 2D models in detail. Chapter 8 discusses definitive conclusions are drawn based on these result and provides a set of recommendations to further this research work. The roadmap of the thesis is shown graphically in Figure 1.2

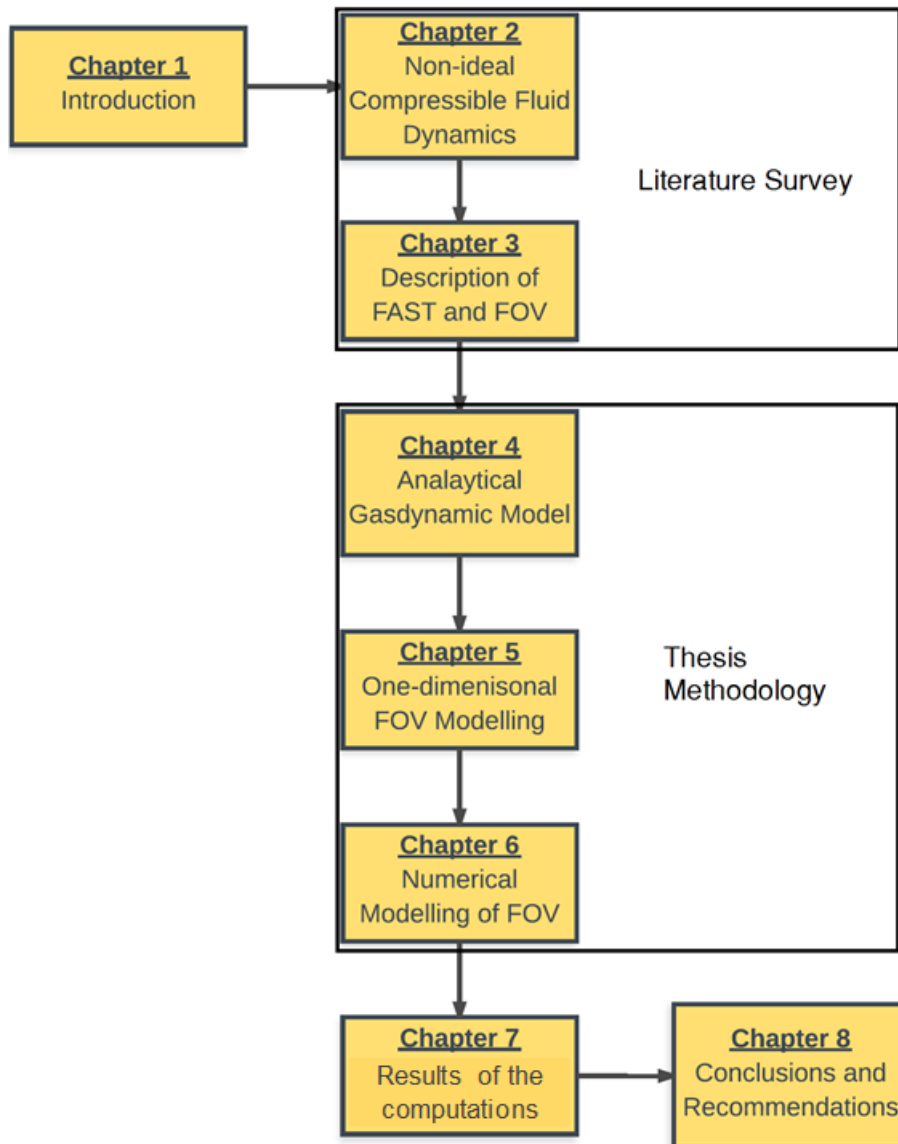


Figure 1.2: Road map of the current thesis

2

NON-IDEAL COMPRESSIBLE FLUID DYNAMICS

2.1. FUNDAMENTAL DERIVATIVE OF GASDYNAMICS

It is often assumed during studies on compressible flow dynamics that the behaviour of the fluid can be described using the ideal gas equation of state (EoS). Though this model works well at moderate temperatures and pressures, the ideal gas assumption fails to physically characterize the gas behaviour for thermodynamic states close to the critical point or the saturation condition. Various studies have shown that certain substances can exhibit gasdynamic phenomena that are considerably different from their ideal-gas counterparts at states close to the saturation curve, the most notable example being the admissibility of expansion shock-waves and compression fans [9]. Hence, thermodynamic models that take into account real gas effects need to be used for studying compressible flows of super-heated vapours in the dense-gas thermodynamic region.

The admissibility of a shock wave, whether of the compression or the rarefaction type, is governed by the second law of thermodynamics which states that the entropy must always increase in an adiabatic process. As a consequence of this law, only compressive shock waves are admissible for the case of ideal gases while rarefaction shocks are physically impossible due to the decrease of entropy [11]. Duhem [12] was the first to show that while the first and second derivatives of the entropy with respect to the density is zero when evaluated at state 1 upstream of a weak shock, the third derivative can be expressed as:

$$\left(\frac{\partial^3 s}{\partial \rho^3}\right)_1 = \frac{1}{2\rho_1^3 T_1} H \quad H = \left(2\frac{dp}{d\rho} + \rho\frac{d^2 p}{d\rho^2}\right)_1 \quad (2.1)$$

From these equations, he stated that depending on the sign of H , the fluid density either increases or decreases in the region behind the shock wave. Specifically, if H is positive, then the shock wave is of the compressive type while a negative H denotes a propagating expansion shock. The increase in entropy across weak shocks were studied independently by Becker [13] and Bethe [14]. From their work, H was found to be a measure of the curvature of the isentropes in the $P - v$ diagram (Figure 2.1) and is expressed in the non-dimensional form as [15]:

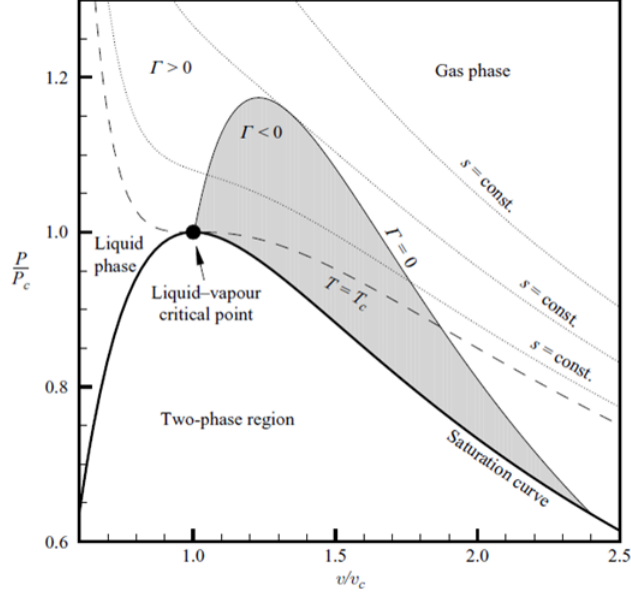


Figure 2.1: Liquid Vapour Saturation curve and negative Γ region for a BZT fluid [10]

$$\Gamma = \frac{v^3}{2c^2} \left(\frac{\partial^2 P}{\partial v^2} \right)_s = \frac{H}{2c^2} \quad (2.2)$$

where ρ is the density, P is the pressure, s is the entropy, v is the specific volume, c is the thermodynamic speed of sound and Γ is called the fundamental derivative of gasdynamics [3]. Thus, it can be seen from the above relation that if the isentropes are convex ($\partial^2 P / \partial v^2 > 0$) on a P - v diagram, then the shock will propagate as a compression and if concave ($\partial^2 P / \partial v^2 < 0$), the formation of an expansion shock is possible [11]. Γ also defines the dependency of the sound speed on density and using thermodynamic relations, Equation 2.2 can be rewritten as:

$$\Gamma = 1 + \frac{\rho}{c} \left(\frac{\partial c}{\partial \rho} \right)_s \quad (2.3)$$

Since both the speed of sound and density are positively defined, the variation of sound speed with density depends on the sign of Γ . For ideal gases, Γ is constant, greater than 1 and is equal to $(\gamma + 1)/2$ [3]. Thus, $\left(\frac{\partial c}{\partial \rho} \right)_s > 0$ and the sound speed increases with an increase in density. For $\Gamma < 1$, $\left(\frac{\partial c}{\partial \rho} \right)_s < 0$ and the sound speed increases with a decrease in density. A special case is when $\Gamma = 1$ and the sound speed is unaffected by the change in density. The following expression for the isentropic variation of the wave speed with pressure can be derived using the method of characteristics, the continuity and the momentum equations:

$$\frac{dw}{dp} = \frac{d(c+u)}{dp} = \frac{\Gamma}{\rho c} \quad (2.4)$$

Thus, for the ideal case where Γ is positive, the wave speed increases with an increase in pressure. On the other hand, when Γ is less than zero, the wave speed decreases with an increase in pressure. For these two cases, both the sound and wave speed vary similarly. When $0 < \Gamma < 1$, while the sound speed decreases, the wave speed increases with pressure albeit slower than the ideal case. Two special cases occur when $\Gamma = 1$ and

$\Gamma = 0$. In the former case, the sound speed remains constant with pressure while the wave speed increases and in the latter, the wave speed remains constant while the sound speed decreases with pressure.

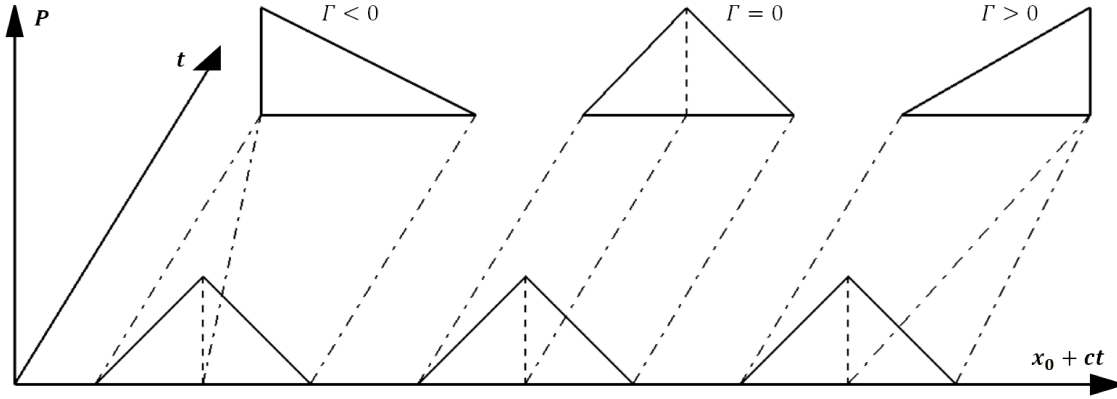


Figure 2.2: Wave propagation in the classical and nonclassical regimes. In classical dynamics, when $\Gamma > 0$, compression waves coalesce to form a compression shock wave. In NICFD with $\Gamma < 0$, a RSW is formed. A special case is when $\Gamma = 0$ where the wave propagates unaltered

This dependency of the wave speed on Γ affects the formation of shocks. Consider a one dimensional right running wave with positive pressure variation as an example. In the classical case ($\Gamma > 0$), the part of the wave that is at a higher pressure travels faster than that with a lower pressure. As a result, the wave steepens forming a compression shockwave. For $\Gamma < 0$, the wave speed increases with decrease in pressure and thus the low pressure side of the wave steepens and a RSW is formed. For the special case when Γ is zero, the wave speed is unaltered by the pressure and no shock is formed. The curvature of the isentropes in the P - v diagram not only determines what type of shock wave is admissible but also governs how the shock is formed from the initial conditions during flow propagation [13]. Figure 2.2 provides a schematic of the wave propagation for the three cases discussed here.

2.2. ADMISSIBILITY REGION FOR RAREFACTION SHOCK WAVES

In the classical theory of gasdynamics, the thermodynamic states of a gas before and after a shock wave are related by the Rankine-Hugoniot relations, which are expressed as:

$$\rho_1 u_1 = \rho_2 u_2 \quad (2.5)$$

$$p_1 + \rho_1 u_1^2 = p_2 + \rho_2 u_2^2 \quad (2.6)$$

$$h_2(v_2, p_2) - h_1(v_1, p_1) = \frac{1}{2}(p_2 - p_1)(v_1 + v_2) \quad (2.7)$$

where the subscripts 1 and 2 denote the pre-shock and post-shock states respectively. The last equation, called the shock adiabat, is obtained by solving Equations 2.5 and 2.6 for the flow velocities u_1 and u_2 and replacing them in the energy conservation equation. It describes the locus of all the possible post-shock thermodynamic states for a given set of initial conditions. By eliminating the velocity terms, the equation becomes a purely thermodynamic relation and is independent of the reference frame which can then be applied to any general shock discontinuity such as moving or oblique shocks. The mass flux, J , can be obtained by combining Equations 2.5 and 2.6:

$$J = (\rho_1 u_1)^2 = (\rho_2 u_2)^2 = -\frac{p_2 - p_1}{v_2 - v_1} \quad (2.8)$$

This represents a straight line connecting the upstream and downstream states on a P-v diagram called the Rayleigh line. Kluwick [11] shows that by combining the Gibb's equation with the jump conditions, it can be observed that:

$$\int_{v_1}^{v_2} T ds = \int_{v_1}^{v_2} de + p dv = A_H - A_R \quad (2.9)$$

where A_H and A_R are the areas below the shock adiabat and the Rayleigh line respectively in the P-v diagram. Therefore, in order for a shock to be admissible, the Rayleigh line must lie completely above or below the shock adiabat. Also, since the sign of the integral is maintained in the case of an expansion shock, a necessary condition for the formation of a RSW is that the shock adiabat must be concave down for a range of pressures and specific volumes between the initial and final thermodynamic states. The admissibility of compression and expansion shock waves based on the shock adiabat and the Rayleigh line is shown schematically in Figure 2.3. An expansion shock is admissible between states 1 and 2 since the Rayleigh line lies completely below the shock adiabat in this case. A limiting case for the formation of a RSW is represented by the process between states 1 and 5 where the Rayleigh line is tangential to the adiabat in state 5. This represents a condition where both the pre-shock and the post-shock states are sonic. A shock wave cannot connect state 1 with any state lower than 5 since then the Rayleigh line and the adiabat would cross each other violating the entropy condition. A relation between the entropy change Δs and the specific volume Δv for weak shock waves derived using Taylor expansion is as follows [16]:

$$\Delta s = -\frac{\Gamma_1}{6} \frac{c_1^2}{T_1} \left(\frac{\Delta v}{v_1} \right)^3 + O([\Delta v]^4) \quad (2.10)$$

where the subscript 1 denotes the pre-shock state and T represents the temperature. Since Δs must always be positive, it can be deduced from Equation 2.10 that only compression shock waves ($\Delta \rho > 0$ and so $\Delta v < 0$) are physically admissible when $\Gamma > 0$ while expansion shock waves are possible only if $\Gamma < 0$ [3, 10]. This equation reiterates the fact that the admissibility of a shock wave is governed by the curvature of the shock adiabat in the P-v diagram. It has been theoretically proven [14, 17] that there exist fluids of high molecular complexity, called the Bethe, Zel'dovich and Thompson (BZT) fluids, for which the isentropes show a downward curvature in a limited region in the vapour phase close to the liquid-vapour saturation curve, as shown in Figure 2.1 [10]. Flows of such fluids evolving in the negative Γ region can therefore provide an insight into the behaviour of fluids in the non-ideal gasdynamic region.

While all flows evolving within the negative Γ region show opposite features with respect to their ideal counterparts, Ferguson et. al [7] pointed out that non-classical effects can also occur between two states in the $\Gamma > 0$ region if the shock adiabat passes through the $\Gamma = 0$ boundary. Due to the limited extent of the negative Γ region, it is possible that the $\Gamma = 0$ boundary is crossed during flow evolution, thereby leading to the formation of mixed waves such as a rarefaction shock-fan combination [10].

Solving the shock adiabat for the given initial conditions provides multiple solutions for the thermodynamic state behind the shock. Amongst the possible solutions, the unique downstream state is found by imposing two other conditions - the first being the entropy condition $\Delta s > 0$ discussed earlier and the second called the

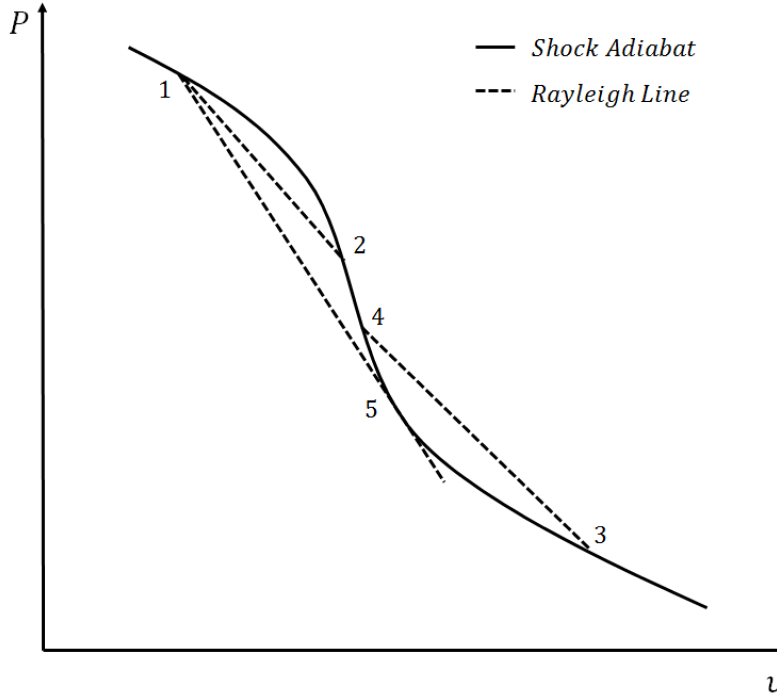


Figure 2.3: P - v plot showing the shock adiabat and Rayleigh lines for two cases: Only a shock wave of the expansive type is allowed between states 1 and 2 since the Rayleigh line lies completely below the adiabat. However, from state 3 to 4, a compression shock can exist in the flow while expansion waves flatten out. The expansion from 1 to 5 shows the limiting case when the Rayleigh line is tangential to the adiabat. For this condition, the shock is said to be sonic, i.e., both initial and final states have $M = 1$.

mechanical stability criterion[11]:

$$M_1 \geq 1 \geq M_2 \quad (2.11)$$

where M denotes the Mach number and 1 and 2 denote pre-shock and post-shock states. From Equation 2.10, it can be seen that the change in entropy is zero in the vicinity of the upstream state $v = v_1$ and the shock adiabat approaches the isentrope where $(dp/d\rho)_{RH} = (dp/d\rho)_s$ [14]. Consequently, on the adiabat:

$$\left(\frac{dp}{dv}\right)_1 = -\rho_1^2 \left(\frac{dp}{d\rho}\right)_1 = -\rho_1^2 c_1^2 \quad (2.12)$$

The continuity (2.5) and the momentum (2.6) equations can be rearranged to obtain the following relationship:

$$\frac{p_2 - p_1}{v_2 - v_1} = -\rho_1^2 u_1^2 \quad (2.13)$$

Dividing the above two equations and using the admissibility condition for the upstream state 1 gives:

$$\left(\frac{p_1 - p_2}{v_1 - v_2}\right) / \left(\frac{dp}{dv}\right)_1 = \left(\frac{u_1}{a_1}\right)^2 = M_1^2 \geq 1 \quad (2.14)$$

A similar expression can be derived for the post-shock state 2 [18]. The final equivalent expression for the mechanical stability criterion is as follows:

$$\left(\frac{dp}{dv}\right)_1 \geq \frac{p_2 - p_1}{v_2 - v_1} \geq \left(\frac{dp}{dv}\right)_2 \quad (2.15)$$

The above equation can be interpreted directly from the curvature of the shock adiabat in the P-v plane. From the second law of thermodynamics and Equations 2.9 and 2.15, it can be concluded that the Rayleigh line must not cross the shock adiabat at an interior point between the initial and final states for the shock wave to be admissible. These two conditions are equivalent if the shock adiabat is either only concave up or concave down between the initial and final states but become inequivalent if the adiabat changes curvature across the shock. The most restrictive condition is the stability criterion, implying that if Equation 2.11 is valid, then $\Delta s > 0$ [11].

2.3. SUMMARY

Based on the literature presented above, it can be concluded that nonclassical effects such as rarefaction shock waves and compression fans can be observed when the fundamental derivative of gasdynamics is negative. The RSW is the more attractive of the two choices since it can be clearly observed as a sharp drop in pressure during an expansion process crossing the BZT region. The initial temperature and pressure of the experiment are chosen such that it lies well within the nonclassical region so as to obtain a strong and a reliable rarefaction shock wave. The initial condition is verified in Chapter 4 by solving for the Rankine-Hugoniot relations (Equations 2.5 to 2.7), the entropy condition and the mechanical stability criterion (Equation 2.11).

3

EXPERIMENTAL TEST RIG

This chapter describes the experimental facility that will be used to conduct nonclassical gasdynamic experiments in the dense vapours of D6. The first section 3.1 provides an overview of the experiment followed by a description of the setup and the experimental procedure in section 3.2. The Fast Opening Valve (FOV) or the diaphragmless driver is introduced to the reader in Section 3.3. A few different driver designs that have been developed so far along with the current and new FOV designs used in FAST are discussed in subsections 3.3.2 to 3.3.4.

3.1. FLEXIBLE ASYMMETRIC SHOCK TUBE

The Flexible Asymmetric Shock Tube (FAST) facility is an unconventional Ludwieg type shock tube commissioned at TU Delft to study the propagation of waves in dense gas flows of organic compounds with the specific aim of providing the first-of-its-kind experimental evidence for the existence of nonclassical gasdynamics. It comprises of a pipe called the charge tube (CT) that is connected to a low-pressure plenum (LPP) via a Fast Opening Valve (FOV). The CT is composed of several tube segments. The working fluid is heated to the required temperature in a tank from where the dense vapour is supplied to the experiment. The tank is connected to the CT by means of a reference tube which is a short tube segment that is geometrically identical to the CT except for its length. Owing to this geometric similarity, applying the same temperature on the CT as on the RT results in the same temperature of the fluid within the tube [19]. A condenser that is connected to the heated tank on one side and the LPP on the other allows for the recovery of the working fluid. Figures 3.1 and 3.2 show the isometric and side-views of the FAST setup.

3.2. OUTLINE OF FAST EXPERIMENT

The FAST consists of a charge tube (CT) and a low pressure plenum (LPP) which are connected through a Fast Opening Valve (FOV). The CT contains the high pressure working fluid initially at rest. The entire facility is maintained at a specified temperature by a thermal control system. The experiment begins when the FOV is opened thereby allowing the high pressure gas in the CT to expand into the LPP causing an expansion wave

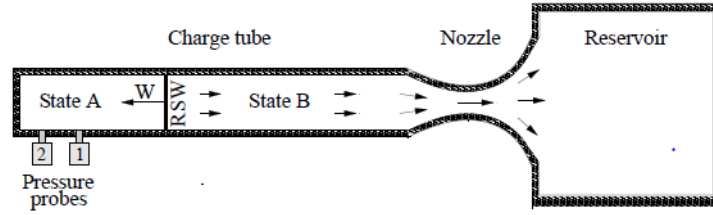


Figure 3.1: Side-view of FAST setup showing the key geometrical components. Once the FOV is opened, the high-pressure gas in the CT accelerates via the nozzle and expands into the reservoir. Consequently, an expansion wave starts to propagate into the CT that might develop into a RSW upstream. The speed of the RSW formed in the CT is measured using the pair of pressure probes located on the walls of the CT [20]



Figure 3.2: Flexible Asymmetric Shock Tube setup commissioned at TU Delft [8]

to propagate into the CT. At suitable initial conditions in the CT and the LPP, this rarefaction wave is expected to coalesce to form a rarefaction shock wave (RSW). The fluid is accelerated behind the expansion shock wave to post-shock conditions before it flows into the reservoir through the nozzle. The pressure profiles across the expansion wave are measured using four pressure transducers, PT1, PT2, PT3 and PT4 located in the CT at distances 4 m, 4.3 m, 8.3 m and 8.7 m ($153.8D$, $165.4D$, $319.2D$, $334.6D$, where D is the CT diameter) respectively from the nozzle. The wave propagation speed is then measured using the time of flight method for corresponding transducer pairs. If the wave speed is greater than the local speed of sound, then the wave moves at supersonic speed in the CT and is indeed a non-classical RSW [20].

The objective of this research work is to verify the existence of non-classical gas dynamic effects through the demonstration of a rarefaction shock wave in the CT. To observe non-classical behaviour, the test fluid must yield special properties such as high molecular complexity and must not undergo thermochemical decomposition, etc. The choice of the working fluid is of utmost importance as described in 1.3. Currently, three classes of working fluids, namely, hydrocarbons, perfluorocarbons and siloxanes are believed to exhibit a $\Gamma < 0$ region outside the scaling-law region in the vapour phase. Of these three, siloxanes prove a suitable choice for working fluids since their thermal stability at high temperatures have already been tested. The thermodynamic modelling of siloxanes is also at an advanced stage when compared to perfluorocarbons. Siloxanes are safer to handle as they polymerize upon thermal decomposition with the polymer product being non-toxic

	Symbol	Parameter	Value	Units	Dimensionless Value
Initial Conditions	P_1	Pressure	9.122	bar	0.949
	T_1	Temperature	368.96	$^{\circ}\text{C}$	0.990
	ρ_1	Density	188.13	kg/m^3	0.679
	Γ_1	Fundamental derivative	-0.1233	-	-
	u_1	Velocity	0	m/s	-
	c_1	Sound Speed	34.24	m/s	-
	M_1	Mach Number	0	-	-

Table 3.1: Initial Conditions for the FAST experiment with D_6 working fluid using the PRSV thermodynamic model. The thermodynamic variables are normalized by the corresponding critical point values [20]

whereas perfluorocarbons decompose forming hydrofluoric acid (HF) and other toxic compounds. Siloxanes are also far less flammable than hydrocarbons, making them suitable for high temperature applications [19]. Simpler molecules of the siloxane family are already being employed in ORC turbines. All these proposed reasons make siloxane the ideal choice for the current research project. In particular, cyclic siloxanes have shown to exhibit greater thermal stability than their linear counterparts and are hence preferred.

It has been shown that the size of the thermodynamic region with negative Γ values - in terms of the range of pressures and temperatures - decreases with decreasing molecular complexity [20]. Therefore, the use of siloxane fluids less complex than dodecamethylcyclohexasiloxane (D_6 , $C_{12}H_{36}O_6Si_6$) becomes infeasible. Even though more complex fluids such as tetradecamethylhexasiloxane (MD_4M , $C_{14}, H_{42}O_5Si_6$) can be used, the thermal stability of these fluids at high temperatures is not yet fully understood. D_6 was chosen as the best option for this experiment due to both its thermal stability and the size of the nonclassical region. The initial conditions for the experiment have been determined for D_6 using the Peng-Robinson cubic equation of state modified by Stryjek-Vera (PRSV) in [21] and are presented in Table 3.1. The initial state has been chosen close to the liquid-vapour saturation curve in the negative Γ region to maximize the strength of the RSW formed.

3.3. DIAPHRAGMLESS SHOCK TUBE DRIVER

A conventional Ludwieg tube makes use of a diaphragm as a barrier element to separate the high pressure CT segment from the reservoir. When the required initial conditions are reached in the driver section, the diaphragm is ruptured either by the pressure itself or by an external stimulus such as an electric shock or a ram[22]. The pressure difference across the diaphragm causes a shock wave to form and propagate into the driven section. Though this method is widely used and is effective in forming shocks, the diaphragm, upon rupturing, contaminates the test section with debris making it less attractive for the study of RSWs. Since this debris must be removed and the diaphragm needs to be replaced, it also considerably increases the time between successive experimental runs. Furthermore, the diaphragm rupture might not be consistent between runs which the reproducibility of the test results. In order to alleviate these problems, the FAST uses a diaphragmless driver.

Shock tube experiments use a wide variety of driver configurations. Two kinds of fast opening valves based on pneumatic actuators were developed by Ikui et. al [23, 24] replacing the diaphragm with either a piston that moves axially or a gate that opens transversally with respect to the shock tube axis. The researchers determined that the valve opening time was the most important criterion governing shock formation. While diaphragms typically rupture in 0.2-0.5 ms, the opening time of piston drivers depends on a range of factors

such as the weight, configuration and the actuating pressure and vary from 0.9 ms to about 0.97 ms. Transversal gates, on the other hand, take longer to open due to the higher effective opening distance when compared to the piston driver.

Muirhead and Jones [25] developed a series of fast opening valves for large shock tube applications. These designs incorporated a piston that separates the driver and driven sections and is held in position by a back-pressure. When this back-pressure is released by opening a release valve, the pressure in the driver section pushes the piston away subsequently releasing the pressure into the driven section. Oguchi et al. [26] further modified this design by replacing the cam release valve with an auxiliary piston that is also kept in place by a back-pressure. The valve is actuated by releasing the back pressure in the auxiliary piston by means of a solenoid valve. This design is widely used in the shock tube community due to the use of a pneumatic valve that can evacuate the back pressure quickly.

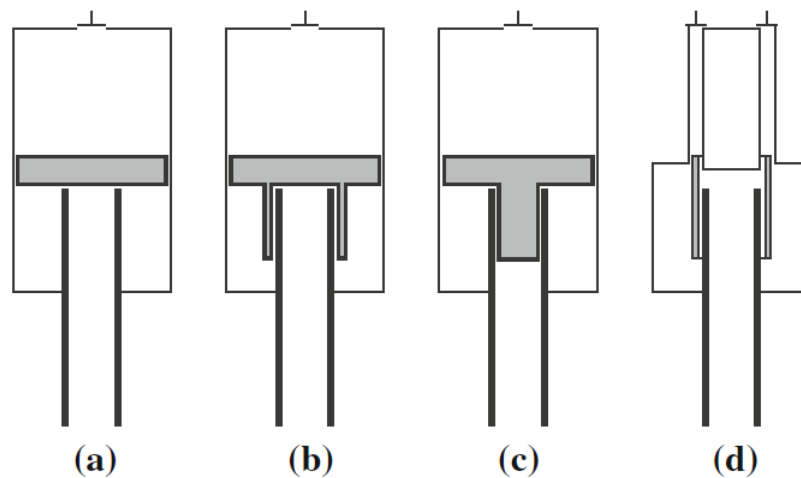


Figure 3.3: Schematic of different driver designs. a) Piston b) Piston with lip c) Piston with plug d) Sleeve [22]

A further modification to the two-piston driver was made by Takano and Akamatsu [27], who added a lip to the free piston such that it fits over a short portion of the driver section. This lip allows the piston to accelerate before breaching, thereby increasing the velocity at which the driver breaches and hence reducing the time between breaching and full opening. Downey et. al. [28] and Heufer et. al. [29] replaced the piston with a sleeve so that the driver chamber volume, and hence the pressure, is unaffected by the accelerating barrier element. However, since the area that is exposed to the pressure is smaller for sleeves, the reduction in opening time largely depends on the particular design of the sleeve mechanism. A schematic of the basic driver designs is shown in Figure 3.3.

3.3.1. FAST DIAPHRAGMLESS SHOCK TUBE DRIVER

The current FOV in the FAST is a custom made stainless steel valve placed and is the most complex component of the setup. It can be remotely operated to maintain the facility hermetically sealed for successive experimental runs.

In the open position, the test fluid can flow from the CT into the LPP through the venting holes on the inner and outer bodies in the radial direction. When the FOV is closed, the flow through the venting holes is obstructed by a sliding cylinder that is pushed between the two components. The inlet is sealed by the sliding

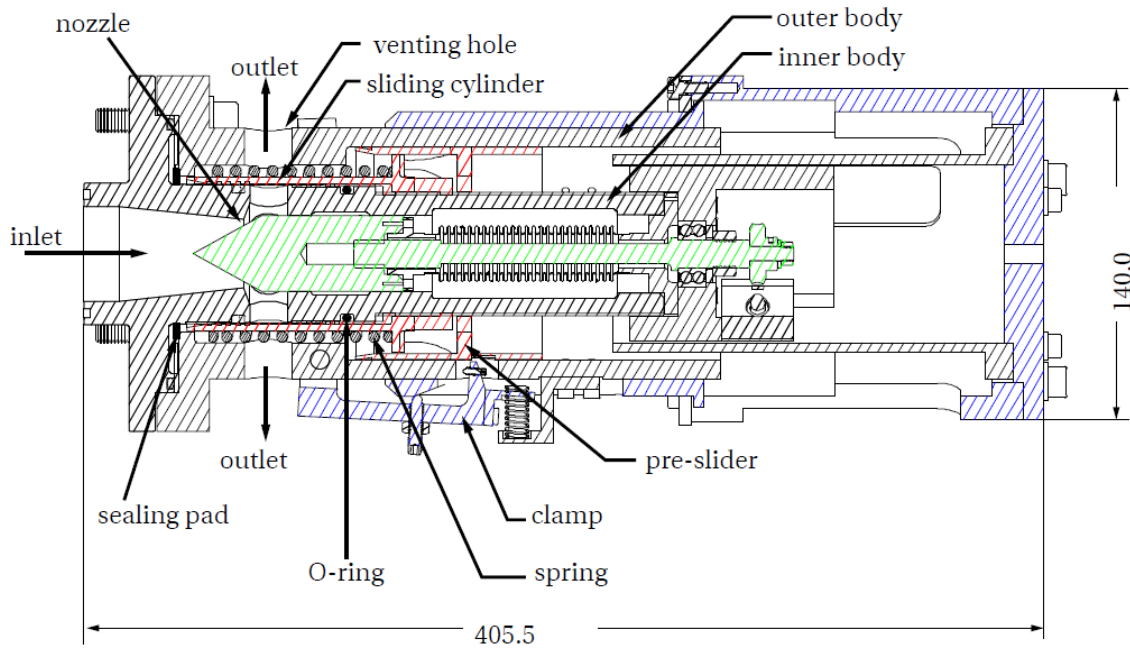


Figure 3.4: Schematic of cross-section of Fast Opening Valve [8]

cylinder as it presses into a Kalrez compound sealing pad placed on the flange. A Kalrez O-ring of 47.22 mm diameter and 3.53 mm thickness is placed between the sliding cylinder and the inner body to ensure sealing at the venting holes. Since the friction of the sliding cylinder during fast opening strongly depends on the thermal swelling of the O-ring, the temperature of the steel is monitored using a 3 mm K-type thermocouple that is inserted into a hole in the mounting flange of the FOV. An Inconel steel spring is compressed and the pre-slider is engaged by three radial clamps to prevent the release of the spring [8].

The valve is opened when the clamps are moved in the outward direction, allowing the spring to push the pre-slider and the sliding cylinder away, thereby opening the venting holes. In order to prevent flow disturbances from travelling upstream, a nozzle insert is used to create a throat to choke the flow. The throat is placed downstream of the sealing for this purpose as opposed to solutions typical to other Ludwieg tubes. The throat insert can be moved remotely in the longitudinal direction to vary the throat cross-sectional area between 420 mm² and 600 mm² which allows to modulate the strength of the expansion waves.

The moving parts in the FOV, however, have the possibility of getting jammed due to thermal expansion owing to the high operating temperatures of the facility. This can increase the opening time of the FOV which in turn affects the formation of shock waves in the CT and leads to bad reproducibility of the results. It is therefore necessary to adopt a new design for the FOV that takes into consideration the requirements of the FAST setup.

3.3.2. LOS ALAMOS NATIONAL LABORATORY DRIVER

The Los Alamos National Laboratory (LANL) driver is a diaphragmless shock tube driver designed for the LANL vertical shock tube for study of shock-driven mixing and turbulence. R. Meija Alvarez et. al. [22] studied the motion of the various driver design configurations mentioned in Section 3.3 and numerically modelled their performance. They concluded that the lowest opening times were produced by the piston with a plug or a lip (Figure 3.3(b),(c)) since in these designs, the barrier element accelerates to a high speed before breaching. Of the two, the plug has aerodynamic advantages since it can be given a streamlined shape that will

reduce the pressure loss as the driver gas expands into the driven tube. The researchers incorporated these findings in their new driver design which features a two-body barrier element, namely the piston-plug and a sliding sleeve. The LANL driver has a functionality that is opposite to the FAST FOV. This is due to the fact that the high pressure section of the LANL shock tube is in an external pressure vessel while the shock tube houses the high pressure gas in FAST. A schematic of the driver and its opening action is shown in Figure 3.5.

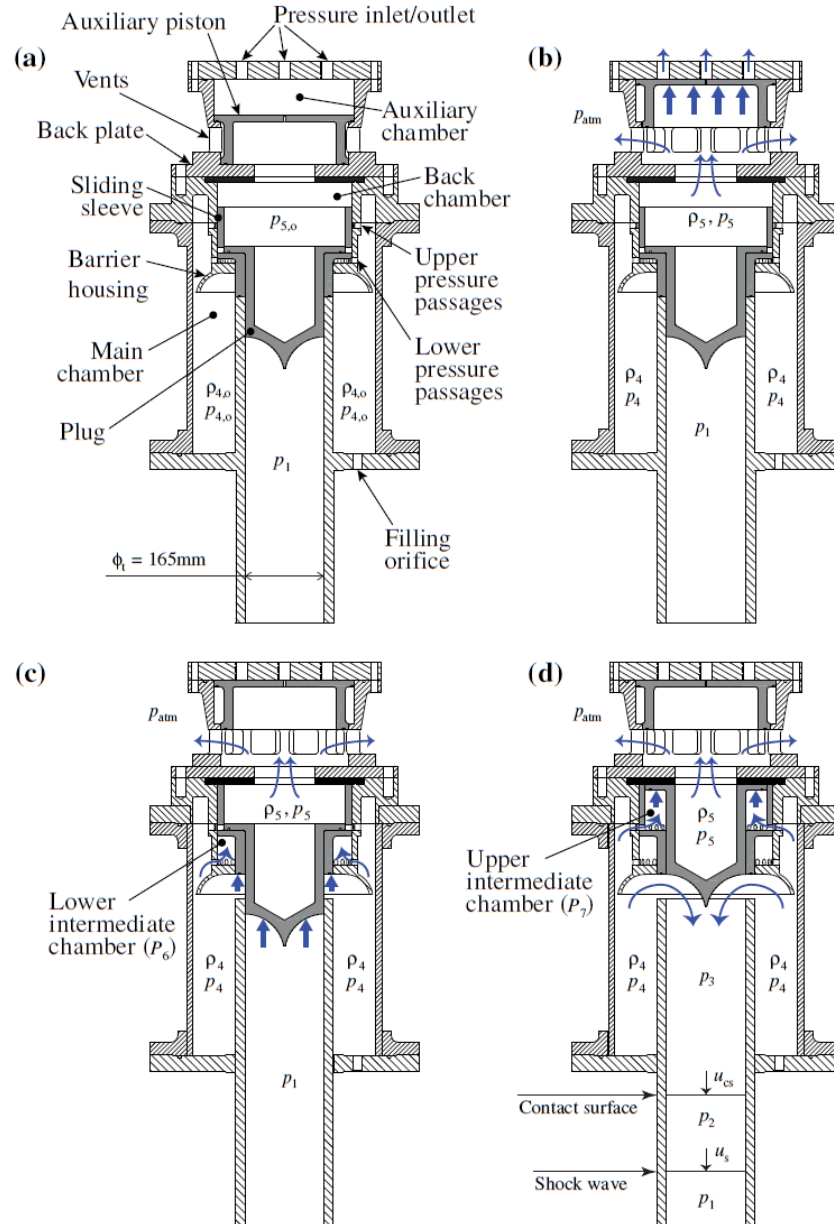


Figure 3.5: Schematic of LANL driver showing its three-staged opening motion (a) The main chamber pressure is increased to $p_{4,0}$ (b) The auxiliary chamber is evacuated through the pressure inlet/outlet. The auxiliary bellows move upwards as a result clearing the vents (c) The back-pressure p_5 releases through the vents creating a pressure imbalance across the barrier element. The main chamber and the lower intermediate chamber pressure (p_4 & p_6) thereby pushes the plug-sliding sleeve system away from the driven section till the sliding sleeve is stopped at the top of the back chamber (d) The upper intermediate chamber pressure (p_7) continues to push the piston upwards till it breaches and the main chamber pressure exhausts into the driven section. [22]

The two-body barrier system is initialized to the driver pressure in several steps. The auxiliary chamber at the top of the driver is initially pressurized through the pressure inlet (Figure 3.5(a)). This pushes the auxiliary piston against the backplate thereby sealing the latter from the exterior. The back chamber is slowly pressur-

ized through a small orifice in the auxiliary piston. When the required pressure ($p_{5,0}$) is attained in the back chamber, the sliding sleeve and the piston move towards the shock tube inlet with the sliding sleeve sealing the main chamber from the exterior and the plug inserting into the inlet of the shock tube, see Figure 3.5(a). Once the shock tube is sealed, the main chamber is pressurized up to the required pressure ($p_{4,0}$). Since the area of the plug-sleeve couple exposed to $p_{5,0}$ is larger than that exposed to $p_{4,0}$, there is a net force that pushes the barrier element against the rim of the shock tube even when $p_{4,0} = p_{5,0}$. The driver is ready to be fired at this condition.

The driver is fired in a three-staged process: first, the pressure in the auxiliary chamber is released using a solenoid valve through the pressure outlet, as shown in Figure 3.5(b). The auxiliary piston retracts due to the dropping pressure, clearing the vents in the back chamber. The back chamber pressure exhausts quickly creating a force imbalance on the top and bottom surfaces of the plug-sliding sleeve system. As the sleeve moves upwards from the rim, the area that was in contact with the rim is now exposed to $p_{4,0}$ thereby increasing the upward force. Since the piston is not directly exposed to $p_{4,0}$, the plug-sliding sleeve couple initially move together. However, at the end of this stage, the motion of the sliding-sleeve is stopped by the padding on the backplates, as shown in Figure 3.5(c). Since the piston-plug is not attached to the sliding sleeve but is merely pushed by it, the plug continues to move by virtue of its upward momentum.

As the piston separates from the sliding-sleeve, the high-pressure gas flows into the upper-intermediate chamber thereby pressuring it. This pressure pushes the piston-plug away from the shock tube inlet and hence allows the plug to keep accelerating. The accelerating piston breaches at a high speed finally stopping at the padding in the backplates (Figure 3.5(d)). Since the plug detaches from the sliding-sleeve during this stage, the weight of the moving parts is reduced by nearly 50% further increasing the barrier element acceleration [22].

The authors conducted a series of experiments with the new driver and concluded that the opening time of the LANL driver was comparable to that of aluminium diaphragms. For the range of Mach numbers measured, the LANL driver performed close to that of an ideal driver. The aerodynamic design of the plug is also reported to have reduced pressure losses when fully open. The high velocity achieved during opening due to the acceleration of the barrier element even before breaching greatly reduces the opening time of this driver. Since a short opening time is expected of the FOV in FAST as well, the two-barrier element design of the LANL driver was one of the designs that were studied for modelling the new FAST FOV driver.

3.3.3. BELLOWS-ACTUATED SHOCK TUBE DRIVER

A schematic of the bellows-actuated driver design is shown in Figure 3.6. This novel diaphragmless shock tube driver was developed by R.S. Tranter et al. [30] and makes use of metallic bellows as a secondary barrier element instead of the auxiliary piston. In this design, an edge welded bellow is placed inside the driver section facing the driven section. The bellow is attached to a stainless steel shaft using a mounting collar. The shaft faces the driven section through a linear bearing to ensure that the shaft runs along the center of the driver section. An aluminium plate with a circumferential O-ring is fitted onto the shaft at the other end. Two 1/2 inch diameter feedthroughs are attached to the flange onto which the bellows are mounted. Initially, the flange containing the bellows is pressurized by a compressed gas supply through a 1/2 inch National Pipe Thread (NPT) port, thereby compressing the bellows. This causes the shaft and the aluminium plate to seal the opening between the driver and the driven sections. When the gas in the flange is evacuated through the feedthroughs, the bellows expand, pulling away the aluminium plate from the opening and hence causing

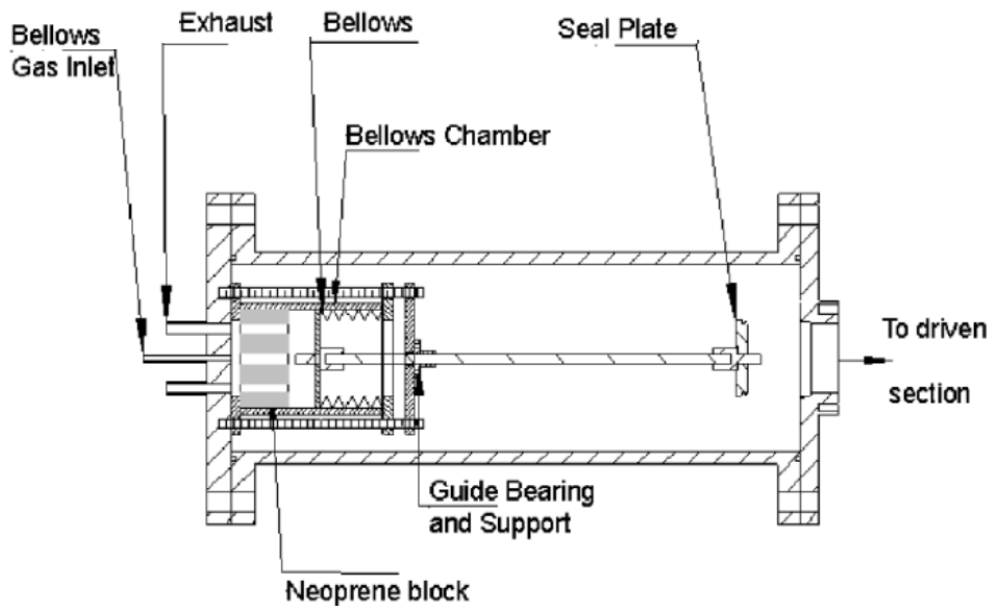


Figure 3.6: Schematic of Bellow-actuated diaphragmless shock tube driver. When the bellows is pressurized with gas, the seal plate attached to the shaft seals the opening to the driven section. The seal plate is pulled away from the opening when the bellows are vented thereby allowing the high pressure gas to expand into the driven section. [30]

the driver gas to expand into the driven section. A 2 inch thick neoprene block is placed at the end of the bellows chamber to prevent the bellows from expanding by more than 1 in. past their equilibrium position in order to reduce vibrations due to the firing action [30].

3.3.4. NEW FOV FOR FAST - CONCEPT DESIGN

As mentioned in Section 3.3.1, the current FOV in the FAST facility was found to be unsuitable for experiments in the non-classical regime due to its poor functionality and bad reproducibility of the experimental results. To mitigate this problem, a new FOV was designed at TU Delft. This design incorporates the features described in Sections 3.3.3 and 3.3.1. Specifically, it uses the staged opening action of R Meija Alvarez et. al. [22] to accelerate the barrier element before breaching so as to reduce the opening time. However, since the FAST experiment is performed at a high temperature, it is possible that the barrier elements get stuck together due to thermal expansion and are not separated at a later stage as intended in the LANL design. To prevent this from happening, the sleeve in the LANL design is replaced with the bellows from the design of R.S. Tranter et al [30]. A schematic of the new design is shown in Figure 3.7.

The primary (purple) and the secondary (red) bellows are mounted onto the existing LPP cover flange (dark blue) via an adapter plate. A cavity of 26 mm diameter in the base flange of the FOV acts as a throat connecting the CT to the LPP. The plug (brown) is inserted through this cavity into the CT similar to the design mentioned in Section 3.3.3. The piston is fitted onto the primary bellows which is housed in the primary base (dark green). The auxiliary base (blue) houses the auxiliary bellows in a similar manner. Charging of the bellows is done via a 1/2 inch flexible tube connected to a helium source via a manual ball valve. The primary bellows are charged through a 5 mm diameter hole in the lid of the auxiliary bellows. The auxiliary bellows are vented through a 1 in. tube that is connected to a vacuum tank through a solenoid valve. The vacuum tank is connected to the vacuum pump using a manual ball valve.

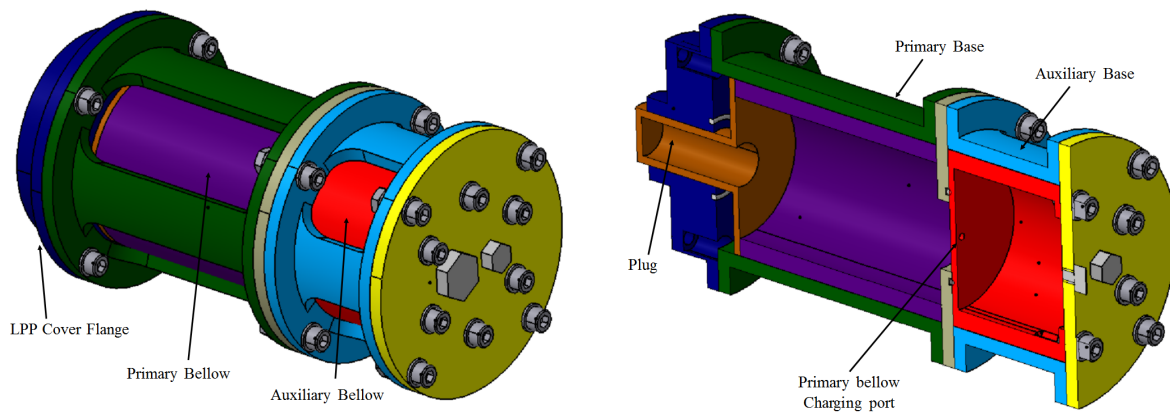


Figure 3.7: Conceptual design of a new Fast Opening Valve for the FAST experimental setup

The exhaust diameter for venting the bellows is a limiting factor influencing the performance of the driver [22]. To reduce the opening time, it is necessary to have the maximum allowable exhaust diameter for the bellows. However, the diameter of the exhaust is limited by the size of the solenoid valve in use. One of the primary reasons for incorporating an auxiliary piston is to increase the exhaust diameter of the primary bellows. Since only the auxiliary bellow is connected to the solenoid valve, the primary bellow design can include a larger exhaust which is initially sealed by the extended auxiliary bellow. When the secondary bellow is vented, it moves away from the outlet of the primary bellow allowing for a larger discharge of helium into the LPP and thereby ensures a smaller opening time.

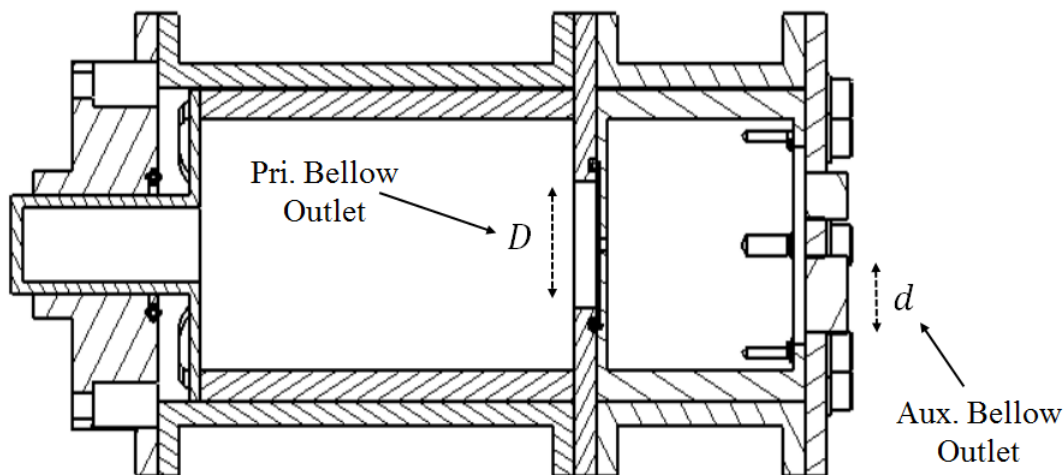


Figure 3.8: Schematic of different driver designs. a) Piston b) Piston with lip c) Piston with plug d) Sleeve [22]

Though a conceptual design of the FOV has been made, neither a mechanical nor a fluid dynamic study of the design has been performed till date. It is necessary that the performance of the FOV is assessed prior to its manufacturing and usage in the experiment. To better understand the performance characteristics of the driver, a one-dimensional model is developed in this thesis that computes the opening time and motion of the driver based on its mechanical properties. The effect of the FOV motion on the nearby fluid is also studied in this model. The formulation of the model along with the results are presented in Chapter 5.

3.4. SUMMARY

Based on the literature presented in this chapter, it can be surmised that a diaphragmless shock tube driver possesses key advantages over a conventional rupturing diaphragm which can prove essential for the non-classical FAST experiment. For this experiment, and for a driver in general, the opening time is a crucial parameter that determines the effectiveness of the driver in forming a reliable shock wave. Moreover, the driver must also be suitable to be employed in the experimental conditions of the FAST setup. It is therefore necessary to perform a detailed analysis of the conceptual design so as to ensure its applicability for the proposed experiment. Since only a conceptual design was done till date, this thesis will focus on modelling the motion of the driver and analysing its effect on the formation of a shock wave in the FAST setup.

4

ANALYTICAL MODELLING OF NORMAL SHOCKS IN NON-IDEAL FLOWS

This chapter describes the analytical solution for normal shock waves in real gas flows. The model serves as an efficient tool for estimating the thermodynamic states downstream of a normal shock wave in real gases, especially for flows evolving in the non-classical regime. The results of this model can serve as a guide for further numerical and experimental analyses. Section 4.1 presents the underlying thermodynamic concepts governing real gas flows followed by Section 4.2 which discusses the analytical model in detail. Section 4.3 provides the results of this routine.

4.1. REAL GAS THERMODYNAMICS

Real gases are gases that do not behave as predicted by the ideal gas law due to the interaction between the gas molecules. Ideal gases are in fact an assumption of the real gas behaviour. Unlike an ideal gas, properties such as the compressibility and specific heats are not constant for a real gas but instead vary depending on its thermodynamic conditions. These factors must be taken into account in order to understand the behaviour of real gases. Before presenting the analytical model for real gas flows, it is necessary to establish some important thermodynamic relations for real gases and to study their departure from ideal gas theory.

4.1.1. COMPRESSIBILITY FACTOR

The compressibility factor is the magnitude of a fluid's deviation from ideal gas behaviour and is expressed as $Z = v/v_{ideal}$, where $v_{ideal} = RT/P$ is the ideal gas specific volume. The relative change in specific volume with respect to pressure at constant temperature and with respect to temperature at constant pressure is given by isothermal and isobaric compressibility respectively. The definitions of these thermodynamic properties are given in Table 4.1.

As can be seen from the table, these parameters reduce to simple terms in the case of ideal gases but are a necessary addition in the thermodynamic relations of real gases [31].

Parameter	Definition	Ideal Case
Compressibility Factor (Z)	$f(p, T)$	1
Isobaric Compressibility (β_p)	$\frac{1}{v} \left(\frac{\partial v}{\partial T} \right)_p$	$\frac{1}{T}$
Isothermal Compressibility (β_T)	$-\frac{1}{v} \left(\frac{\partial v}{\partial p} \right)_T$	$\frac{1}{P}$

Table 4.1: Real gas compressibility functions from [31]

4.1.2. CALORIC EQUATION OF STATE

For a real gas, the enthalpy is not a function of only temperature but also of pressure. As a result, a more fundamental equation for enthalpy must be considered for the case of real gases:

$$dh = c_p dT + v(1 - \beta_p T) dp \quad (4.1)$$

For the ideal case, the second term of Equation 4.1 vanishes resulting in the expression for a ideal gas, $dh = c_p dT$. The internal energy can also be expressed in a similar manner in terms of temperature and specific volume:

$$du = c_v dT + p \left(\frac{\beta_p T}{\beta_T p} - 1 \right) dv \quad (4.2)$$

As in the previous case, the second term vanishes for a ideal gas, thereby reducing Equation 4.2 to the form, $du = c_v dT$. An analytical solution for the Rankine-Hugoniot equation is complicated due to this dependency of the enthalpy on both the temperature and pressure [31]. To mitigate this problem, a model has been developed to solve for the thermodynamic properties downstream of a shock wave in a real gas.

4.1.3. ISENTROPIC COEFFICIENT

Another important difference between the real and the ideal cases is the isentropic exponent. In the case of an ideal gas, an isentropic process is expressed in the p-v coordinates as $pv^\gamma = \text{const}$. For non-ideal gases however, the isentropic exponent is a function of the isothermal compressibility and the specific heat ratio. Substituting γ with n_s and differentiating the isentropic equation gives:

$$\frac{dp}{p} + n_s \frac{dv}{v} = 0 \Big|_{s=\text{const}} \quad (4.3)$$

Rearranging the terms, n_s can be written as:

$$n_s = -\frac{v}{p} \left(\frac{\partial p}{\partial v} \right)_s \quad (4.4)$$

The right hand side of the above equation can be simplified by using the Gibb's equation and Maxwell's cyclic rules to show that:

$$\gamma = \frac{c_p}{c_v} = \frac{(\partial p / \partial v)_s}{(\partial p / \partial v)_T} \quad (4.5)$$

This can also be expressed as:

$$-\frac{v}{p} \left(\frac{\partial p}{\partial v} \right)_s = -\gamma \frac{v}{p} \left(\frac{\partial p}{\partial v} \right)_T = \frac{\gamma}{\beta_T p} \quad (4.6)$$

Substituting Equation 4.6 into 4.4 gives an expression for the isentropic exponent:

$$n_s = \frac{\gamma}{\beta_T p} \quad (4.7)$$

A detailed derivation of Equation 4.7 can be found in [31]. A different isentropic exponent can be derived when using T-p coordinates for the isentrope. These exponents for both ideal and real gases are shown in Table 4.2.

Isentrope	Exponent	General Expression	Ideal Case
$p v^{n_s} = \text{const}$	n_s	$\frac{\gamma}{\beta_T p}$	γ
$T p^{-m_s} = \text{const}$	m_s	$\frac{\gamma-1}{\gamma} \frac{\beta_T p}{\beta_p T}$	$\frac{\gamma-1}{\gamma}$

Table 4.2: Expressions for isentropic exponents [31]

The importance of the compressibility factors and the need for using appropriate EoS for determining the derived quantities is seen in the Table 4.2. This different form of the isentropic exponent also has an effect on the speed of sound of a real gas. The speed of sound is expressed as:

$$c^2 = \left(\frac{\partial p}{\partial \rho} \right)_s = -v^2 \left(\frac{\partial p}{\partial v} \right)_s \quad (4.8)$$

Substituting Equation 4.6 in 4.8 yields:

$$c = \sqrt{n_s p v} = \sqrt{n_s Z R T} \quad (4.9)$$

As can be observed in Equation 4.9, the speed of sound for a real fluid is not a function of temperature alone as in the ideal case but is also dependent on the compressibility factor and the isentropic exponent. In certain dense gases, this can cause the speed of sound to decrease even when the temperature is increasing, thereby leading to an inversion in gasdynamic behaviour and giving rise to nonclassical effects (see Section 2.1).

4.2. ANALYTICAL MODEL FOR NORMAL SHOCKS IN REAL GAS FLOWS

The estimation of the thermodynamic properties downstream of a normal shock wave from known upstream values is a complex and a time-consuming process. There are five important state variables involved, namely, pressure p , specific volume v , temperature T , enthalpy h and velocity u . These variables can be evaluated using five basic equations: the mass, momentum and energy conservation equations, the EoS and the caloric state equation. A propagating normal shock is formed in the Charge Tube (CT) and the conservation equations, together called the Rankine-Hugoniot (RH) relations written in the reference frame of the shock are as follows:

$$\rho_1 u_1 = \rho_2 u_2 \quad (4.10)$$

$$p_1 + \rho_1 u_1^2 = p_2 + \rho_2 u_2^2 \quad (4.11)$$

$$h_1 + \frac{1}{2} u_1^2 = h_2 + \frac{1}{2} u_2^2 \quad (4.12)$$

where 1 and 2 denote the pre-shock and post-shock states respectively. The shock adiabat, introduced in Section 2.2, is given as:

$$h_2(v_2, p_2) - h_1(v_1, p_1) = \frac{1}{2}(p_2 - p_1)(v_1 + v_2) \quad (4.13)$$

For the case of ideal gases, the Equations 4.10 to 4.12 are explicit and can be solved analytically. However, for the case of a real gas, these equations can be solved only numerically due to the complexity of the EoS and the enthalpy equation (see Section 4.1.2) [32]. D_6 , the test fluid used in the FAST experiment, is one such gas and in order to overcome this difficulty, an analytical method has been devised for calculating the properties across a normal shock wave for real gases.

Since the EoS and the enthalpy cannot be directly calculated as for an ideal gas, the software FluidProp is used to estimate the thermodynamic parameters of the gas. FluidProp is a standard interface to several software libraries for the estimation of thermodynamic and the transport properties of several fluids [33]. It was developed at the Energy Technology Section at TU Delft. Each library implements one or many thermodynamic models for a different number of fluids and mixtures. For the case of D_6 , the StanMix library is used which models the fluid based on the improved Peng-Robinson cubic EoS modified by Stryjek-Vera (*iPRSV*).

The input conditions required for this model are the initial pressure, temperature and the specific gas constant of the test fluid. Since an iterative procedure is followed, an initial guess of the range of pressures and temperatures of the possible post-shock state could lie is also required. The range of the guessed post-shock temperature and pressure affects only the speed of the routine and not the accuracy of the result. Once these data are input in the model, the downstream state is estimated as follows:

- First, the possible post-shock states are evaluated by solving the left and right hand sides of Equation 4.13 for each pair of the input post-shock p and T and the pairs for which the error is least between the two sides are identified. These (p, T) pairs belong to the post-shock states that lie on the shock adiabat passing through the upstream state.
- All possible downstream conditions for the given initial state have been evaluated but the unique solution is obtained by checking for two other criteria: the entropy condition and the mechanical stability criterion (see Section 2.2). The mechanical stability criterion is the limiting condition of the two and thus, this condition is verified for each of the (p, T) pairs obtained from the previous step. There can be only one pair for which this condition is satisfied and that pair is the downstream thermodynamic state of the gas across a normal shock wave.

Once the downstream p and T are known, all other state variables can be evaluated using FluidProp. Depending on whether the initial condition lies within the non-ideal thermodynamic region or not, the final post-shock state can signify the presence of a classical compression or a nonclassical expansion shock wave in the flow. A flowchart of the analytical model is shown in Figure 4.3. The results of this routine are provided in Chapter 7.

4.3. ANALYTICAL MODEL FOR REAL GASDYNAMIC FLOWS

The results of the analytical solution for normal shock waves in D6 are provided in Table 4.3. The initial conditions for the experiment have been chosen on the liquid vapour saturation curve in the negative Γ region so as to maximize the Mach number of the RSW [20]. From the table, it can be seen that the model predicts a rarefaction shock wave that is travelling upstream into the charge tube at a speed of 35.03 m/s. The value of Γ behind the shock wave is less than 1 indicating that non-ideal effects can still be observed in this region though RSWs cannot exist. The shock Hugoniot and the Rayleigh line of the expansion process are shown in the contours of Γ in Figure 4.1 and a close-up of the process is shown in Figure 4.2.

	Symbol	Parameter	Value	Units	Dimensionless Value
Pre-Shock State 1	P_1	Pressure	9.122	bar	0.949
	T_1	Temperature	368.96	$^{\circ}\text{C}$	0.990
	ρ_1	Density	188.13	kg/m^3	0.679
	Γ_1	Fundamental derivative	-0.1233	-	-
	u_1	Velocity	0	m/s	-
	c_1	Sound Speed	34.24	m/s	-
	M_1	Mach Number	0	-	-
Rarefaction Shock Wave	u_w	Wave Speed	35.03	m/s	-
	M_w	Mach Number	1.023	-	-
Post-Shock State 2	P_2	Pressure	8.02	bar	0.834
	T_2	Temperature	363.73	$^{\circ}\text{C}$	0.976
	ρ_2	Density	127.35	kg/m^3	0.459
	Γ_2	Fundamental derivative	0.1380	-	-
	u_2	Velocity	16.87	m/s	-
	c_2	Sound Speed	51.90	m/s	-
	M_2	Mach Number	0.325	-	-

Table 4.3: Initial and post-shock thermodynamic states for FAST experiment D6. The shock Mach number is defined as $M_w = u_w/c_1$. All velocities are calculated in the laboratory frame of reference. The thermodynamic properties are normalized using the corresponding critical point values

It can be observed from Figure 4.2 that the Rayleigh line completely lies below the shock adiabat thus demonstrating the admissibility condition for the formation of a nonclassical expansion shock wave. Also, it can be seen that the Rayleigh line is tangent to the shock adiabat at the downstream state indicating a sonic post-shock state:

$$\left(\frac{dp}{dv}\right)_1 \geq \frac{p_2 - p_1}{v_2 - v_1} = \left(\frac{dp}{dv}\right)_2 \quad (4.14)$$

4.4. SUMMARY

An analytical method to estimate the thermodynamic properties across a normal shock wave for the case of a real gas was presented in Section 4.2. The model predicts the formation of a rarefaction shock wave in the flow for the given initial conditions. Though it doesn't take into account factors such as area change that are present in the FAST setup, the model provides an estimate of the thermodynamic properties of the possible

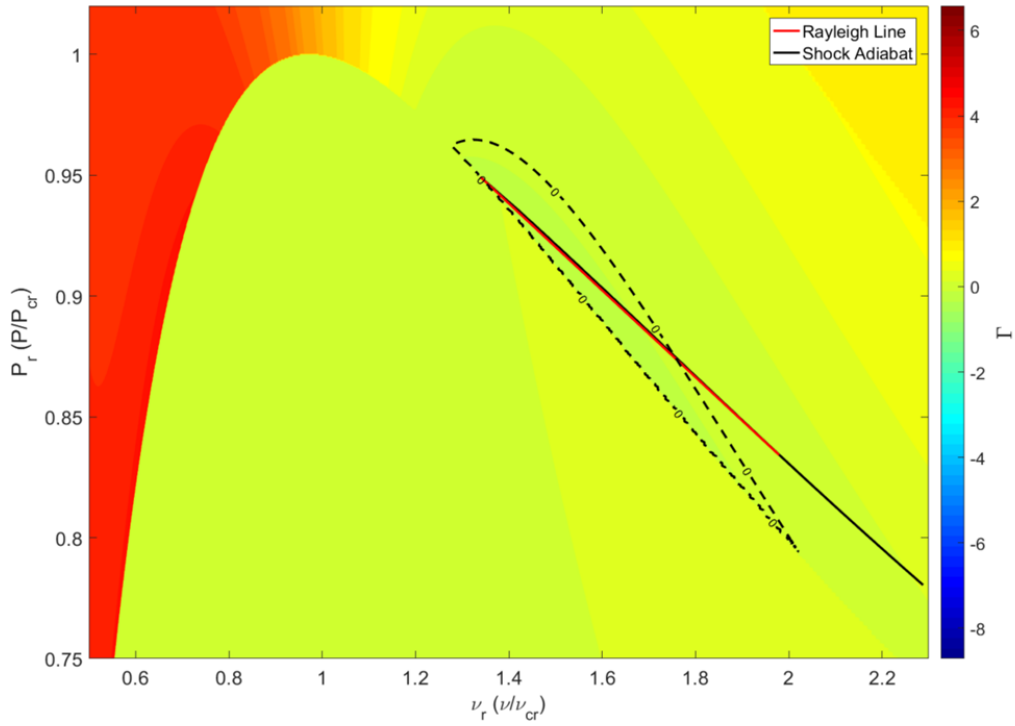


Figure 4.1: Contours of Γ shown in the P-v plot for D_6 with the expansion process denoted by the Hugoniot and the Rayleigh lines. The $\Gamma = 0$ line is shown in dotted lines.

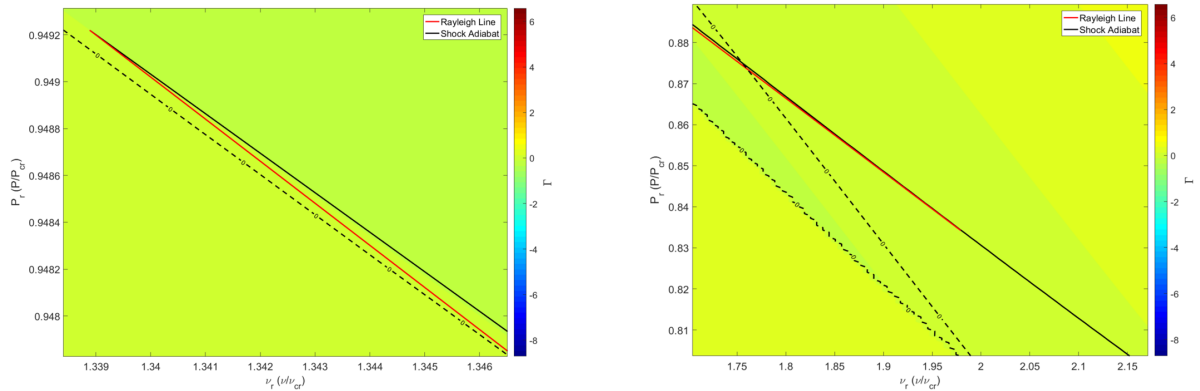


Figure 4.2: Close-up of the Hugoniot and Rayleigh lines connecting the pre-shock and post-shock states. The Rayleigh line completely lies below the shock adiabat. Also the Rayleigh line is tangent to the adiabat in the downstream state indicating a sonic post-shock state.

rarefaction shock that would be generated for the given initial conditions. The results of this model serve as a guide to verify the outcomes of the computational and experimental studies.

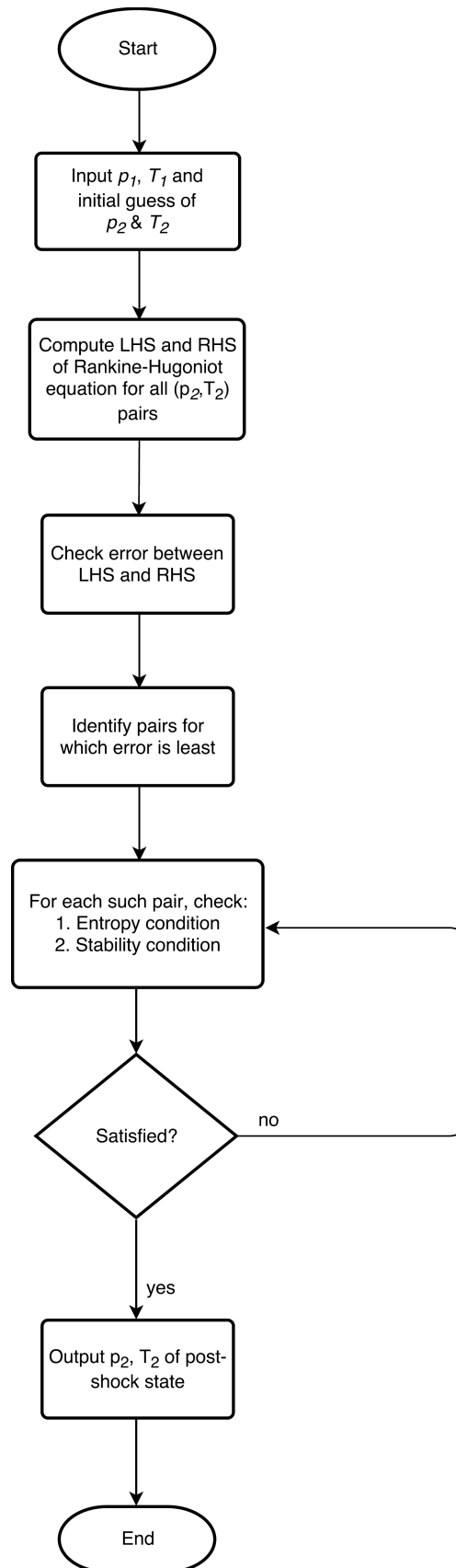


Figure 4.3: Flow-chart of the analytical gasdynamic model

5

MODELLING OF FOV MOTION

As mentioned in Chapter 3, the Fast Opening Valve is a critical component in the experimental setup whose opening time can affect the successful formation of a shock wave in the charge tube. The opening time of the FOV must be as low as possible to increase the chances of forming a shock in the CT. In this chapter, a numerical model for the motion of the new FOV design is presented which will be used to determine its opening time. Based on the results of this approach, numerical calculations of the FOV motion will be developed which and results discussed in Chapter 6.

5.1. MODELLING DRIVER PERFORMANCE

In order to estimate the opening time of the FOV, the opening speed and the pressure evolution are modelled as a function of time and the mechanical properties of the driver [22] such as the mass of the piston, spring constant of the bellow. A schematic of the proposed FOV design with the dimensions is shown in Figure 5.1. The pressure in the charge tube is denoted as p_4 and in the reservoir as p_1 . Once the driver is opened and a shock is formed, we denote p_4 and p_3 are the pressures before and after the expansion wave. The back-chamber pressures of the helium gas within the primary and auxiliary bellows are denoted by p_{52} and p_{51} respectively. The geometric parameters and the initial conditions are presented in Table 5.1.

To model the compressible flow inside the driver, a time-dependent control-volume formulation for the conservation of mass is carried out in the charge tube, the primary and the auxiliary bellows, referred to here as control volumes CV_4 , CV_{52} and CV_{51} respectively in Figure 5.1 and the mass conservation principle (Equation 5.1) is applied :

$$\rho Au = constant \quad (5.1)$$

For a given control volume, the left hand side of the conservation of mass equation represents the inflow/outflow through the boundaries of the CV and the right hand side denotes the mass variation within the CV over time. Since both the primary and auxiliary bellows are identical, the control volume formulation is shown here only

for the primary bellows.

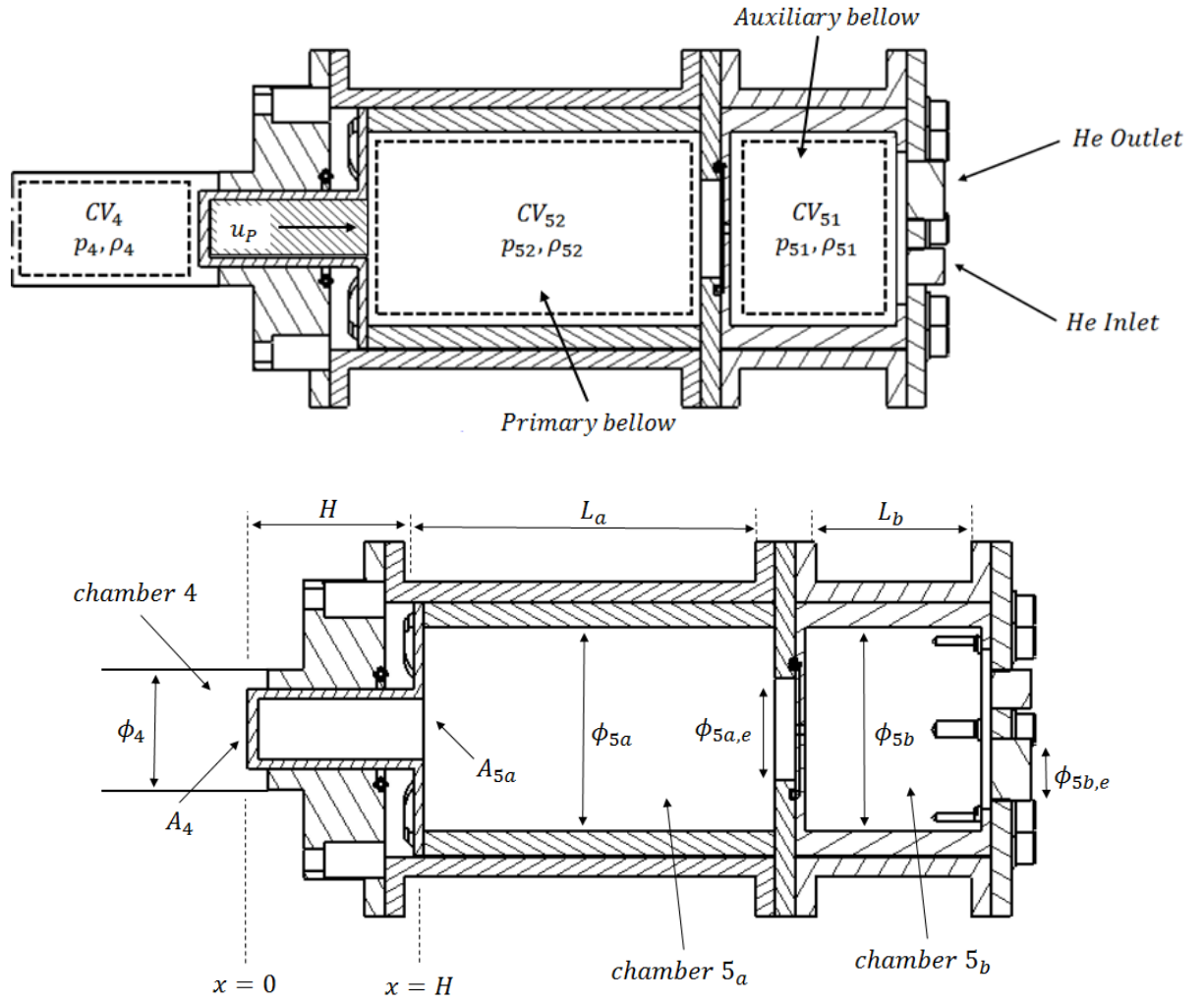


Figure 5.1: Cross-sectional view of the new Fast Opening Valve design showing key dimensions

In Equation 5.1, ρ is the instantaneous density in the CV, \mathbf{u} is the flow velocity entering/leaving the CV, S represents the area of the CV inlet and outlet, and V denotes the instantaneous volume of the CV.

For the modelling, only the effect of forces acting on the piston in the direction of motion is considered. Since only the pressure force exerted by the fluid on the FOV contributes to its motion, the shear stresses acting on the walls of the CT and the piston can be neglected. Also, it is assumed that the piston completely seals the throat and that no fluid is present between the piston and the walls. Therefore, the flow can be considered to be inviscid and one-dimensional. The system is also assumed to be adiabatic since the process of shock generation is too fast for any significant heat transfer. The bellows are assumed to function as perfect springs with a spring constant k . Though the motion of the FOV is formulated as a one-dimensional model, the pressures in the charge-tube and the bellows are considered to be lumped quantities (see Section 5.2). The density of the working fluid can be expressed in terms of its pressure using adiabatic relations as (shown in Equation 5.2):

$$\rho_4 = \rho_{40} \left(\frac{p_4}{p_{40}} \right)^{\frac{1}{\gamma_4}} \quad \rho_5 = \rho_{50} \left(\frac{p_5}{p_{50}} \right)^{\frac{1}{\gamma_5}} \quad (5.2)$$

	Symbol	Parameter	Value	Units	Dimensionless Value
Charge Tube and Piston	ϕ_4	Diameter	40	mm	1
	A_{5a}	Cross-sectional Area	1256.64	mm ²	-
	H	Plug Length	83	mm	2.075
Primary Bellow	ϕ_{5a}	Diameter	101.6	mm	1
	A_{5a}	Cross-sectional Area	8107.32	mm ²	-
	$\phi_{5a,e}$	Exhaust Diameter	50.8	mm	0.5
	L_a	Length	175.2	mm	1.724
Auxiliary Bellow	ϕ_{5b}	Diameter	101.6	mm	1
	A_{5b}	Cross-sectional Area	8107.32	mm ²	-
	$\phi_{5b,e}$	Exhaust Diameter	25.4	mm	0.25
	L_b	Length	87.6	mm	0.862
Initial Conditions	p_4	C.T. Pressure	9.122	bar	0.949
	ρ_4	C.T. Density	188.17	kg/m ³	0.679
	p_1	Reservoir Pressure	1	bar	0.109
	ρ_1	Reservoir Density	8.69	kg/m ³	0.031
	p_{5a}, p_{5b}	Bellow He Pressures	3.56	bar	-
	ρ_{5a}, ρ_{5b}	Bellow He Density	0.6827	kg/m ³	-

Table 5.1: Geometric Parameters of the FOV and Initial Conditions of the driver and driven gas. The geometric parameters are normalized by the corresponding diameters and the thermodynamic properties are normalized using the critical point values.

where n_s is the isentropic exponent discussed in Section 4.1.3, calculated using FluidProp for the real gas, and the subscript 'o' represents the initial thermodynamic states.

The pressure in CV_{52} is evacuated through the outlet orifice to the LPP. Cunningham [34] observed that unlike well-shaped Convergent-Divergent (CD) nozzles, orifices have been observed to not reach a choked condition. Instead, a *vena contracta* is created at the discharge and its throat diameter and distance from the discharge decrease continuously as the pressure ratio is decreased from the critical value to zero, defined as the supercritical range of ratios. Due to the highly dissipative nature of such a discharge, an inviscid formulation is not feasible. The author addresses this problem by developing an empirical formula describing the supercritical discharges of compressible flow through orifices [22]. This formulation is expressed as:

$$\dot{m} = CYA\sqrt{2\rho\Delta p} \quad (5.3)$$

$$C = 0.608 + 0.415\beta^4 \quad (5.4)$$

$$Y = 1 - (0.41 + 0.35\beta^4)\frac{1-r}{r} \quad r \geq 0.63 \quad (5.5)$$

$$Y = Y_{0.63} - 0.3501(0.63 - r) \quad r < 0.63 \quad (5.6)$$

where \dot{m} represents the mass flow rate, C is the discharge coefficient, Y denotes the expansion factor, $Y_{0.63}$

is the expansion factor from Equation 5.5 evaluated at $r = 0.63$, r is the ratio of pressures before and after the orifice and β is the ratio of the hydraulic orifice diameter to the diameter of the upstream duct. The parameters β and r for the discharge from CV_4 to the driven section are defined as:

$$\beta_t = \frac{2(x-H)}{\phi_{5a} - (\phi_t + 2d_w)} \quad r_t = \frac{p_3}{p_4} \quad (5.7)$$

For the discharge from CV_{52} to the atmosphere, the parameters are expressed as:

$$\beta_d = \frac{\phi_{5a,e}}{\phi_{5a}} \quad r_d = \frac{p_{tank}}{p_5} \quad (5.8)$$

where ϕ_{5b} is taken as the distance between the primary and auxiliary bellows until it is greater than the outlet diameter of the primary bellow. The parameter β_d has been shown to be a controlling factor for the opening time of the bellows [22]. Combining Equations 5.1 through 5.3 results in an ordinary differential equation for the evolution of p_5 in the primary bellow:

$$\frac{dp_{52}}{dt} = \frac{\gamma}{L-x} p_{52} \left[u_p - C_{52b} Y_{52b} \frac{A_{52b}}{A_{52a}} \sqrt{2 \frac{p_{52} - p_{vac}}{\rho_{50}} \left(\frac{p_{50}}{p_{52}} \right)^{\frac{1}{\gamma}}} \right] \quad (5.9)$$

where L is the initial length of the control volume, x is the instantaneous position of the piston, p_{vac} is the pressure of the vacuum chamber and u_p is the instantaneous velocity of the piston. The governing equation for the motion of the auxiliary bellow can be derived using the same method. A similar approach for the control volume CV_4 provides an ODE for the evolution of p_4 :

$$\frac{dp_4}{dt} = \frac{-\gamma}{V_4 + xA_4} p_4 \left[u_p A_4 + C_4 Y_4 \pi \phi_t (x-H) \sqrt{2 \frac{p_4 - p_3}{\rho_{40}} \left(\frac{p_{40}}{p_4} \right)^{\frac{1}{\gamma}}} \right] \quad (5.10)$$

where V_4 is the instantaneous volume of the CV and ϕ_t is the inner diameter of the charge-tube. The variable port area between the piston and the charge tube walls is represented in the last term on the right hand side of the above equation as $\pi(x-H)$. The position of the piston, x , is expressed as:

$$x = \frac{du}{dt} \quad (5.11)$$

The ODE for the velocity of the piston, u_p , is obtained by applying a force balance on the free-body diagram of the piston:

$$\frac{du_p}{dt} = p_1 A_{ext} + p_4 A_4 - p_5 A_5 + k_b(x - x_0) \quad (5.12)$$

where A_{ext} is the the area of the piston exposed to the reservoir pressure and k_b and x_0 are the spring constant and the equilibrium extension of the bellow respectively. Equations 5.9, 5.10, 5.11 and 5.12 together completely define the motion of the FOV in the FAST setup.

5.2. MODEL ASSUMPTIONS

The following assumptions were made during the formulation of the model:

1. The flow is considered to be inviscid and one-dimensional. This is a valid assumption since it is only the pressure force that is exerted by the fluid on the piston that influences its motion. Since it is also assumed that the piston completely seals the throat of the setup, there can be no fluid between the FOV and the throat walls to exert viscous forces on the piston. The effect of viscous forces and hence the fluid viscosity can therefore be neglected.
2. The system is also assumed to be adiabatic since the process of shock generation is too fast for any significant heat transfer.
3. The bellows are assumed to function as massless, perfect springs with a spring constant k . This is done so as to reduce the complexity of the governing equations. Also, since the spring is assumed to be massless, its acceleration and hence the vibrations arising due to its recoil can be neglected.
4. Due to the large volume of gas in the CT, the pressure in CV_4 is modelled as a lumped quantity. Similarly, the pressures in the bellows are also treated as lumped parameters since we are more interested in the rate of discharge of the gas rather than its variation within the bellow. Therefore, the pressures p_4 , p_{51} and p_{52} can simply be written as a function of time and can be solved for using Ordinary Differential Equations (ODE).

5.3. EFFECT OF PISTON MOTION ON CHARGE TUBE PRESSURE

It was mentioned in Section 5.1 that the formulation presented above models only the piston motion in a single dimension but the pressures in the charge tube and the back-chamber are considered as lumped quantities. In other words, any change in pressure that is given by Equations 5.9 and 5.10 is assumed to affect the entire pressure in the CT and the bellow rather than the variation in the region closer to the moving piston. In reality, however, as the piston moves, the high pressure gas fills into the space that was earlier occupied by the piston and as a result, a weak expansion wave starts to propagate into the charge tube even before the driver has breached. The speed of the fluid in the immediate vicinity of the piston is equal to the piston speed. Correcting for the ideal gas isentropic exponent, the sound speed in region 3 can be expressed using one-dimensional acoustic equations as:

$$c_3 = c_4 + \left(\frac{1 - n_s}{2} \right) u_p \quad (5.13)$$

The pressure and temperature ratios across the expansion can be estimated using isentropic relations for a real gas:

$$\frac{P_3}{P_4} = \left(1 + \frac{1 - n_s}{2} \frac{u_p}{c_4} \right)^{\frac{2n_s}{n_s - 1}} \quad (5.14)$$

$$\frac{T_3}{T_4} = \left(1 + \frac{1 - n_s}{2} \frac{u_p}{c_4} \right)^{\frac{2n_s m_s}{n_s - 1}} \quad (5.15)$$

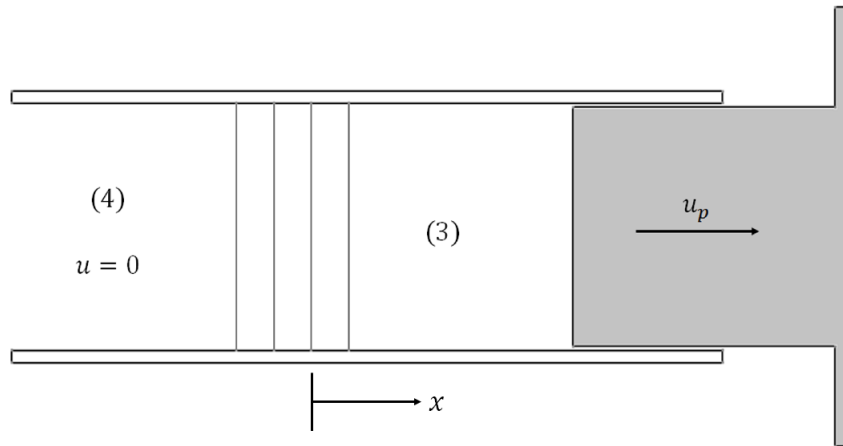


Figure 5.2: Expansion wave caused by motion of piston in a tube. As the piston accelerates within the tube, the gas expands to fill in the space occupied by the piston creating a series of expansion waves that propagate into the tube ahead of the final shock wave

where n_s and m_s are the isentropic exponents discussed in Section 4.1.3 and u_p is the instantaneous piston velocity. u_p can be expressed in terms of the instantaneous piston displacement as:

$$u_p = x_p * t \quad (5.16)$$

Since the displacement and the velocity of the piston are already known as a function of time, Equations 5.14 and 5.15 can be used to compute the drop in pressure with distance due to the initial expansion wave due to piston motion. The inverted thermodynamic characteristics exhibited by dense gases can be clearly observed in Equations 5.13 to 5.15. Although the temperature and pressure drop across an expansion wave, it can be seen that the sound speed behind the expansion is greater than that of the fluid at rest.

5.4. ESTIMATION OF OPENING TIME

Unlike the rupture of a diaphragm wherein a shock wave is formed almost immediately, the motion of the FOV spans over a relatively large time interval that creates a series of disturbances in the flow field. These disturbances would then propagate for a finite distance before coalescing into a single shock front. The FOV opening must allow these disturbances to coalesce before reaching the end of the shock tube. In other words, the length of the shock tube places an upper limit on the maximum allowable FOV opening time.

We will define the opening time as the time taken for the FOV to move from the initial position to a distance of one plug-diameter from the breaching position as shown in Figures 5.3 and 5.4 when the upstream effects due to the presence of the FOV are the least. The new FOV has been designed with the aim of having an opening time of 5 ms.

5.5. PERFORMANCE EVALUATION OF FOV DESIGN

The methodology of the 1D analytical model for the motion of the FOV was described in Section 5.1 and the results of the analysis are provided here. The inputs to the model include the mechanical properties of the driver and the thermodynamic initial state of the fluid, shown in Table 5.1. The model computes the

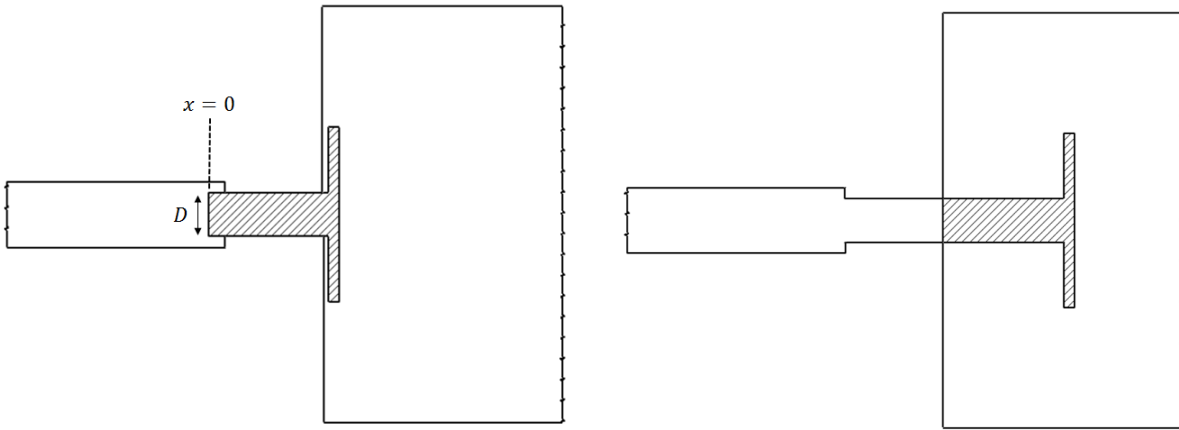
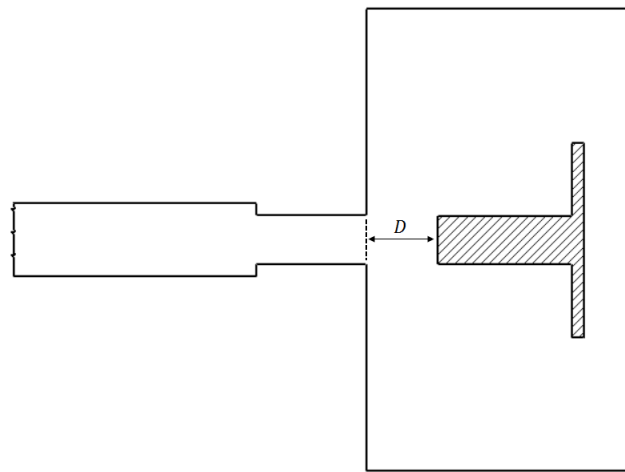


Figure 5.3: (Left) Initial and (Right) Breaching position of the FAST FOV driver

Figure 5.4: Definition of opening time for FAST FOV - time taken for the FOV to move from $x = 0$ till a distance equal to D from the breaching position

variation of the displacement and the velocity of the piston with time. From the displacement of the piston, the opening time can be estimated by using the definition provided in Section 5.4. The opening time of the bellow is calculated based on the definition provided in Section 5.4. The total distance that the piston needs to move in order to consider the driver to be open is equal to the sum of the length of the plug and the diameter of the throat, which here is 0.109 m. The opening time of the new FOV design is thereby estimated to be 18.13 ms, which is approximately 3.5 times larger than the proposed time of 5 ms. The displacement and velocity profiles of the FOV motion are shown in Figure 5.5. The drop in pressure and temperature behind the piston due to its initial motion before breaching are modelled as described in Section 5.3 and are shown in Figure 5.6.

This large opening time of the driver can be attributed to the presence of the auxiliary bellow which blocks the outflow of helium from the primary bellow as shown in Figure 5.7. As the auxiliary bellow compresses, the length of the opening Δx along the sides of the bellows for the Helium from the primary bellow to escape into the LPP increases. Till this opening is equal to or larger than the primary bellow outlet diameter $\phi_{e,p}$, the exhaust of Helium into the LPP will be governed by Δx . This causes the bellow to initially accelerate slowly. Once $\Delta x \geq \phi_{ce,p}$, the amount of Helium that is emptied into the LPP increases thereby helping the piston achieve a greater speed during breaching. This effect can be clearly seen in Figure 5.5 where the slope of the curves, which is initially flat, steepens after a certain time when the auxiliary bellow has cleared the exhaust

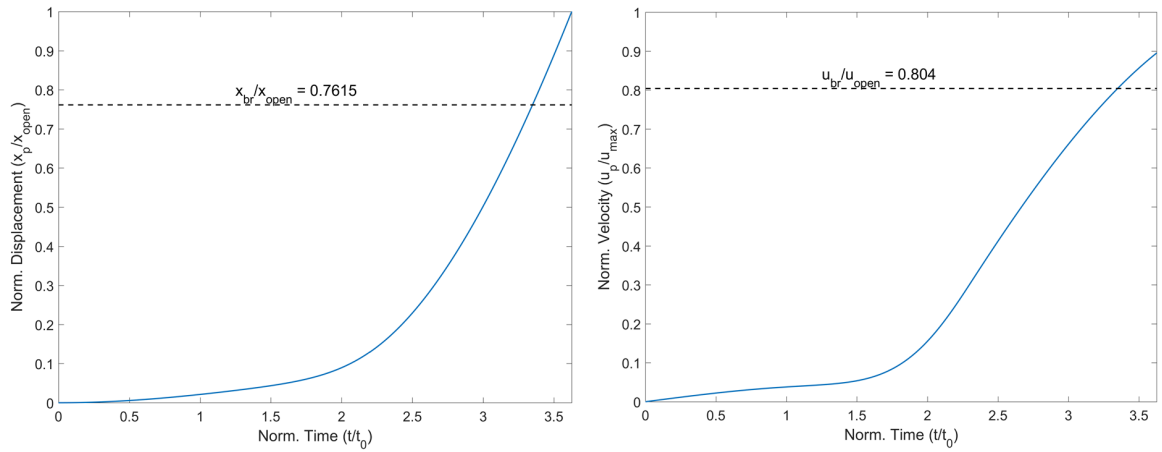


Figure 5.5: Displacement and velocity curves for the New FOV Design; The displacement is normalized with the FOV opening distance, the velocity with the maximum FOV velocity and the time with the proposed opening time of 5 ms

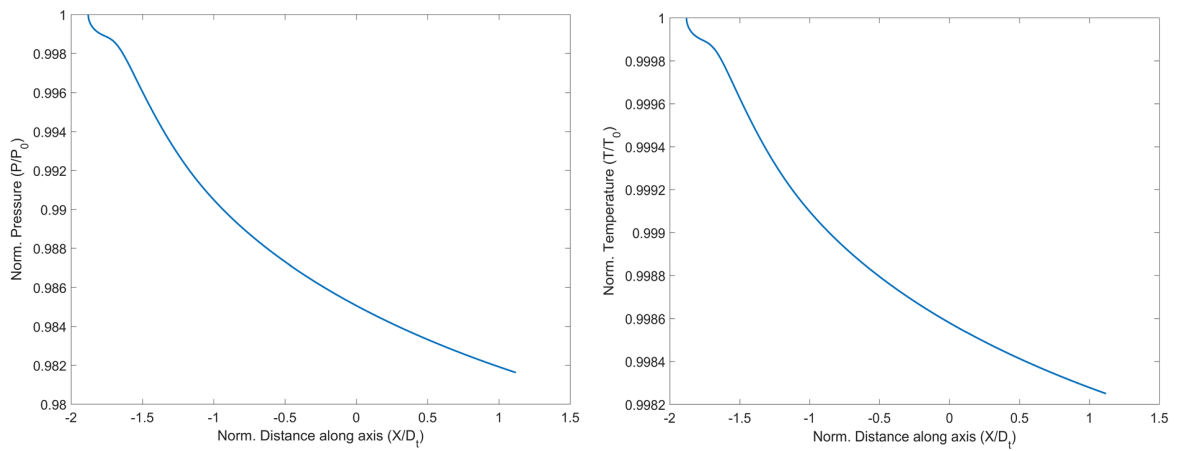


Figure 5.6: Drop in pressure and temperature across expansion wave generated by initial piston motion; The pressures and temperatures are normalized with the corresponding CT values and the distance is normalized with the throat diameter

of the primary bellows.

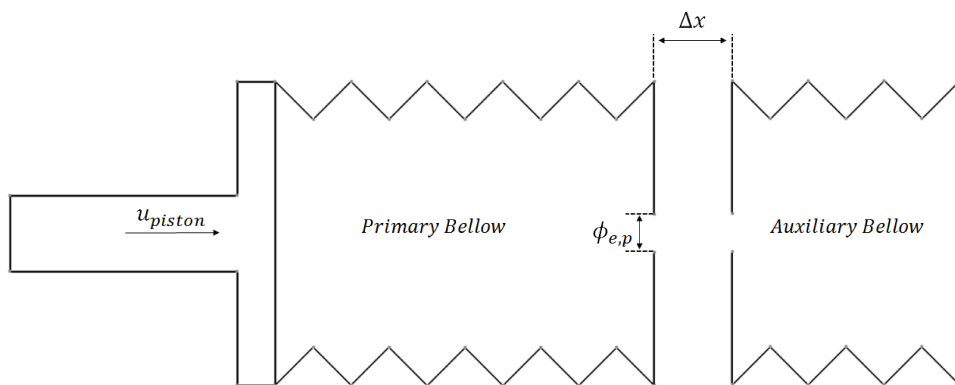


Figure 5.7: Schematic of the effect of auxiliary bellows on the exhaust of the primary bellows; As long as $\Delta x \leq \phi_{e,p}$, the rate of Helium exhausted into the LPP will be governed by the gap between the bellows.

5.6. EFFECT OF β_d ON FOV OPENING TIME

It was mentioned in Section 5.1 that the ratio of the orifice to the bellow diameter, β_d , is a critical parameter that affects the opening time of the driver. In order to investigate its influence, the β_d value of the auxiliary bellow was varied without changing that of the primary bellow and the opening times for each configuration was noted. Figure 5.8 shows the variation of the piston displacement with β_d for the auxiliary bellow.

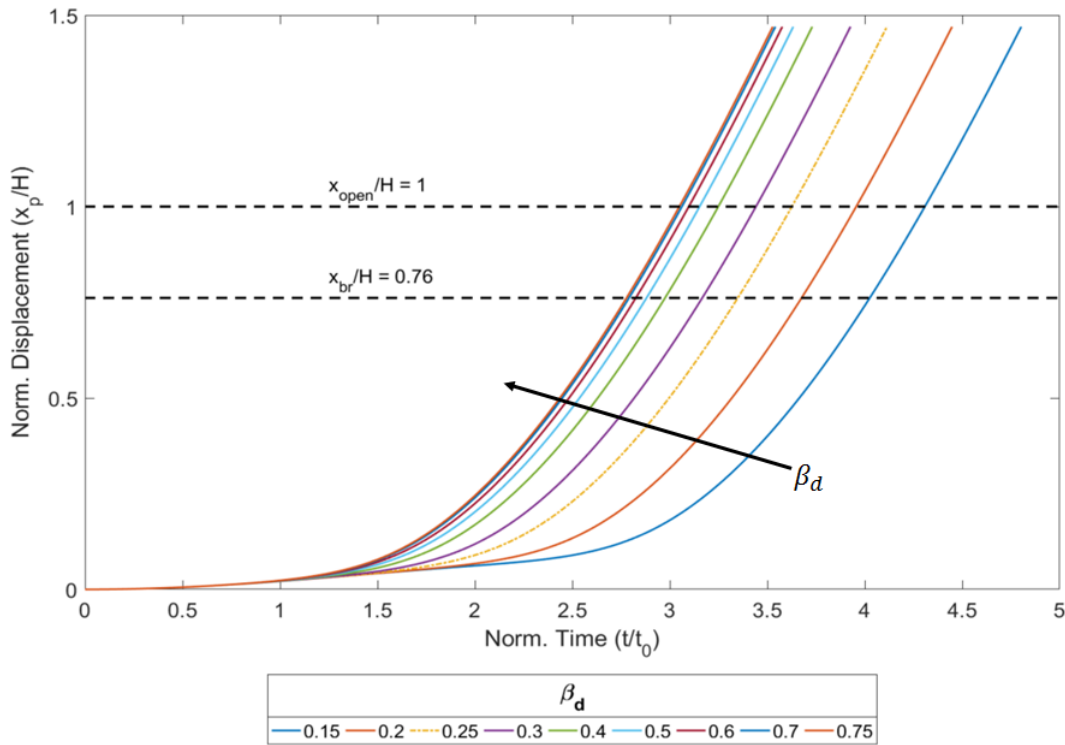


Figure 5.8: Variation of the FOV displacement with time for various auxiliary bellow β_d . Given the limiting value of β_d is 0.5, these curves indicate that the exhaust diameter of the auxiliary bellow can be increased further to reduce the FOV opening time. Variation of the FOV velocity with time for various primary bellow β_d . Unlike the auxiliary bellow, increasing the β_d of the primary bellow increases the velocity of the FOV. The time axis is normalized with the proposed design opening time of 5 ms and the displacement is normalized using the opening distance of 0.109 m.

The β_d value of 0.25 for the current configuration is shown in dotted lines. It can be seen from the figure that time taken for the piston to breach and the opening distance decreases steadily with increasing β_d till a value of 0.6. For $\beta_d > 0.6$, the change in β_d is observed to have little to no effect on the opening characteristic. The limiting value of β_d , denoted as $\beta_{lim,ab}$ is 0.6. In other words, it is necessary that the auxiliary bellow outlet orifice is at least 60% of the bellow diameter to ensure that the bellow is vented in the lowest possible time. This can also be inferred from the plot of the velocity profiles of the piston with varying β_d shown in Figure 5.9.

The slope of the curves remains unchanged as they are just offset to a reduced time for various values of β_d . The results indicate that the auxiliary bellow has little influence over the maximum speed or displacement of the piston but can only determine how soon those values are reached. The auxiliary bellow controls the rate at which the piston moves indirectly through the primary bellow. As explained in Section 5.6, the auxiliary bellow obstructs the exhaust of the primary bellow during start-up until it has moved a distance equal to the outlet diameter of the primary bellow. Therefore, the sooner the auxiliary bellow is vented, the lesser is the obstruction for the primary bellow and hence the piston. Therefore, the opening time of the FOV can be

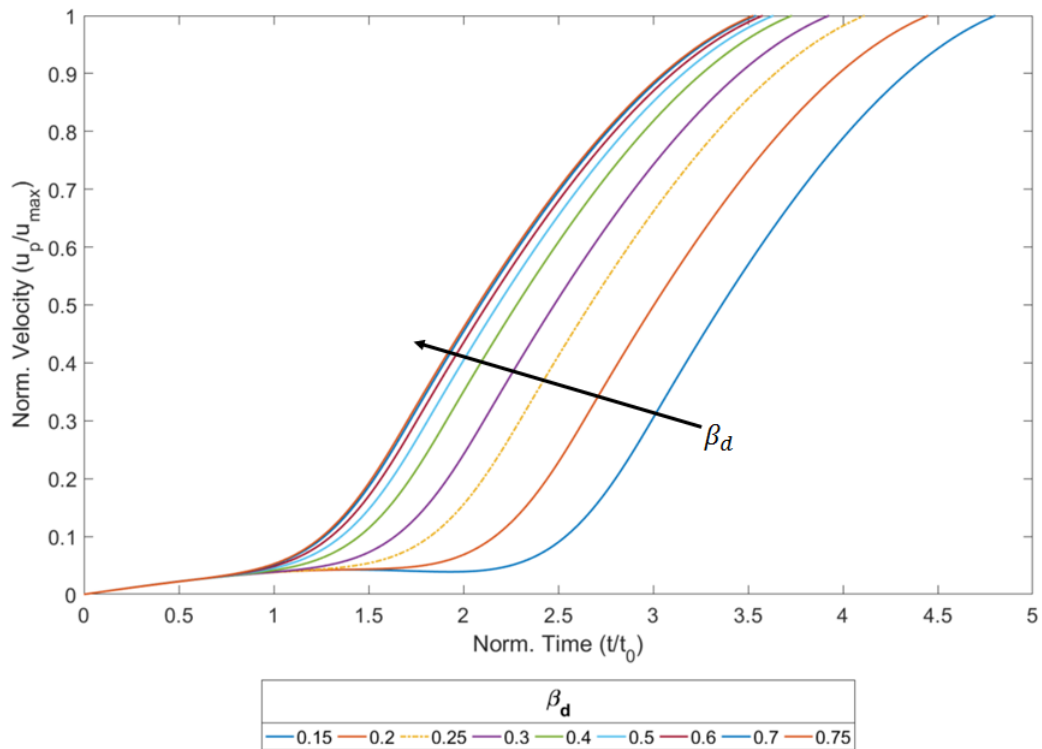


Figure 5.9: Variation of the FOV velocity with time for various auxiliary bellow β_d . Similar to the displacement curves, increasing the β_d value of the auxiliary bellow effectively displaces the curves to the left of the time axis while keeping the shape of the curve the same.

The time axis is normalized using the proposed design opening time of 5 ms and the velocity axis is normalized by the maximum velocity of the design FOV motion

expected to decrease with increasing size of the auxiliary bellow outlet orifice.

A similar study is also performed for the primary bellow by varying its β_d without changing that of the auxiliary bellow and the results are shown in Figure 5.10 and 5.11. The β_d value of 0.5 for the design case is shown in dotted lines. It can be observed from the figures that the value of $\beta_{lim,pb}$ is 0.5 as the performance curves show no change for $\beta_d > 0.5$. Unlike previous case, it can be seen that the maximum velocity of the piston increases and the displacement and velocity curves get progressively steeper with increasing β_d . Thus, it can be inferred that the primary bellow has a direct effect on the velocity and the acceleration of the barrier element. This is due to the fact that the primary bellow is mechanically attached to the piston and therefore, the sooner it vents, the lower is the resistance for the piston to move. It can also be observed from the plots that upto approximately two times the intended opening time of 5 ms, the behaviour of all the configurations are similar. This is due to the fact that upto this point, the piston motion is governed by the venting of the auxiliary bellows whose outlet diameter has been held constant. Once the auxiliary bellow has cleared the exhaust of the primary bellow, the performance curves diverge depending on the value of β_d . Since the design β_d value of the primary bellow is already equal to the limiting value, it can be said that the primary bellow is operating at its maximum efficiency.

Thus, while the β_d value of the primary bellow chosen during the preliminary design is equal to the limiting case, the value of the auxiliary bellow was lower than $\beta_{lim,ab}$. It can therefore be concluded that changing the β_d value of the auxiliary bellow will have a greater impact on the opening time of the piston than that of the primary bellow. This conclusion is corroborated by Figure 5.12 in which the opening time for the configurations studied above are plotted with β_d . It can be seen from this figure the opening time of the FOV

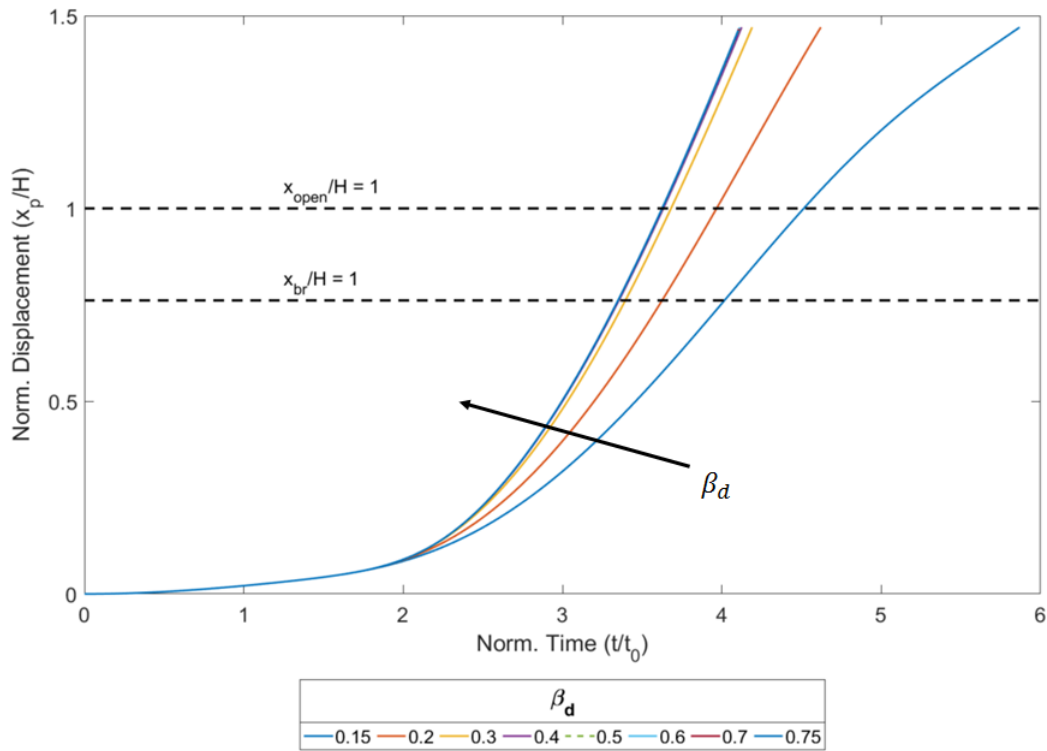


Figure 5.10: Variation of the FOV velocity with time for various primary bellow β_d . Unlike the auxiliary bellow, increasing the β_d of the primary bellow increases the velocity of the FOV. The time axis is normalized with the proposed design opening time of 5 ms and the displacement is normalized using the opening distance of 0.109 m.

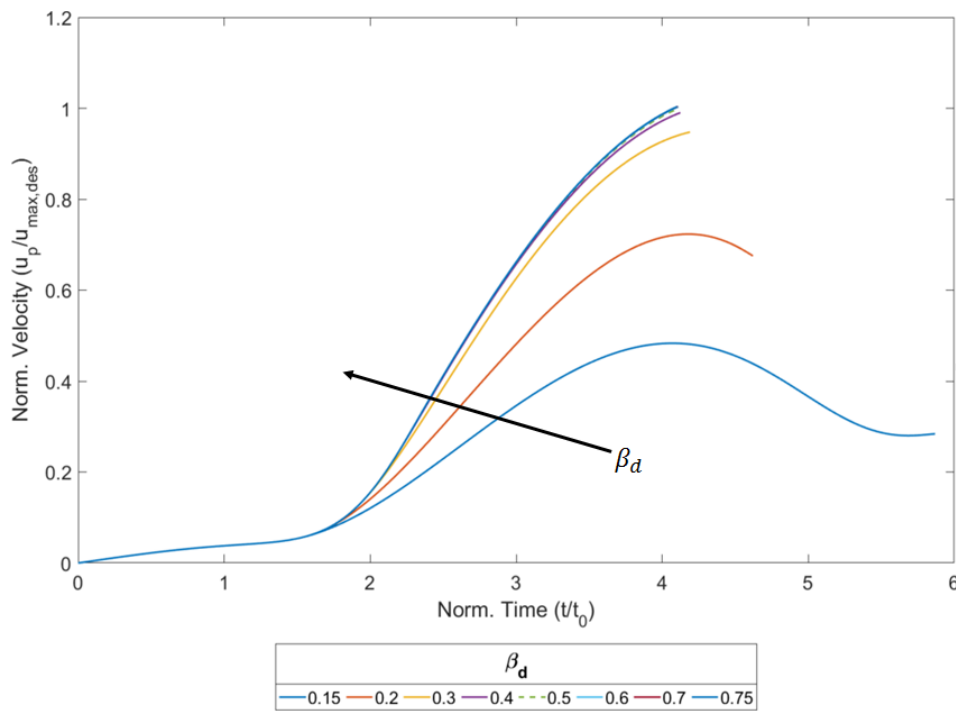


Figure 5.11: Variation of the FOV velocity with time for various primary bellow β_d . Similar to the displacement profile, the FOV acceleration increases with increasing primary bellow β_d . The time axis is normalized using the proposed design opening time of 5 ms and the velocity axis is normalized by the maximum velocity of the design FOV motion.

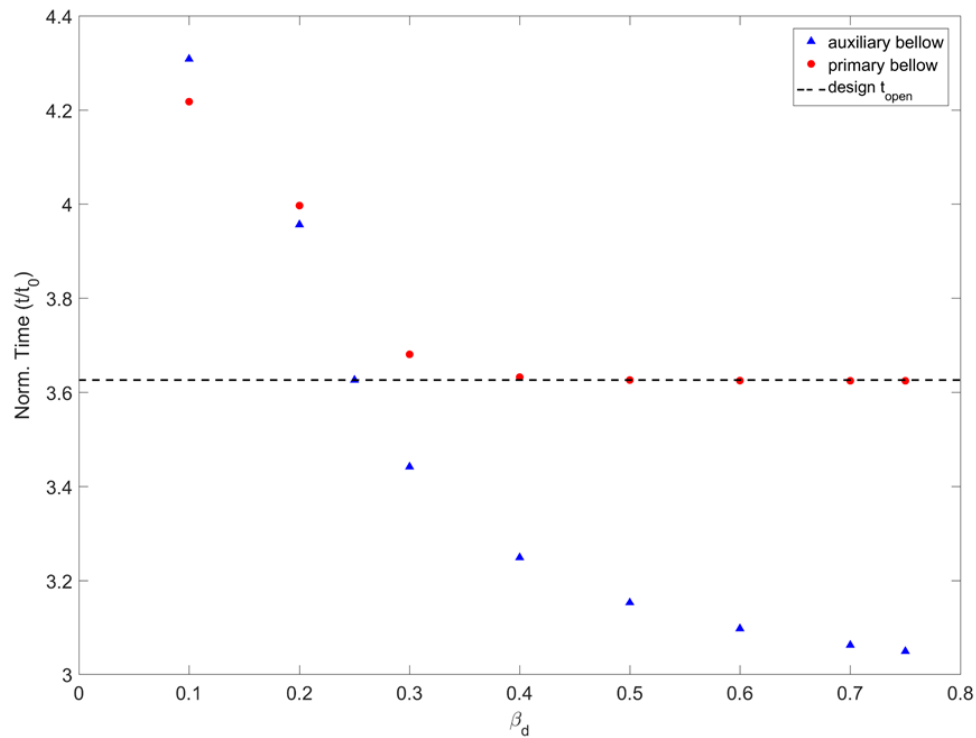


Figure 5.12: Effect of the exhaust diameters of the primary and auxiliary bellows on the FOV opening time. Due to the design β_d of the primary bellow already being equal to the limiting value, it has little influence on the opening time of the FOV while increasing the auxiliary bellow exhaust diameter can effectively reduce the opening time by nearly 20%.

can be reduced by nearly 2.5 ms by increasing the auxiliary bellow β_d from the design value of 0.25 to 0.6. The auxiliary bellow outlet diameter must therefore be increased from the current 25 mm to a value of 61 mm to achieve a lower opening time. Increasing β_d of the primary bellow, on the other hand, has no effect on the opening time of the FOV since it is already operating at its maximum condition.

5.7. SUMMARY

A one-dimensional model for the characterisation of the FOV motion was presented in this chapter. The results of the model suggest that the new conceptual design of the FOV has a opening time of 18.13 ms which is more than three times the design opening time of 5 ms. The sensitivity of the opening time of the valve to the value of β_d was also discussed and was shown that the opening time can further be reduced by increasing the auxiliary bellow exhaust diameter. The motion of the FOV obtained from this model will be used in the computational analysis discussed in Chapter 6 to assess its impact on the shock formation in the FAST setup.

6

COMPUTATIONAL MODELLING OF THE FAST OPENING VALVE

This chapter provides an overview of the theory behind the computational modelling of the Flexible Asymmetric Shock Tube experiment and the motion of the Fast Opening Valve. In this thesis, a numerical study of a simplified model of the FAST facility with the FOV motion is performed to understand dense-gas flow behaviour and to characterize the FOV motion.

6.1. REYNOLD'S AVERAGED NAVIER-STOKES EQUATION

The governing equations that physically characterize the flow are the equations for the conservation of mass, momentum and energy, together called the Navier-Stokes (NS) equations [35]. These conservation of mass equation is expressed as:

$$\frac{\partial \rho}{\partial t} + \frac{\partial(\rho u_i)}{\partial x_i} = 0 \quad (6.1)$$

the equation for momentum conservation, which is also called the Navier-Stokes equation:

$$\frac{\partial(\rho u_i)}{\partial t} + \frac{\partial(\rho u_i u_j)}{\partial x_j} = -\frac{\partial p}{\partial x_i} + \frac{\partial \tau_{ij}}{\partial x_j} \quad (6.2)$$

where the stress tensor τ_{ij} is expressed as:

$$\tau_{ij} = \mu \left[\left(\frac{\partial u_i}{\partial x_j} + \frac{\partial u_j}{\partial x_i} \right) - \frac{2}{3} \delta_{ij} \frac{\partial u_j}{\partial x_i} \right] \quad (6.3)$$

where μ is the dynamic viscosity and the equation for the conservation of energy:

$$\frac{\partial}{\partial t} [\rho(e + \frac{1}{2} u_i u_i)] + \frac{\partial}{\partial x_j} [\rho u_j (h + \frac{1}{2} u_i u_i)] = \frac{\partial}{\partial x_j} (\tau_{ij} u_i) - \frac{\partial q_j}{\partial x_j} \quad (6.4)$$

Various approaches such as the Direct Numerical Simulation (DNS), Large Eddy Simulation (LES) and Reynold's Averaged Navier-Stokes (RANS) approaches are used for modelling turbulence.

The most 'exact' approach to solve this system of equations is Direct Numerical Simulation which solves the fluid down to the smallest length and timescales. This provides highly detailed information about the flow field but the computational cost increases rapidly at high Reynold's numbers. This is due to the fact that a finer mesh is required to accurately capture the turbulent flow field and the required number of cells is proportional to the cube of the Reynold's number. Due to their high computational loads and time, DNS approach is chiefly used only in low-Re applications with small domains. An intermediate approach is the LES method which by means of a filtering approach applied to the N-S equations, explicitly computes the large scale turbulence eddies while modelling the small scale motions. Though this method is accurate, the computational cost is still very high [36].

For this research, the RANS approach is used due to reduced computational cost and its wide use in engineering applications. Due to the large size of the computational domain and the use of mesh motion and remeshing techniques, the computational overhead is an important constraint that affected the selection of the turbulence model. In the RANS approach, the NS equation for the turbulent flow field is solved by decomposing the fluctuating variables into a time-averaged and a fluctuating part in a process called as Reynold's decomposition:

$$u_i = \bar{u}_i + u_i' \quad (6.5)$$

where \bar{u}_i and u_i' represent the time-averaged and the fluctuating quantities. The time-averaged component is obtained by applying the Reynold's time-average operator locally to the velocity vector:

$$\bar{u}_i = \frac{1}{\Delta t} \int_{t_0}^{t_0 + \Delta t} u_i dt \quad (6.6)$$

By applying Equation 6.6 to all the variables in the NS equations, the time-averaged NS equations are obtained. However, this decomposition gives rise to extra unknown terms known as the Reynold's Stress Terms (RST) which includes the fluctuating component of velocity. As such, the RANS equations don't constitute a closed system and it is necessary to model the stress terms to solve the equation. Various turbulence models have been created for this purpose.

6.2. TURBULENCE MODELLING

As mentioned in the previous section, turbulence models have been developed to deal with the closure problem in the RANS approach due to the presence of the RSTs. One of the most widely used models in the RANS approach are the eddy viscosity models which relate the Reynold stresses to the eddy viscosity, ν_T and the turbulence kinetic energy, k as follows:

$$\tau_{ij} = 2\nu_T S_{ij} - \frac{2}{3}\delta_{ij}k \quad (6.7)$$

where S_{ij} is the shear rate and δ_{ij} is the kronecker delta function. These models use two additional equations to model the turbulence. Two different approaches, namely the $k - \epsilon$ and $k - \omega$ models can be used to relate the turbulence kinetic energy to the eddy viscosity. In the $k - \epsilon$ model, additional equations are used to compute the turbulence kinetic energy and the turbulence eddy dissipation ϵ and the turbulence viscosity (ν_T) is determined as a function of k and ϵ . While this model is well-suited for external flows, it is not suitable for predicting rotating flows and flows with strong separation [37].

The $k - \omega$ model utilizes turbulence dissipation rate, ω . As in the $k - \epsilon$ model, two additional equations are solved to compute the k and ω terms which are then used to determine the eddy viscosity. In contrast to the $k - \epsilon$ model, the $k - \omega$ model is capable of predicting internal flows [38] and flows that encounter adverse pressure gradients but can overestimate the turbulence in stagnation regions and shows strong sensitivity to the free-stream boundary conditions.

A third model, called the $k - \omega$ SST model, combines the best features of both the $k - \omega$ and $k - \epsilon$ models by switching between the two models in the boundary layer and the free-stream conditions respectively. Therefore, it provides a more accurate representation of boundary layer flows while being insensitive to the free-stream conditions [39]. Therefore, the SST model is used for this thesis work.

6.3. CFD SIMULATION SETUP

In this section, computational aspects such as geometry and mesh creation, solver initialization and mesh and geometry sensitivity analyses are discussed.

6.3.1. GEOMETRY

A two-dimensional representation of the FAST experimental facility is made in ICEM CFD. The geometry consists of a 9 m long CT that is connected to the LPP via a throat of 26 mm diameter. The solid piston-plug FOV is modelled as a moving wall within the LPP. A schematic of the FAST geometry is given in Figure 6.1 and the geometrical parameters are provided in Table 6.1. Though the FAST setup features a cylindrical shaped pressure vessel with curved ends, the curvature of the tank results in a poor quality mesh especially during mesh motion. To avoid this, the tank is modelled as a straight ended cylinder while maintaining the volume a constant as shown in Figure 6.2.

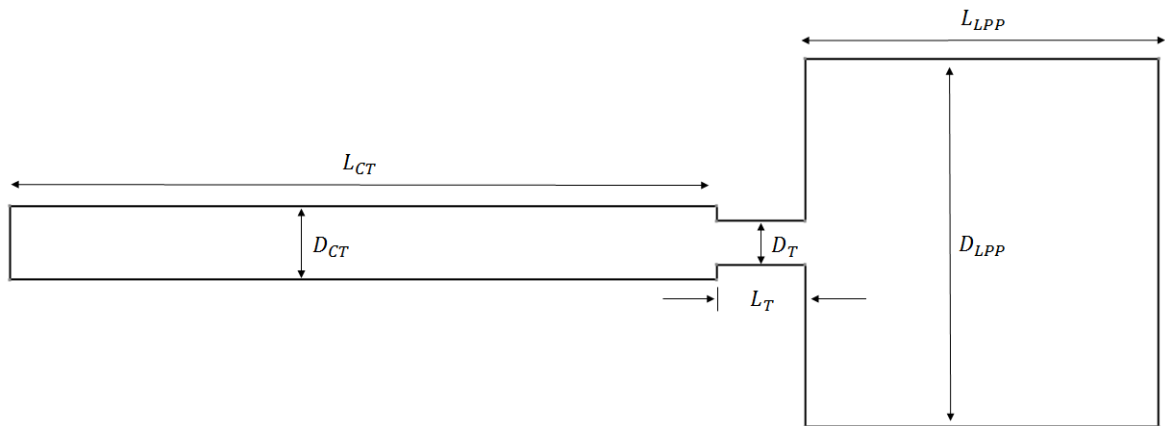


Figure 6.1: Schematic of FAST geometry with characteristic dimensions

	Symbol	Parameter	Value	Units	Dimensionless Value
Characteristic Dimensions	D_{CT}	CT diameter	40	mm	1.54
	L_{CT}	CT length	9	m	346.15
	A_{CT}	CT cross-sectional area	1256	mm ²	-
	V_{CT}	CT internal volume	0.01256	m ³	-
	D_T	Throat diameter	26	mm	1
	L_T	Throat length	58	mm	2.23
	A_T	Throat cross-sectional area	531.2	mm ²	-
	D_{LPP}	LPP diameter	387.34	mm	14.89
	L_{LPP}	LPP Length	0.958	m	36.84
	V_{LPP}	LPP volume	0.113	m ³	-

Table 6.1: Characteristic dimensions of FAST geometry [20]. All the non-dimensional parameters are expressed in terms of the throat diameter.

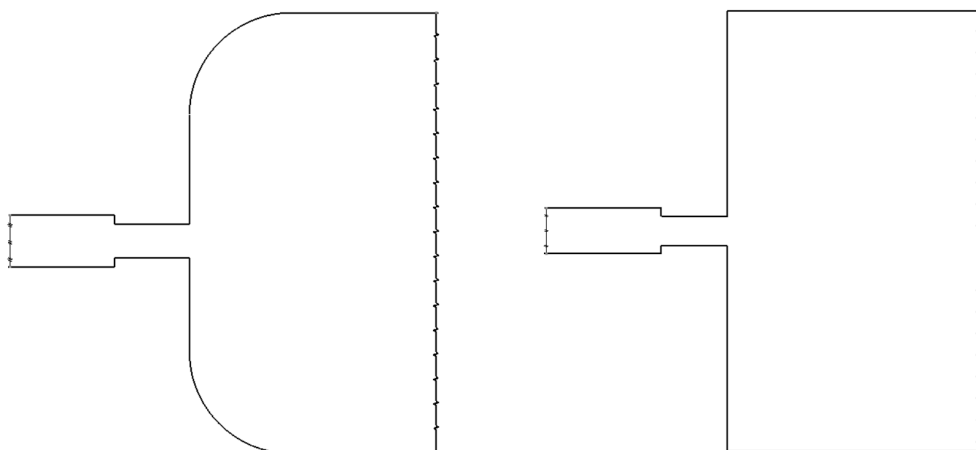


Figure 6.2: Schematic of actual (left) and modelled (right) LPP geometries. The curved walls of the LPP result in the generation of poor quality meshes during mesh motion making its use unsuitable.

6.3.2. MESHING

A structured hexahedral mesh is created for the FAST geometry in ICEM CFD using the blocking technique. In this process, the computational domain is divided manually into multiple blocks and the mesh parameters such as mesh density, first cell thickness, etc., are specified for each block. An important parameter that ensures good accuracy especially in the boundary layer region is the non-dimensional wall distance y^+ given as follows:

$$y^+ = \frac{u_* y}{\nu} \quad (6.8)$$

where the wall friction velocity u^* is defined as:

$$u^* = \sqrt{\frac{\tau_{wall}}{\rho}} \quad (6.9)$$

in which τ_{wall} is the shear stress at the wall, y is the first cell thickness and ν is the kinematic viscosity. For accurately predicting flows within the boundary layer, the value of y^+ must be less than or equal to 1. Since the value of y^+ can be estimated only from the CFD results, the wall distance y is altered in an iterative procedure to arrive at the preferred value of y^+ . An important feature in ICEM CFD is the ability to record and replay the commands used during the geometry and mesh generation process. Since the FOV is modelled to move during the course of the simulation, the geometry and the grid vary with each time-step. Changing the geometry and the grid manually at each iteration would be a tedious process. Using the replay file, this process is autonomously implemented by the software which can maintain mesh quality as described in Section 6.3.5.

6.3.3. SOLVER

Once the mesh is generated, it is transferred to the solver. ANSYS CFX is used for this purpose due to its simple interface and the ability to directly read the real gas property (.rgp) files for real gases, which is necessary to simulate flows in D_6 . The .rgp file contains the thermodynamic properties of a real gas in the form of look-up tables. The .rgp file for D_6 is generated using FluidProp. As mentioned in Section 6.2, the RANS approach with the $k-\omega$ SST turbulence model is used in the simulations. A density-based solver is used to account for the compressibility effects and higher order numerical schemes are applied to improve the accuracy of the solution. Since the flow is expected to be supersonic and the fluid is highly viscous, the kinetic energy and the viscous heating effect terms also are included in the energy equation.

6.3.4. PROBLEM SETUP

Once the mesh is loaded into CFX, relevant information such as the initial values and the boundary conditions must be set for the solver to solve for the flow. The B.C. of the computational FAST geometry are shown in Figure 6.5. Since the FAST is a shock tube, there are no inlet or outlet B.C.s. in the model. The piston is modelled as a moving wall. The displacement of the piston as a function of time (Figure 5.5) obtained from the performance evaluation of the FOV in Chapter 5 is input as a CEL expression in CFX to define the wall motion. The external boundaries of the model are all modelled as no-slip walls (red) while the symmetry

B.C. (green) is applied to the front and back faces of the model. The initial conditions for the simulations are described in Table 3.1.

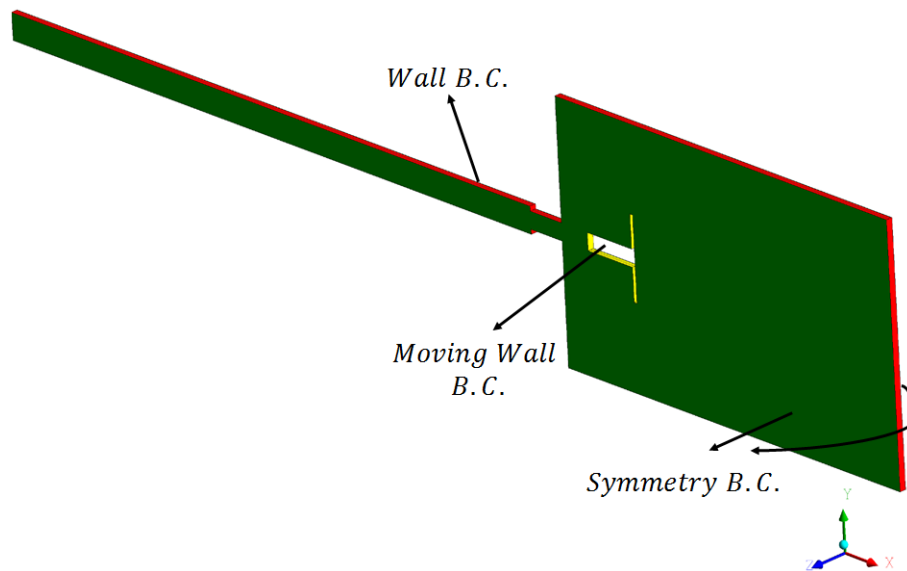


Figure 6.3: Schematic of FAST geometry showing the boundary conditions defined for the simulation

The time-step of the transient simulation is chosen based on the Courant-Friedrich-Levy's (CFL) number, shown in Equation 6.10, which is an important parameter that determines the stability of the simulation:

$$CFL = u \frac{\Delta t}{\Delta x} \quad (6.10)$$

where u is the local flow velocity, Δt is the time-step and Δx is the length interval. Physically, the CFL number is the ratio of the length travelled by a fluid particle in one time-step to the mesh size. It is desired that the CFL number is kept at 1 for the accuracy and the stability of the numerical simulation. This condition is automatically satisfied for implicit solvers since the particle displacement is updated every time it crosses a computational cell. However, since CFX is an explicit solver, the time-step of the simulation must be adjusted accordingly to achieve a $CFL = 1$. A time-step of $1e-5$ [s] has been chosen for the current simulations to fulfil this condition. Since the flow velocity cannot be known before-hand, the time-step was found in an iterative process.

6.3.5. MESH MOTION AND REMESHING

As mentioned in Section 6.3.2 and in Chapter 1, the purpose of the CFD analysis is to understand the effect of the moving piston and its opening time on the generation of shock waves. The piston-plug's motion that was modelled in Chapter 5 is used in the computation. However, as the piston moves, the mesh is also dragged along with it thereby creating skewed cells and reducing the mesh quality, eventually causing convergence issues. To prevent this from happening, the mesh is automatically replaced by ICEM and CFX based on a user-defined Interrupt condition. For this simulation, the solver is interrupted whenever the minimum mesh orthogonality angle drops below 50° . Once this condition is met anywhere in the domain, CFX calls on and provides the piston position to ICEM where a new mesh based on the replay file created earlier is generated. This new geometry and mesh are again transferred back to CFX and the simulation is continued. More infor-

mation on setting up remeshing in the solver can be found in the CFX-Pre Guide[40].

In the FAST setup, the FOV is positioned such that during the experiment start-up, the plug of the piston blocks the throat of the setup and extends a short distance into the CT. A small clearance between the throat and the piston allows for the latter's smooth motion and thermal expansion. Similarly, CFX requires that there must be a gap that is at least one-cell thick between the stationary and the moving boundaries. However, the solver simulates a flow from the CT to the LPP through this small gap and the large pressure difference acting over a relatively small clearance creates convergence issues. To mitigate this problem, the motion of the piston is simulated as if starting from the breaching position (see Figure 6.4) and the pressure and temperature behind the piston that were affected due to its motion within the throat are modelled as shown in Section 5.3.

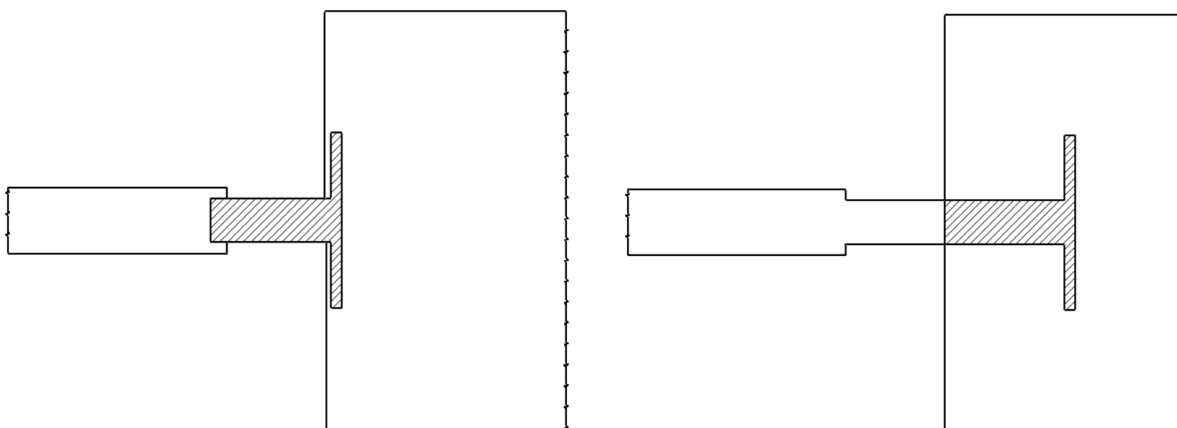


Figure 6.4: Schematic of the actual position (left) and the modelled position (right) of the FOV during initialization in the FAST setup

6.4. SENSITIVITY ANALYSIS

There are a variety of factors such as the mesh size, the CFL criterion, etc. that affect the solution of a computational simulation. It is therefore very important to prove that the solution is accurate and is independent of such factors. The two potential sources of error that can affect the accuracy of the solution in these simulations are the mesh and the change in geometry (see Section 6.3.1). To ensure that the solution is not affected by these factors, a sensitivity analysis is performed for both the cases.

6.4.1. GEOMETRY SENSITIVITY

In order to ensure that the change in LPP geometry has no effect on the solution, simulations were performed for both the straight and curved wall cases in D6 and the pressure in the charge tube was compared. The simulations were performed for an instantaneous expansion and the FOV motion was not considered. The pressures across the CT-throat interface were compared for both cases and it was observed that the change in the LPP geometry had no effect on the pressure of the flow field in the charge tube. Thus, the straight walled LPP geometry was chosen to model the LPP for further runs due to its simplicity in simulating mesh motion. The results of this analysis are shown in Figure 6.5 where the pressure is normalized with the CT pressure and the normal y-distance by the throat diameter.

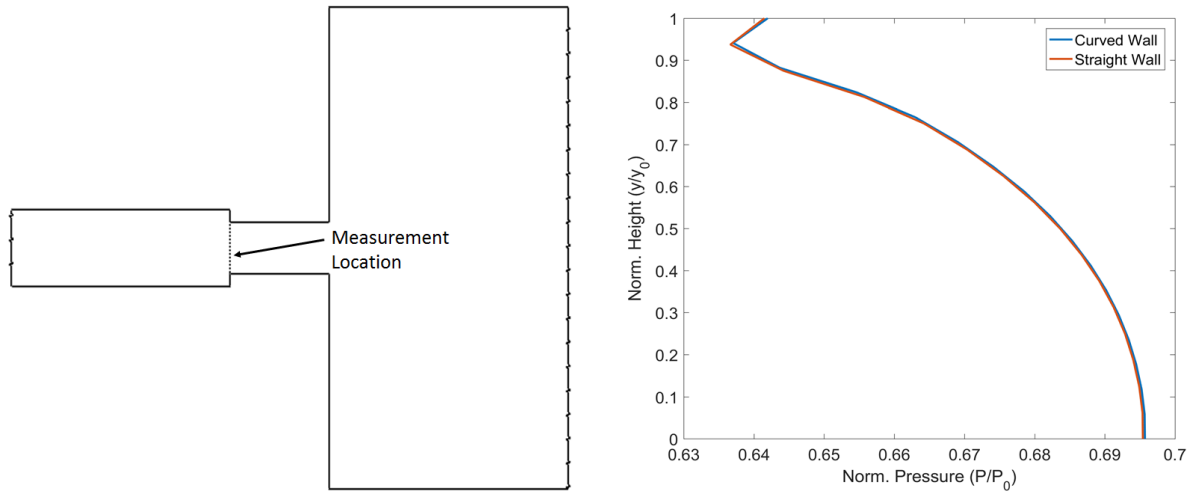


Figure 6.5: (Left) CT-throat interface at which the pressures are measured and (Right) Results of the geometry sensitivity study for the straight-walled and curve-walled LPP geometries at the CT-throat interface

6.4.2. MESH SENSITIVITY

Since the computational time required to solve for the flow increases exponentially with mesh count, a highly dense mesh inadvertently requires a high computational overhead and to prevent this, the mesh is refined. In this case, the average slope of the propagating shock wave in the CT is calculated for varying number of mesh elements and the results are shown in Figure 6.6. The slope of the shock wave is calculated as follows:

$$Slope = \frac{P_1 - P_2}{X_1 - X_2} \quad (6.11)$$

where 1 & 2 denote the pre-shock and post-shock states. It can be observed that the shock slope steadily increases till about 5.48 million mesh elements after which the change is less than 0.02% between 5.48 million and 6.5 million cells. The mesh count of 5.48 million cells was used for the simulations so as to improve the accuracy of the results and to prevent excessive computational time.

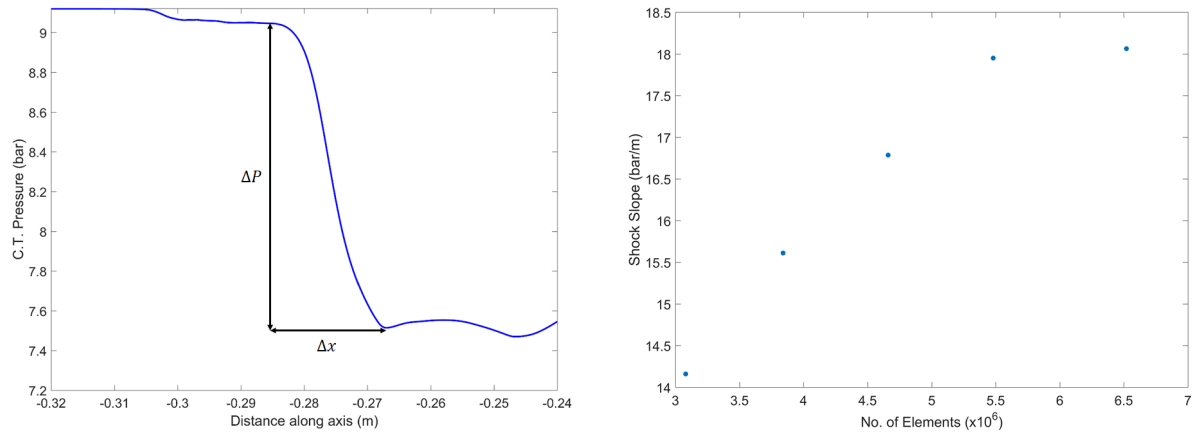


Figure 6.6: (Left) Example for the calculation of the slope of the shock wave and (Right) Results of the mesh sensitivity study for various mesh sizes comparing the shock slope

6.5. SUMMARY

The fundamental aspects of the computational simulation of the FAST experiment were presented in this Chapter. A quasi-3D geometry of the FAST is created in CFX and a refined grid based on the mesh sensitivity study is generated in ICEM. The piston is modelled as a moving wall by using CFX's and ICEM's mesh motion and replay features. A straight-walled geometry for the LPP is used unlike the curved tank of the original geometry so as to reduce complications while simulating mesh motion. A sensitivity analysis was also performed for this case and it was found that the change in LPP geometry had no effect in the flow field in the CT. The results and discussion of the numerical simulations are presented in Chapter 7.

7

ASSESSMENT OF THE CFD RESULTS

The computational model setup and solver initialization were described in Section 6.3 and the results of the simulations are discussed in this chapter. The simulations of the FAST gasdynamic experiment were performed for the cases of an ideal expansion assuming the opening of a diaphragm at time $t = 0$, the FOV opening time of 18 ms as estimated in Chapter 5 and the intended opening time of 5 ms from literature. Section 7.1 discusses the results of the ideal expansion case in which a diaphragm separating the high and low pressure sections is instantaneously opened at $t = 0$. Section 7.2 examines the results of the simulations that incorporate the FOV motion discussed in Chapter 5.

7.1. DIAPHRAGM-LIKE EXPANSION IN D6

First, the expansion of D6 in the FAST setup is simulated without the FOV but instead assuming the rupture of a diaphragm at time $t = 0$. This simulates the case of an ideal expansion where the diaphragm is opened instantaneously allowing for the sudden expansion of the high pressure gas into the reservoir. The results of this simulation can therefore be compared with that of the analytical model described in Chapter 4 to corroborate the CFD methodology.

In order to prove that a propagating wave is indeed a nonclassical shock wave, three conditions are checked:

1. The wave must be in the negative Γ region
2. The wave must propagate at supersonic speeds
3. The wave speed must be independent of the drop in pressure across the wave

To prove that the wave is indeed propagating at a $M > 1$, the speed of the wave is measured using the time of flight method as shown in Figure 7.1. The wave reaches the first transducer at time t_1 and the second one at time $t_2 = t_1 + \Delta t$. The wave velocity is then calculated as $u_w = \Delta x / \Delta t$ where Δx is the axial distance between the two transducers which in this case is 0.3 m. The presence of a shock wave can then be verified by plotting the variation of wave speed with the drop in pressure across the wave in which the shock manifests itself as a horizontal line in plot.

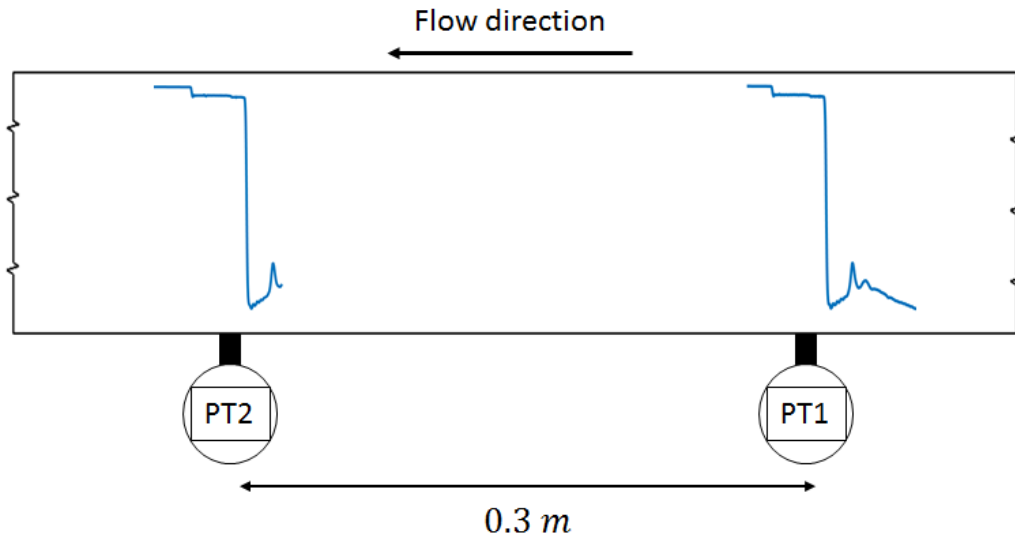


Figure 7.1: Schematic of the CT showing the wave propagation past the pressure transducers. The wave speed is calculated by dividing the distance between the sensors by the time taken for the wave to travel that length. This is done for every point at a given pressure along the wave to obtain the local wave propagation speed.

The pressure recordings at the location of the first two sensors PT1 and PT2 are shown in Figure 7.2. The red and the black lines denote the part of the wave where the fundamental derivative of gasdynamics Γ is negative, thus signifying nonclassical behaviour. The steep gradient in the pressure can in Figure 7.2. Figure 7.3 shows the variation of the wave speed, normalized using the model speed of sound in the fluid at rest, with the drop in pressure across the expansion wave. The figure indicates that between -0.02 and -0.12 on the horizontal axis, the wave speed remains constant with drop in pressure. The nonclassical part of the wave, denoted by the black dots, spans from -0.02 till -0.08 on the horizontal axis. In this pressure range, the wave is supersonic, nonclassical and the wave speed is independent of the drop in pressure, thus signifying the presence of a rarefaction shock wave.

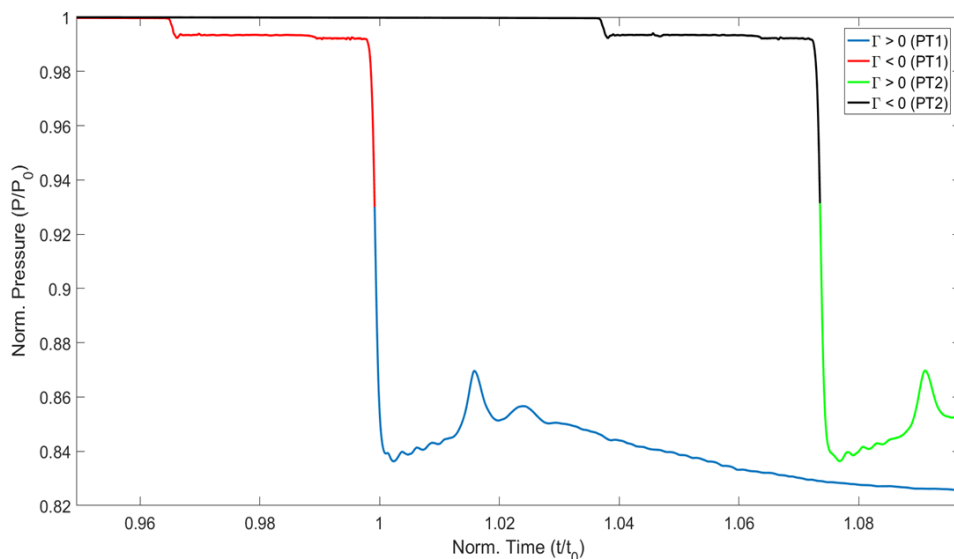


Figure 7.2: Profiles of pressure measured at sensors PT1 and PT2 for the diaphragm-like expansion case. The red and black line overlays depict the nonclassical part of the expansion wave. The wave speed is measured by dividing the axial distance between the two sensors by the time taken for the wave to travel from PT1 to PT2. The time axis is normalized by the mean time taken for the wave to travel between the sensors and the pressure is normalized by the charge tube pressure.

An important observation from Figure 7.3 is that the wave remains supersonic even outside the nonclassical region. This conforms with the prediction of a post-shock sonic state by the analytical model in Chapter 4. The post-shock pressure obtained from the CFD analysis is 8.04 bar which is approximately 0.25% higher than the value predicted by the analytical model while the wave Mach number of 1.019 is only 0.39% lower.

One major aspect of the flow field in the CT is the formation of an oscillatory wave pattern behind the shock wave which is different from the smooth expansion that is observed in a constant area shock tube. The difference in the diameter of the CT and the throat causes the propagating wave to diffract and form a spherical wave front at the throat-CT interface. A portion of the initial wave remains unchanged and propagates as a normal shock wave. The diffracted portion of the wave is reflected by the walls of the CT and this creates a series of oblique waves behind the leading shock wave as shown for the upper-half section of the CT in Figure 7.4. As the distance from the CT-throat junction increases, the diffracted portion of the shock wave becomes normal to the CT axis thereby creating an almost planar shock wave. However, a very small curvature still exists and this gives rise to a system of reflected compression and rarefaction waves that is symmetric about the shock tube axis [41], as shown in Figure 7.5. This system is seen as oscillations in the measured post-shock pressure in the CT which is observed behind the incident shock wave in Figure 7.6. As the wave propagates further upstream, the leading shock becomes completely planar and the rarefaction-compression system behind the shock wave disappears. This effect is seen in Figure 7.7.

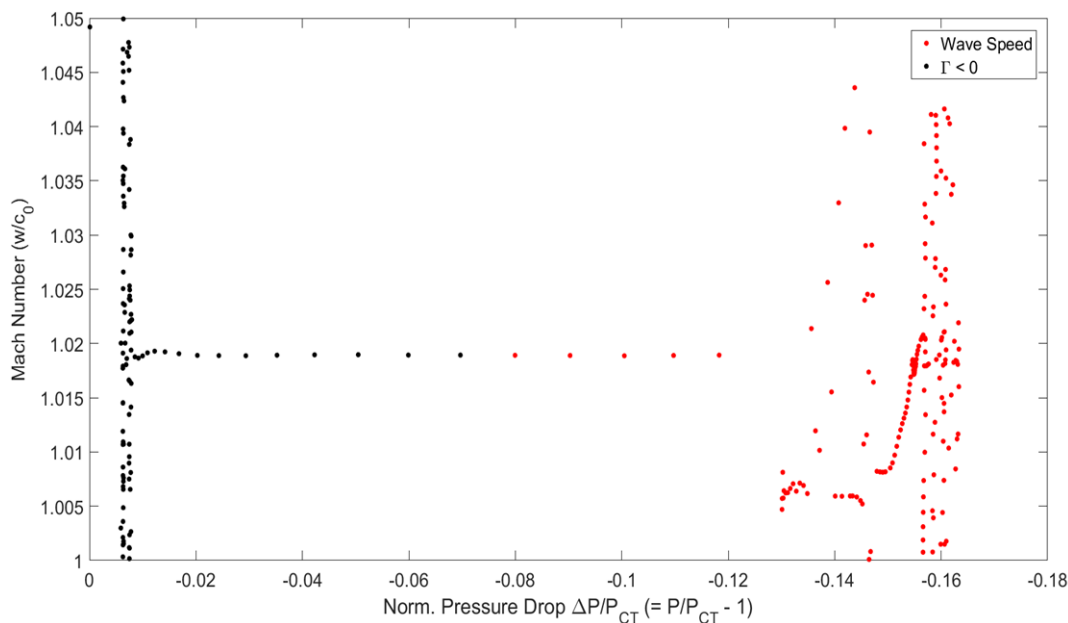


Figure 7.3: Variation of the wave speed with the drop in pressure across the expansion wave for a diaphragm-like expansion. The black dots signify the region of negative Γ . The wave speed is normalized by the local speed of sound in the fluid at rest in the CT.

It can also be observed from Figure 7.7 that the contours are concentrated over a small region indicating the presence of a shock wave. While the thickness of a classical compression shock wave is usually of the order of 10^{-7} m, the thickness of the RSW is calculated to be 5.5 mm.

7.2. EFFECT OF FOV MOTION ON SHOCK FORMATION

Through the simulation of an diaphragm-like case in D6, it was shown that a rarefaction shock wave can be observed in the charge tube at the location of the first pair of pressure transducers for the case of an ideal and

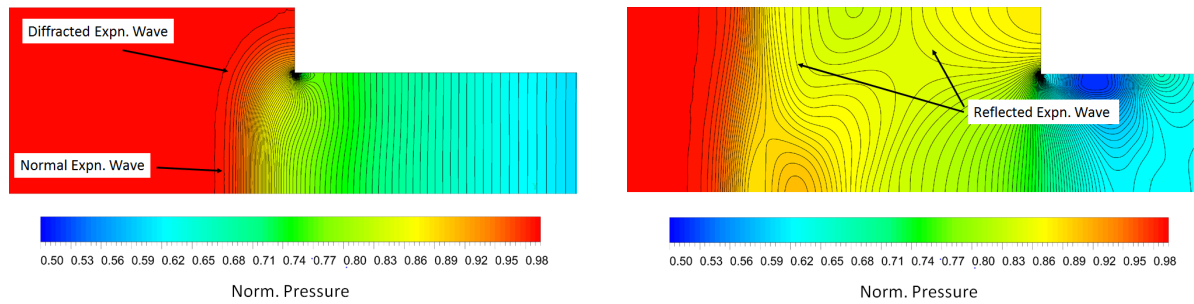


Figure 7.4: (Left) Propagation of the shock wave from the throat to the CT shown at $t = 1.8$ ms. The sudden change in diameter between the two sections causes a part of the wave to diffract while the section close to the centre-line continues to propagate normal to the CT axis (Right) Reflection of the diffracted portion of the wave at the CT walls shown at $t = 3.6$ ms. The reflected waves create a system of oblique compression and rarefaction waves behind the leading shock wave. The contours shown here are for the upper-half section of the CT

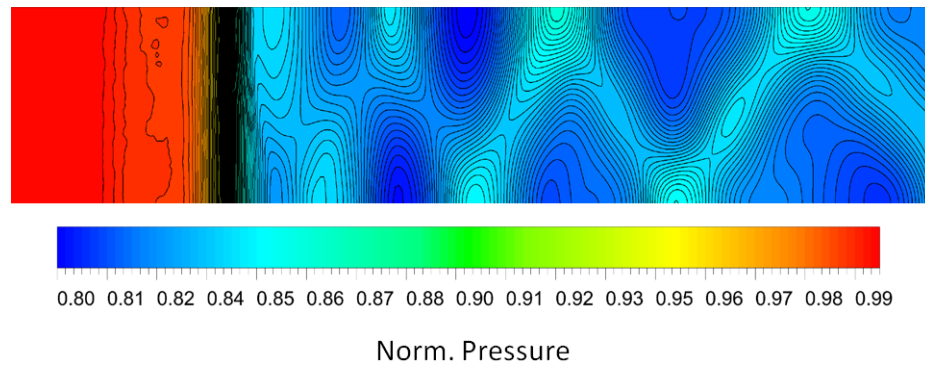


Figure 7.5: Flow field in the upper-half of the CT behind the leading RSW at $t = 5$ ms showing the system of compression and rarefaction waves symmetric about the axis that is created by the reflection of the diffracted portion of the initial expansion shock at the walls.

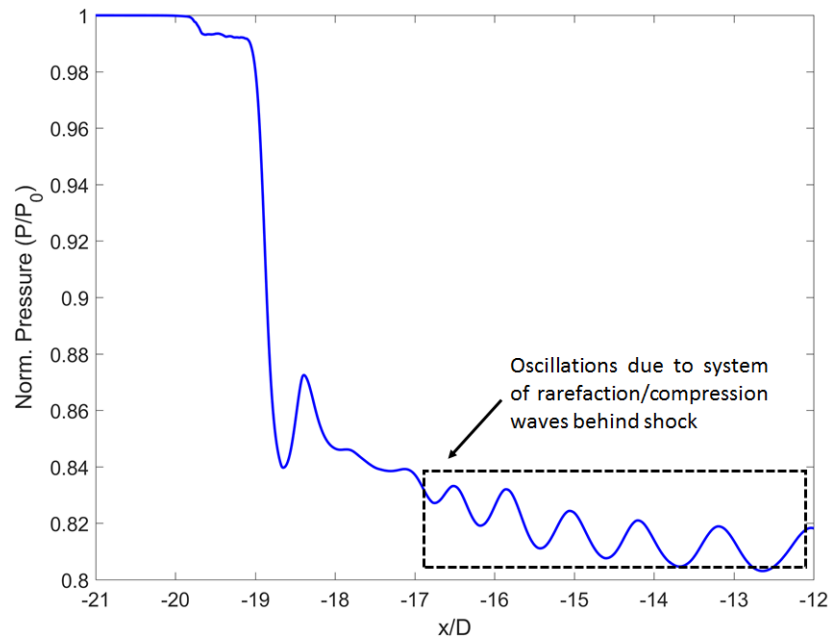


Figure 7.6: Pressure drop across the expansion wave in the CT shown at $t = 5$ ms. The oscillations observed in the post-shock pressure value occur due to the rarefaction/compression wave pattern created by the reflection of the diffracted initial wave at the CT walls.

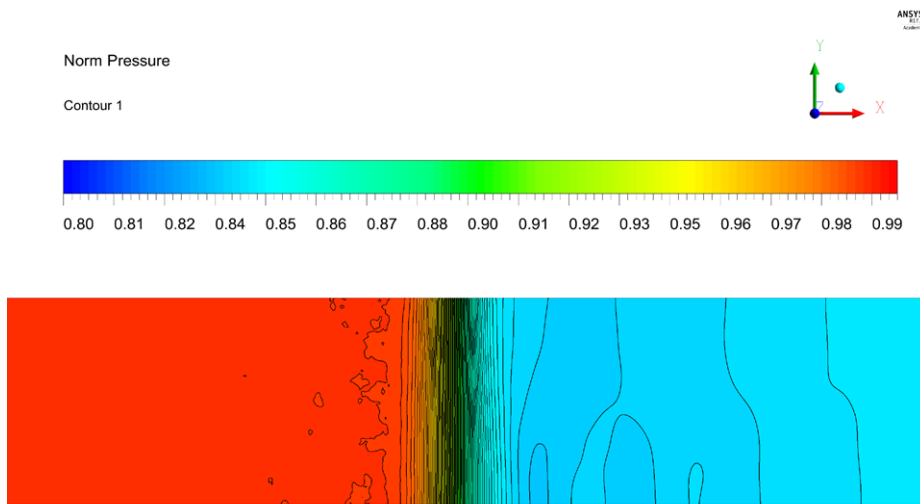


Figure 7.7: Pressure contours of flow in the upper half-section of the charge tube for the diaphragm-like expansion case. The rarefaction shock wave is clearly seen as discontinuity between the high pressure (red) and low pressure (blue) regions in the tube.

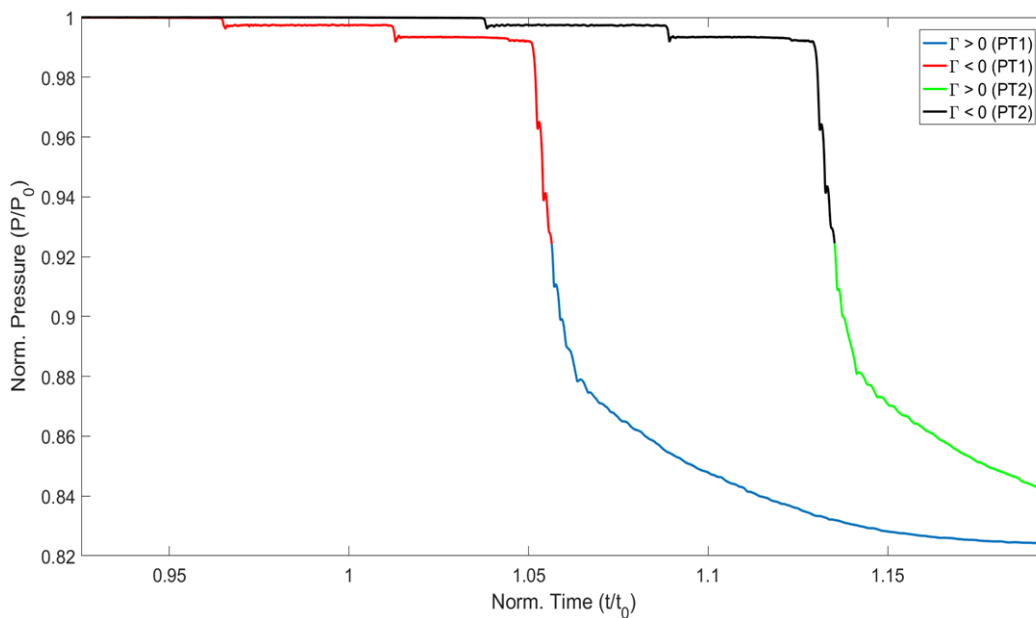


Figure 7.8: Profiles of pressure measured at sensors PT1 and PT2 for a FOV opening time of 18.13 ms. The red and black line overlays depict the $\Gamma < 0$ part of the wave. Unlike the diaphragm-like case where the pressure variation across the wave is smooth, the drop in pressure is staggered in this case with successive expansion waves in the CT denoted by the sudden jumps in pressure. The time axis is normalized by the mean time taken for the wave to travel between the sensors and the pressure is normalized by the charge tube pressure

sudden expansion. Next, it is necessary to assess the impact of the FOV motion on the shock formation. The piston motion is simulated using the equation of motion derived in Chapter 5. The pressure readings at the first pair of sensors in the shock tube and the variation of the calculated wave speed with pressure drop are shown in Figures 7.8 and 7.9. A series of expansion waves are seen to propagate one behind the other with at least two successive RSWs. The wave speed vs. pressure drop is plotted in Figure 7.9 showing two regions, the first between -0.012 and -0.031, and the second between -0.04 bar and -0.51 of the horizontal axis where the wave speed is independent of the drop in pressure. The results indicate that RSWs are formed ahead of the first pressure transducer with the new FOV design. The waves are divided into two shock waves each one

weaker than the shock formed for the diaphragm-like case. A wave Mach number of 1.022 is obtained from the CFD results which is just 0.09% off the value from the analytical model (Table 7.1). Figure 7.10 shows the contour plot of pressure at an instant where multiple expansion waves travelling into the CT can be observed.

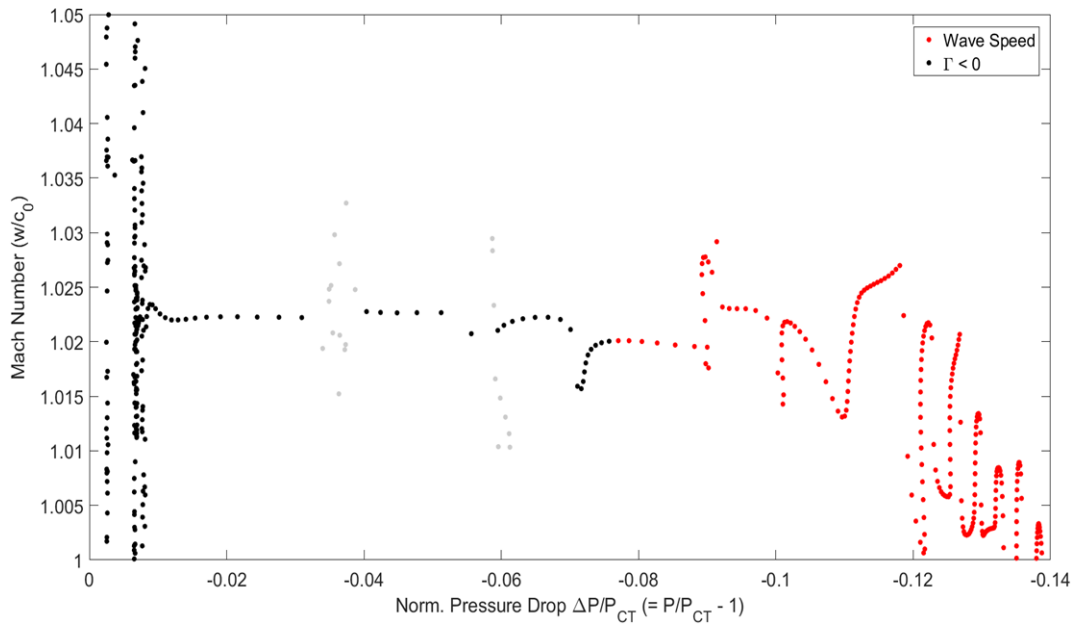


Figure 7.9: Variation of wave speed with the drop in pressure across the expansion wave for the opening time of 18.13 ms. Here, two regions of flatness can be observed signifying the presence of two RSWs in the flow

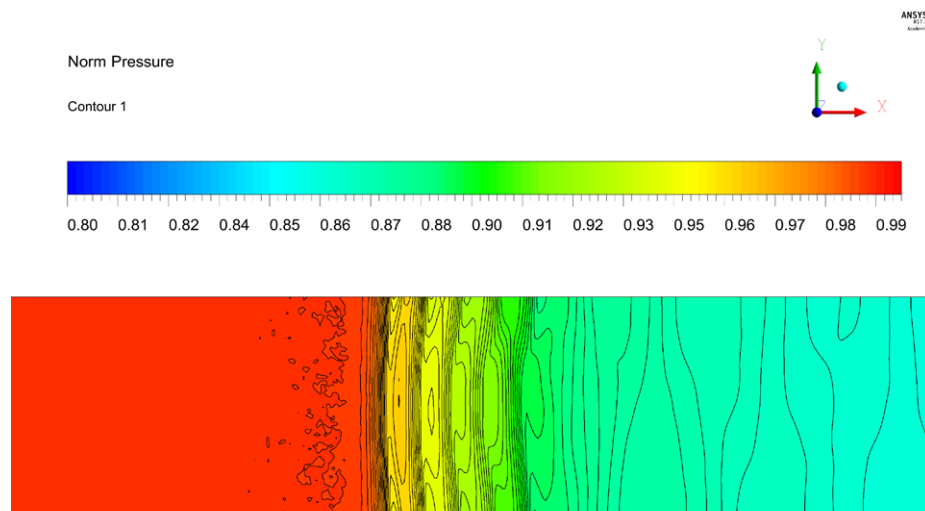


Figure 7.10: Pressure contours of flow in the charge tube for the FOV opening time of 18.13 ms. Unlike the diaphragm-like expansion case, a discernible rarefaction shock is not formed in this run but instead series of expansion waves are seen to propagate into the CT. It can be seen from the wave speed vs. pressure drop plot that the first two waves are supersonic.

One major observation from the results presented above and in Section 7.1 is the presence of multiple expansion waves in the simulations with the FOV that were absent in the diaphragm-like expansion case. The experimental conditions are identical to the diaphragm-like case suggesting that the FOV causes the splitting of the shock front into multiple waves. The results from Chapter 5 predict that the opening time of the current FOV is approx. 18.5 ms which is nearly 3.5 times larger than the design opening time of 5 ms. Simulations for the opening time of 5 ms are also performed. The results with the reduced opening time also indicate the

formation of multiple expansions in the CT. Three RSWs each travelling at a Mach of 1.021 into the CT are observed as indicated in the $w-\Delta p$ plot in Figure 7.12 and the contour plot in Figure 7.13.

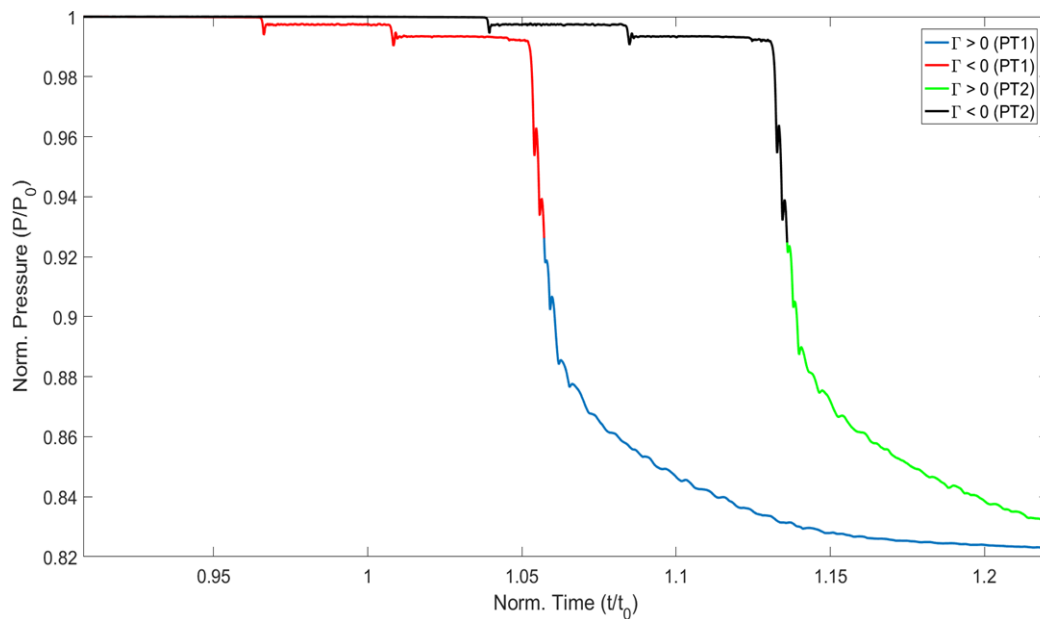


Figure 7.11: Profiles of pressure measured at sensors PT1 and PT2 for a FOV opening time of 5 ms with the red and black lines depicting the $\Gamma < 0$ part of the wave. The presence of multiple waves even in this case indicates that these are not the effect of the large opening time of the FOV. The time axis is normalized by the mean time taken for the wave to travel between the sensors and the pressure is normalized by the charge tube pressure

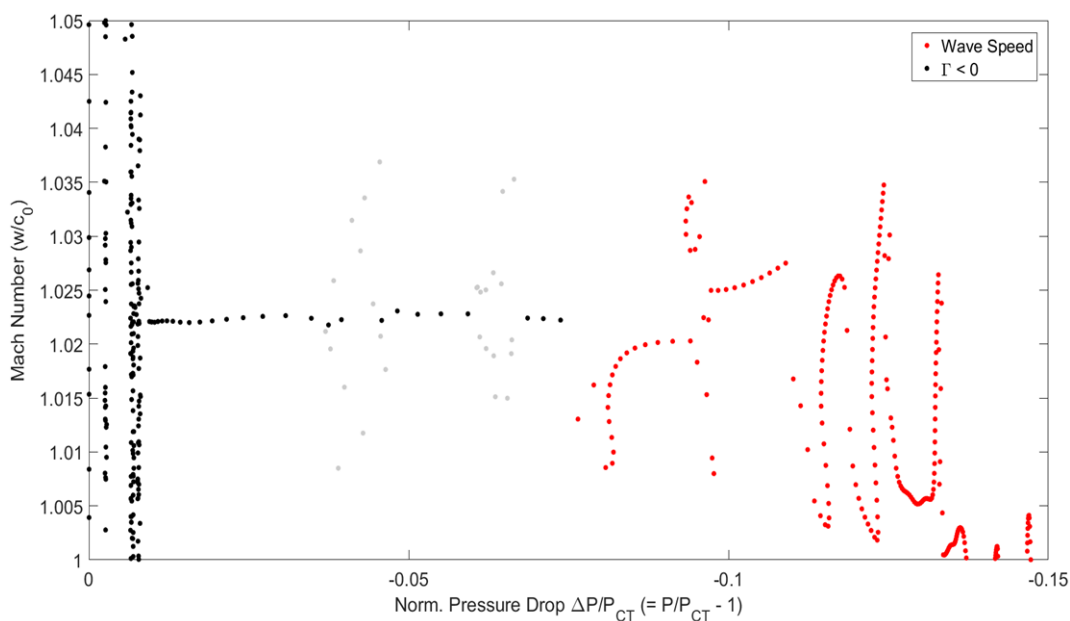


Figure 7.12: Variation of wave speed with the drop in pressure across the expansion wave for a 5 ms opening time. Three RSWs can be observed in this plot as opposed to the two for the case of the 18.13 ms opening time.

With these results, it is evident the FOV is not the only reason for the formation of multiple expansion waves. Next, grid refinements are conducted to assess the effect of mesh resolution on the solution by performing simulations of a simple shock tube with a partially opened diaphragm for the same thermodynamic initial conditions (Table 3.1) as the FAST experiment. The geometry of the shock tube is shown in Figure 7.14 where

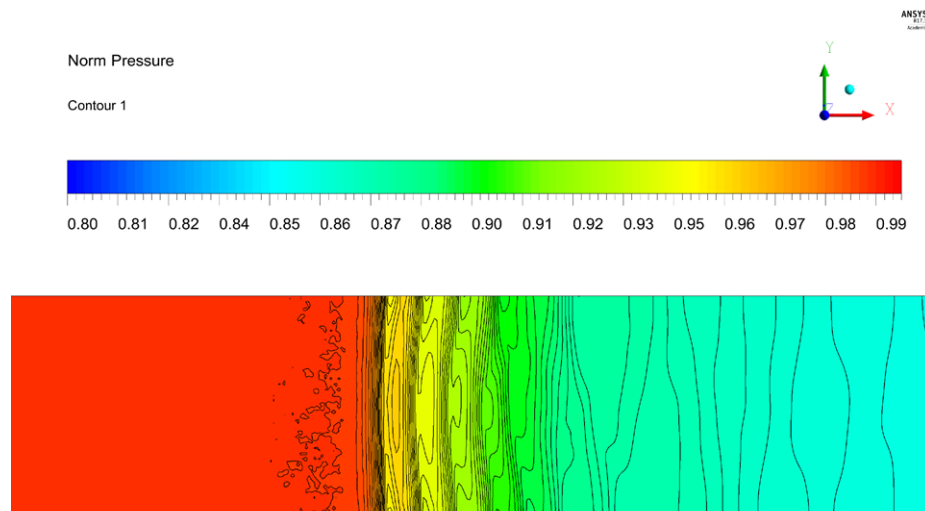


Figure 7.13: Pressure contours of flow in the charge tube for the FOV opening time of 5 ms. Similar to the 18 ms case, a series of expansion waves can be seen propagating into the CT with the first three waves being supersonic.

the diameter D is the same as the CT diameter in the FAST setup while a reduced length of 2 m is considered. The ratio of the diaphragm opening d to the shock tube diameter is taken to be 0.6.

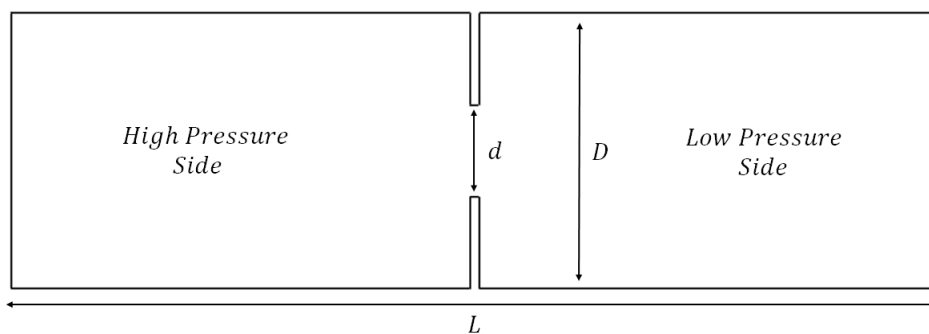


Figure 7.14: Schematic of the simple shock tube geometry that is used to study the reason for the formation of multiple shock waves. The diameter of the shock tube is 0.04 m with $L/D = 50$ and $d/D = 0.6$. The initial temperature and pressure of the fluid are the same as the FAST experiment.

The partially opened diaphragm acts as a constriction for the expansion of the high pressure gas into the low pressure section and simulates the presence of the FOV at any particular time-step. Two different meshes with 0.79 million and 1.18 million cells, referred to here onwards as Cases 1 & 2 respectively (see Table 7.1), were generated to check if the mesh has any effect on such a wave formation. The time-step of the transient simulations were maintained at $1e-5$ [s].

A similar numerical study was performed by Guardone et al. [41] for the compression shock in an ideal gas for a partially opened diaphragm case and its results are qualitatively compared with that of the shock tube simulations of Case 1 close to the diaphragm. As seen in Figure 7.15, the flow-field close to the diaphragm is similar for both the ideal and the real gas simulations. The initial expansion and rarefaction waves curve about the edges of the diaphragm and split into a normal and diffracted portion. As the wave progresses, the diffracted portion is reflected by the walls of the shock tube and the reflected shock interacts with the leading wave thereby reducing its strength. The oscillatory compression-rarefaction wave pattern described in Section 7.1 is shown in Figure 7.16.

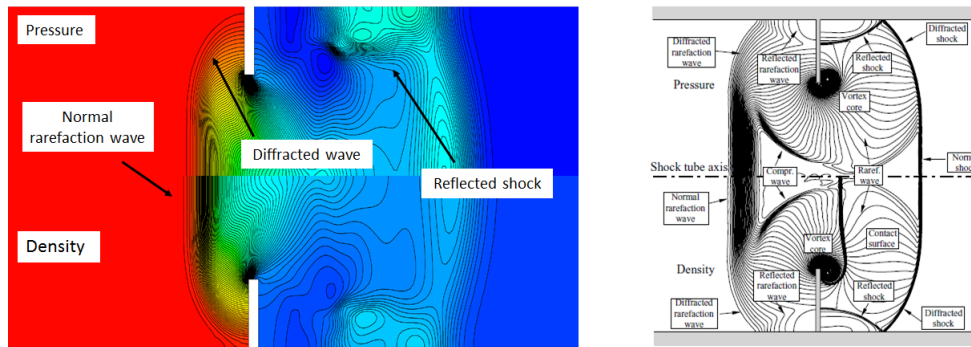


Figure 7.15: Comparison of the shock tube flow close to the diaphragm in (Left) D_6 (Case 1) and (Right) an ideal gas [41]. In both cases, the initial wavefronts can be seen to split into diffracted and normal portions at the diaphragm edges. The image is shown here only for a qualitative comparison of the flow field. The time instants of the two contours are not the same.

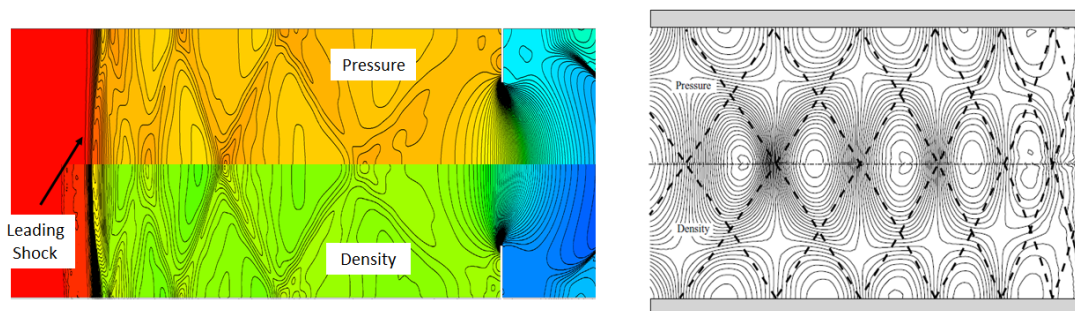


Figure 7.16: Comparison of the shock tube flow sufficiently far from the diaphragm in (Left) D_6 (Case 1) and (Right) an ideal gas [41]. The flow field is similar in both the cases with a leading shock wave followed by a system of compression-rarefaction waves. The image is shown here only for a qualitative comparison of the flow field. The time instants of the two contours are not the same.

The pressure contours of the two simulations are shown in Figure 7.17 at a time instant of 1.2 ms from the opening of the diaphragm for comparison. It can be observed here that in Case 2, a single normal expansion shock can be clearly seen propagating into the shock tube while multiple waves similar to that observed in the CT are seen in Case 1.

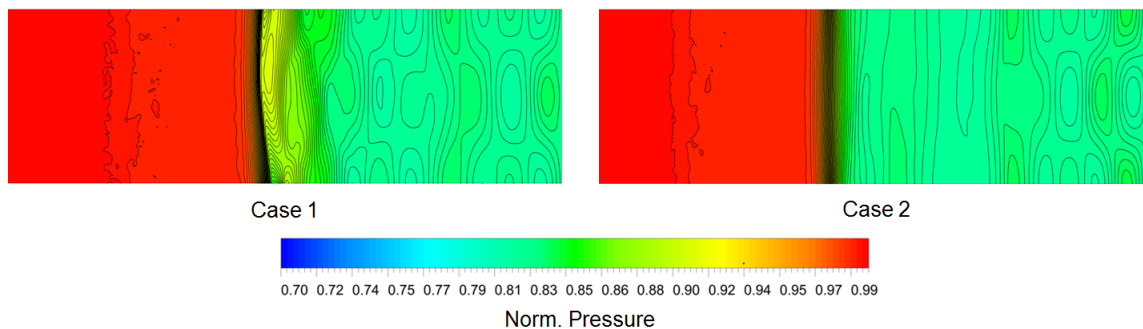


Figure 7.17: Comparison of the pressure contours of Cases 1 & 2 in the simple shock tube. The formation of multiple waves can be observed in the contours of Case 1 while a single expansion shock wave is seen in Case 2.

The propagation of the expansion wave into the shock tube is plotted at various time instances and is shown in Figures 7.18 and 7.19. The formation of the secondary expansion waves can be clearly seen in this figure as the pressure profile of Case 1 gradually becomes staggered while a smooth change in pressure is observed for Case 2. The results of this simulation suggest that the multiple shock waves are due to an insufficient grid resolution.

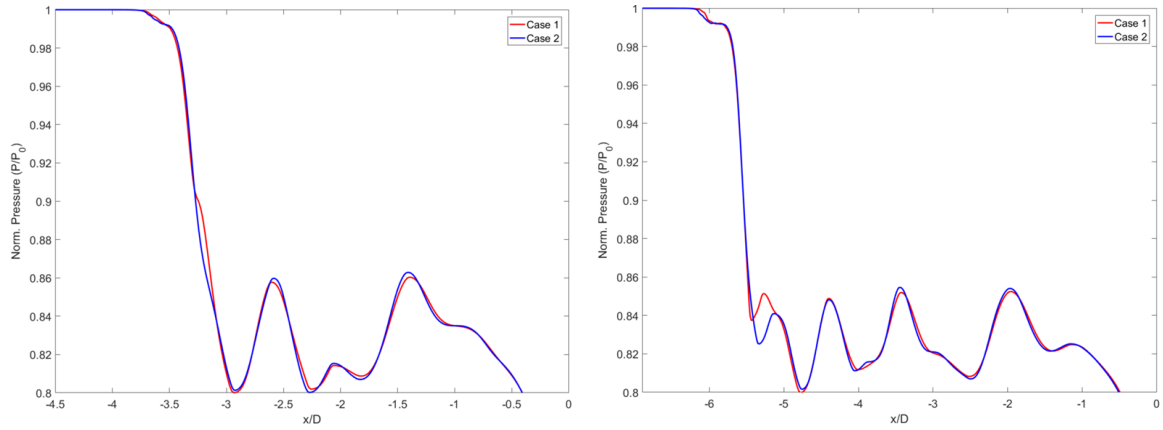


Figure 7.18: Profiles of pressure across the expansion wave for Cases 1 & 2 at time instants (Left) 2.5 ms and (Right) 4.2 ms. The variation between the two pressure profiles across the wave can be seen to gradually evolve with time. It should be noted that the pressure readings behind the wave are in good accordance with each other.

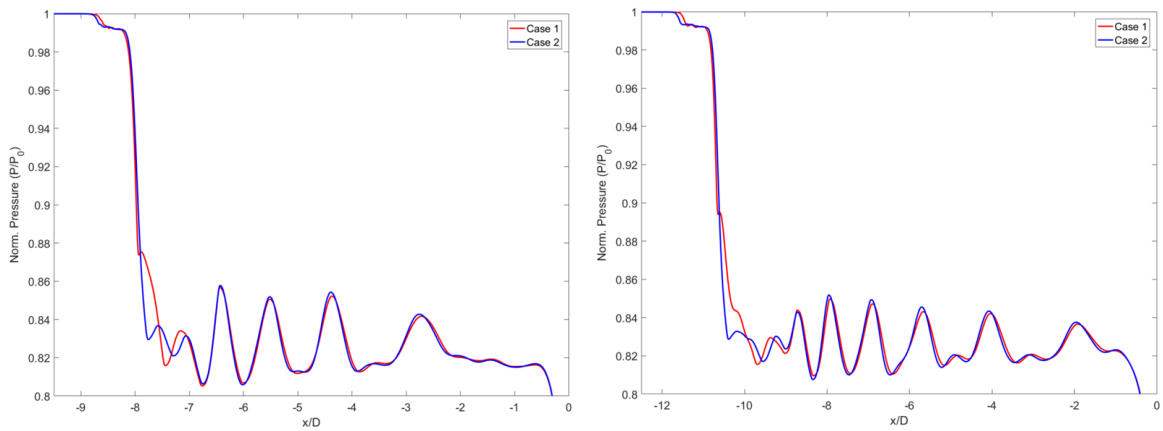


Figure 7.19: Profiles of pressure across the expansion wave for Cases 1 & 2 at time instants (Left) 6 ms and (Right) 8 ms. The expansion wave of Case 1 gradually begins to split into multiple waves which can be observed as steps in the pressure profile. On the other hand, a smooth drop in pressure is seen across the wave of Case 2.

Since the time-step was maintained a constant for both the cases, the CFL number of the two simulations were different with that of Case 1 being 0.6846 and that of Case 2 being 0.86. To understand the effect of temporal resolution on the solution, the time-step of Case 1 was increased to $1.25e-5$ [s] to match the CFL number of Case 2. A third simulation with the coarse mesh and the new time-step was performed which will henceforth be denoted as Case 3. Table 7.1 summarises the setup of the three tests cases that are simulated.

Case	No. of Mesh Elements	Time-step [sec]
1	0.79 million	$1e-5$
2	1.18 million	$1e-5$
3	0.79 million	$1.25e-5$

Table 7.1: Different shock tube simulations that are performed for investigating the effect of multiple wave formation.

The pressure contours for this analysis are shown in Figure 7.20 where they are compared with the contours of Case 2. The multiple expansion waves that were clearly visible in the pressure contours of Case 1 in Figure 7.17 are completely absent in Case 3. This result is also observed in Figures 7.21 and 7.22 which compares the propagation of the expansion wave in Cases 1 & 3 at different time instances.

It can be seen from the shock tube simulations that the multiple expansion waves disappear when the CFL

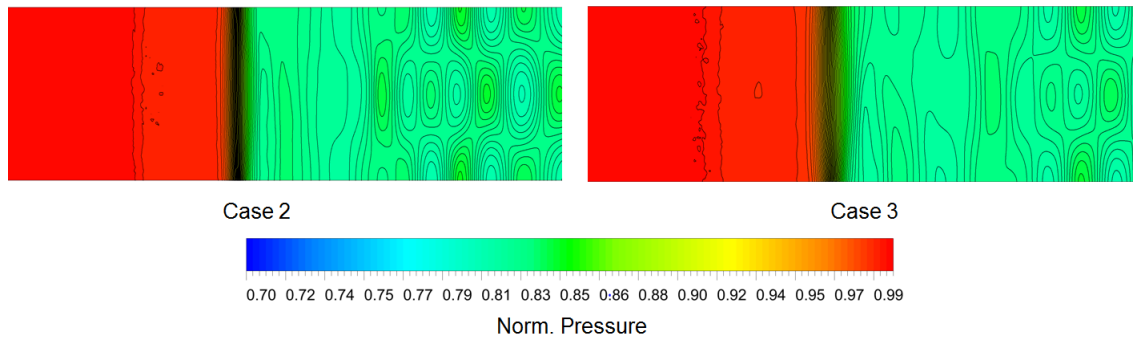


Figure 7.20: Comparison of the pressure contours of Cases 2 & 3 in the simple shock tube. Multiple expansion waves that were clearly visible in the contours of Case 1 are absent in Case 3 and are very similar to that of Case 1 with a single discernible expansion shock wave.

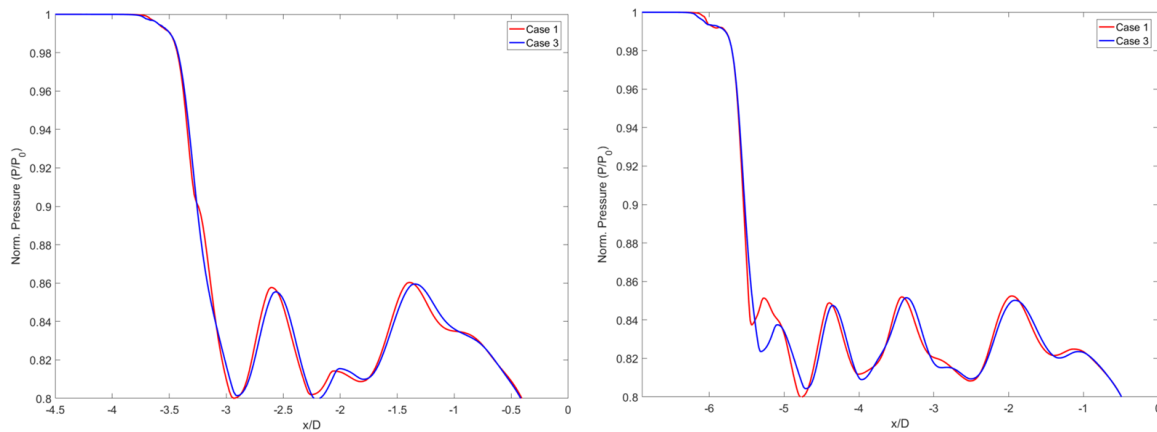


Figure 7.21: Profiles of pressure across the expansion wave for Cases 1 & 3 at time instants (Left) 2.5 ms and (Right) 4.2 ms. The similarity of the pressure profile of Case 3 to that of Case 2 suggests that the multiple expansion waves vanish when the CFL number is increased to close to 1.

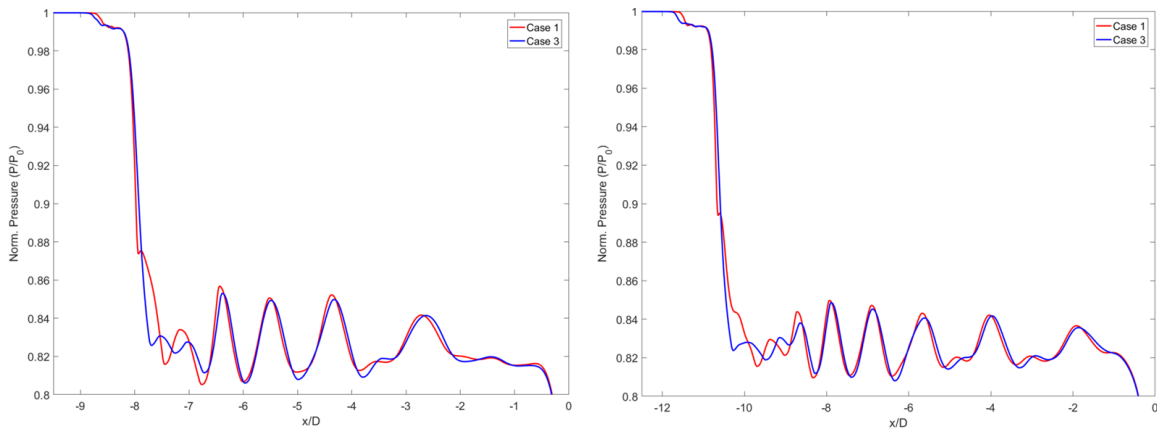


Figure 7.22: Profiles of pressure across the expansion wave for Cases 1 & 3 at time instants (Left) 6 ms and (Right) 8 ms. The smooth pressure profile across the expansion wave of Case 3 shows that the spatial and temporal resolution and has a large effect on the formation of multiple waves in the computational model.

number of the simulation is increased. This behaviour, however, is counter-intuitive since it is known that the accuracy of a numerical simulation increases as the CFL number is lowered. There is a possibility that multiple expansion shock waves are indeed generated in the FAST setup with the presence of the FOV as suggested by the simulations. However, these can be verified only with the help of experimental measurements. Thus,

even though the results in Figures 7.9 and 7.13 predict that RSWs are formed in the CT at the location of the first pressure transducer, further analyses are required to understand the effect of the spatial and temporal resolution on the solution and to correctly predict the properties of the propagating shock wave.

7.3. SUMMARY

The results of the computational simulations with and without the FOV motion were presented in this chapter. The formation of a reliable expansion shock wave was numerically shown for the diaphragm-like expansion case. The results were also found to agree with the 1D model described in Chapter 4. In the case of the simulations with the FOV motion, multiple shock waves instead of a single shock front were found to propagate into the CT. The results were compared for both the current and design FOV opening times and the waves were found to be not formed by the FOV motion. Upon further analysis using simulations of a simple shock-tube, the cause of such a wave pattern was found to be insufficient spatial and temporal resolution both of which have a large impact on the wave formation in the setup. It is therefore recommended to ensure that the computational simulations are independent of these two factors in order to get an accurate result.

8

SUMMARY AND RECOMMENDATIONS

8.1. THESIS SUMMARY

The objective of this thesis work was to numerically demonstrate the formation of a rarefaction shock wave (RSW) in the FAST experimental setup and to characterize the motion of the new design of the Fast Opening Valve (FOV). An analytical model that can evaluate the thermodynamic state behind a shock wave for given initial conditions was developed for the case of real gases. A one-dimensional model of the FOV concept design was formulated to determine its motion and its impact on the RSW formation in the CT. The FOV motion and opening time computed using the 1D model were implemented in the real gas numerical simulations and the evolution of the expansion waves in the CT was analysed for nonclassical gasdynamic behaviour. The major outcomes of this thesis work can be summarized as follows:

1. The analytical real gas model confirms the formation of a rarefaction shock wave in D6 for the chosen experimental initial conditions. These conditions have been chosen close to the saturation curve in the $\Gamma < 0$ thermodynamic region in order to maximize the strength of the RSW. It is also found that the post-shock conditions obtained using this model lie within 1% of the value reported in literature that uses another numerical method [20]. Even though this thesis uses this model to estimate only the properties of D_6 , it can be used equally for any ideal or real gas.
2. The one-dimensional model of the FOV motion suggests that the opening time of the FOV is 18.13 ms which is more than three times the design goal of 5 ms. This large opening time is mainly attributed to the presence of the auxiliary bellow which reduces the exhaust of helium from the primary bellows during its initial motion.
3. Numerical simulations of the FAST experiment performed for a diaphragm-like expansion case in D6 show the formation of a RSW at the first pressure transducer pair located at a distance of 4 m ($100D_{CT}$) from the FOV. The post-shock pressure obtained from the calculation is only 0.5% larger than the value obtained from the analytical model. The consistency of the results between the analytical model and the simulations increases the confidence in the capability of the FAST experimental facility in capturing a RSW for a diaphragm-like expansion case.

4. The results from the CFD analyses of the FAST experiment with the FOV indicate the formation of multiple RSW at the location of the first pressure transducer pair in the CT. Such a wave formation is observed for both the larger opening time of 18.13 ms and the design time of 5 ms. This suggests that the motion of the FOV and its opening time is not the sole reason for the formation of multiple waves.
5. Analysis of the flow-field in a simple shock tube shows that the formation of multiple expansion waves can be avoided by varying the grid size and the timestep of the simulation. Since such effects are observed even when the CFL number is below 1, further studies are required to define the effect of spatial and temporal resolution on the solution of the simulations.

8.2. RECOMMENDATIONS FOR THE FUTURE

Based on the conclusions above, the following topics must be explained through future research:

1. The analytical gasdynamic model developed for this thesis can estimate the thermodynamic conditions downstream of a shock wave but cannot provide information on the shock formation distance based on the FOV opening times. Though this was not of prime importance to this thesis, the model can further be developed to extract more information regarding the shock formation process.
2. The one-dimensional model of the FOV used in this thesis was developed for a preliminary analysis of the behaviour of the FOV. It can be further improved to include additional phenomena such as the thermal expansion of the piston material in the high temperature environment, effect of wall piston on the plug, effect of mass of the spring, etc.
3. The modelling of the piston motion in CFX, as mentioned earlier, was done from the breaching position rather than from the initial position of the FOV in the FAST setup. Though the evolution of the pressure waves due to the initial piston motion was modelled one-dimensionally, the accuracy of the results can further be increased by modelling the entire motion of the piston in CFX.
4. A detailed study of the effect of the mesh size and the timestep on the solution must be performed. It was shown in Chapter 7 that the effect of multiple wave formation in the shock tube occurs in both the cases for which the CFL number was less than 1. It is therefore necessary to investigate an effective method to quantify the spatial and temporal resolution of the computational model so as to understand its influence on the wave formation.
5. One of the major drawbacks of the new FOV design concept is the exhaust of helium into the LPP. It is not recommended that helium be mixed with the vapours of D6 to avoid contamination and therefore requires a redesign of the FOV.

BIBLIOGRAPHY

- [1] L. E. Singer and D. Peterson, *International Energy Outlook 2016*, **0484** (2016).
- [2] C. Lettieri, *Non Ideal Compressible Fluid Dynamics (NICFD) Enabling Science for Turbomachinery of Next-Generation Waste Heat Recovery Systems*, Tech. Rep. (TU Delft, Delft, 2016).
- [3] P. A. Thompson, *A fundamental derivative in gasdynamics*, *The Physics of Fluids* **14**, 1843 (1971).
- [4] N. Nannan, A. Guardone, and P. Colonna, *On the fundamental derivative of gas dynamics in the vapor-liquid critical region of single-component typical fluids*, *Fluid Phase Equilibria* **337**, 259 (2013).
- [5] A. A. Borisov, A. A. Borisov, S. S. Kutateladze, and V. E. Nakoryakov, *Rarefaction shock wave near the critical liquid-vapour point*, *Journal of Fluid Mechanics* **126**, 59 (1983).
- [6] S. Kutateladze, V. Nakoryakov, and A. Borisov, *Rarefaction waves in liquid and gas-liquid media*, *Annual review of fluid mechanics* **19**, 577 (1987).
- [7] S. Ferguson, T. Ho, B. Argrow, and G. Emanuel, *Theory for producing a single-phase rarefaction shock wave in a shock tube*, *Journal of Fluid Mechanics* **445**, 37 (2001).
- [8] T. Mathijssen, M. Gallo, E. Casati, N. Nannan, C. Zamfirescu, A. Guardone, and P. Colonna, *The flexible asymmetric shock tube (fast): a ludwig tube facility for wave propagation measurements in high-temperature vapours of organic fluids*, *Experiments in Fluids* **56**, 195 (2015).
- [9] N. R. Nannan, *Advancements in non-classical gas dynamics*, University of Delft (2009).
- [10] C. Zamfirescu, A. Guardone, and P. Colonna, *Admissibility region for rarefaction shock waves in dense gases*, *Journal of Fluid Mechanics* **599**, 363 (2008).
- [11] A. KLUWICK, *Handbook of shock waves*, , 339 (2001).
- [12] P. Duhem, *On the propagation of shock waves in fluids*, *Z. Phys. Chem* **69**, 169 (1909).
- [13] R. Becker, *Stosswelle und detonation*, *Zeitschrift für Physik* **8**, 321 (1922).
- [14] H. A. Bethe, *On the theory of shock waves for an arbitrary equation of state*, in *Classic papers in shock compression science* (Springer, 1998) pp. 421–495.
- [15] W. D. Hayes, *Gasdynamic discontinuities* (Princeton University Press, 2015).
- [16] L. Landau, *Em lifshitz fluid mechanics*, *Course of Theoretical Physics* **6** (1959).
- [17] E. Jackson, A. Granik, and E. Jackson, *On the possibility of rarefaction shock waves*, in *Selected Works of Yakov Borisovich Zeldovich, Volume I: Chemical Physics and Hydrodynamics* (Princeton University Press, 1992) pp. 152–154.
- [18] M. S. Cramer and R. Sen, *Exact solutions for sonic shocks in van der waals gases*, *The Physics of fluids* **30**, 377 (1987).

- [19] P. Colonna, A. Guardone, N. Nannan, and C. Zamfirescu, *Design of the dense gas flexible asymmetric shock tube*, *Journal of Fluids Engineering* **130**, 034501 (2008).
- [20] C. Zamfirescu, A. Guardone, and P. Colonna, *Numerical simulation of the fast dense gas experiment*, in *European Conference on Computational Fluid Dynamics (P. Wesseling, E. Onate, and J. Périaux, eds.)* (2006) pp. 1–17.
- [21] C. Zamfirescu, A. Guardone, and P. Colonna, *Preliminary design of the fast dense gas ludwig tube*, in *9th AIAA/ASME Joint Thermophysics and Heat Transfer Conference* (2006) p. 3249.
- [22] R. Mejia-Alvarez, B. Wilson, M. Leftwich, A. Martinez, and K. Prestridge, *Design of a fast diaphragmless shock tube driver*, *Shock Waves* **25**, 635 (2015).
- [23] I. Takefumi, K. MATSUO, and Y. YAMAMOTO, *Fast-acting valves for use in shock tubes: part 1, construction and their characteristics*, *Bulletin of JSME* **20**, 337 (1977).
- [24] I. Takefumi, K. MATSUO, and Y. YAMAMOTO, *Fast-acting valves for use in shock tubes: part 2, formation of shock waves*, *Bulletin of JSME* **22**, 693 (1979).
- [25] J. Muirhead and W. Jones, *Shock wave valves*, *Review of Scientific Instruments* **35**, 119 (1964).
- [26] H. Oguchi, K. Funabiki, and S. Sato, *An experiment on interaction of shock wave with multiple-orifice plate by means of snap-action shock tube*, in *Modern Developments in Shock Tube Research*, Vol. 1 (1975) pp. 386–391.
- [27] Y. Takano and T. Akamatsu, *A diaphragmless shock tube*, *Journal of Physics E: Scientific Instruments* **17**, 644 (1984).
- [28] M. Downey, T. Cloete, and A. Yates, *A rapid opening sleeve valve for a diaphragmless shock tube*, *Shock Waves* **21**, 315 (2011).
- [29] K. Heufer, H. Olivier, S. Drumm, and H. Murrenhoff, *A new fast acting valve for diaphragmless shock tubes*, in *28th International Symposium on Shock Waves* (Springer, 2012) pp. 535–540.
- [30] J. Randazzo and R. Tranter, *Note: An improved driver section for a diaphragmless shock tube*, *Review of Scientific Instruments* **86**, 016117 (2015).
- [31] N. D. Baltadjiev, *An investigation of real gas effects in supercritical CO₂ compressors*, Ph.D. thesis, Massachusetts Institute of Technology (2012).
- [32] D. Kouremenos and K. Antonopoulos, *Real gas normal shock waves with the redlich-kwong equation of state*, *Acta mechanica* **76**, 223 (1989).
- [33] P. Colonna and T. van der Stelt, *FluidProp: a program for the estimation of thermo physical properties of fluids*, (2004).
- [34] R. Cunningham, *Orifice meters with supercritical compressible flow*, *Trans. ASME* **73**, 625 (1951).
- [35] I. Asproulis, *RANS Modelling for Compressible Turbulent Flows Involving Shock Wave Boundary Layer Interactions*, Ph.D. thesis, University of Manchester (2014).
- [36] H. Hattori, T. Umehara, and Y. Nagano, *Comparative study of dns, les and hybrid les/rans of turbulent boundary layer with heat transfer over 2d hill*, *Flow, Turbulence and Combustion* **90**, 491 (2013).

-
- [37] A. Sarkar and R. So, *A critical evaluation of near-wall two-equation models against direct numerical simulation data*, *International Journal of Heat and Fluid Flow* **18**, 197 (1997).
- [38] D. A. Wilcox, *Simulation of transition with a two-equation turbulence model*, *AIAA journal* **32**, 247 (1994).
- [39] F. R. Menter, *Two-equation eddy-viscosity turbulence models for engineering applications*, *AIAA journal* **32**, 1598 (1994).
- [40] C. ANSYS, *reference guide, release 14.0, ansys*, (2011).
- [41] P. GAETANI, A. GUARDONE, and G. PERSICO, *Shock tube flows past partially opened diaphragms*, *Journal of Fluid Mechanics* **602**, 267–286 (2008).
- [42] N. R. Nannan, C. Zamfirescu, and P. Colonna, *Detailed Design of the Flexible Asymmetric Shock Tube (FAST) Facility at the P&E Department of the Delft University of Technology*, Tech. Rep. (TU Delft, Delft, 2007).



FLEXIBLE ASYMMETRIC SHOCK TUBE (FAST) USER MANUAL

The procedure that must be followed to conduct high temperature nonclassical gas dynamic experiments in the FAST experimental facility is described in this appendix. This manual is adapted from the report on the detailed design of the FAST facility by Nannan et. al. [42].

A.1. CHARGING THE RIG WITH THE TEST FLUID

The procedure to charge the experimental facility with the siloxane test fluid is provided in this section. These steps must be followed every time the setup is charged with a certain fluid:

1. Open the manual valves MV4, MV5 and MV6, the ball valve and the pneumatic valves PV1 and PV2. The pneumatic valves can be opened using the FAST LabView program. Close the manual valves MV2, MV3 and MV7. If the FOV is installed in the setup, then this must also be in the open position.
2. Start the vacuum pump P-1 and keep it running till the pressure in the entire setup drops to the order of 0.1 Pa. Once this level is achieved, close the manual valve MV6 and monitor the pressure level to check if it rises. If the pressure increases, this could signify either the leakage of air into the setup or diffusion of the gases that were adsorbed on the surface into the vacuumized space.
3. Heat-up the FAST setup to 150°C and start the vacuum pump again to completely remove the adsorbed gases from the setup. The water adsorbed onto the surface of the setup is also removed at this high temperature.
4. Vacuum the swagelok bottle FFC-1 until the pressure inside drops to the order of 0.1 Pa. Once this is achieved, close the manual valve MV1. This prevents the fluid in FFC-1 from flowing into the vapour generator.
5. Connect FFC-1 to the siloxane fluid container. The pressure difference between the two containers causes the fluid to be sucked into FFC-1. Once all the fluid is transferred, disconnect FFC-1.

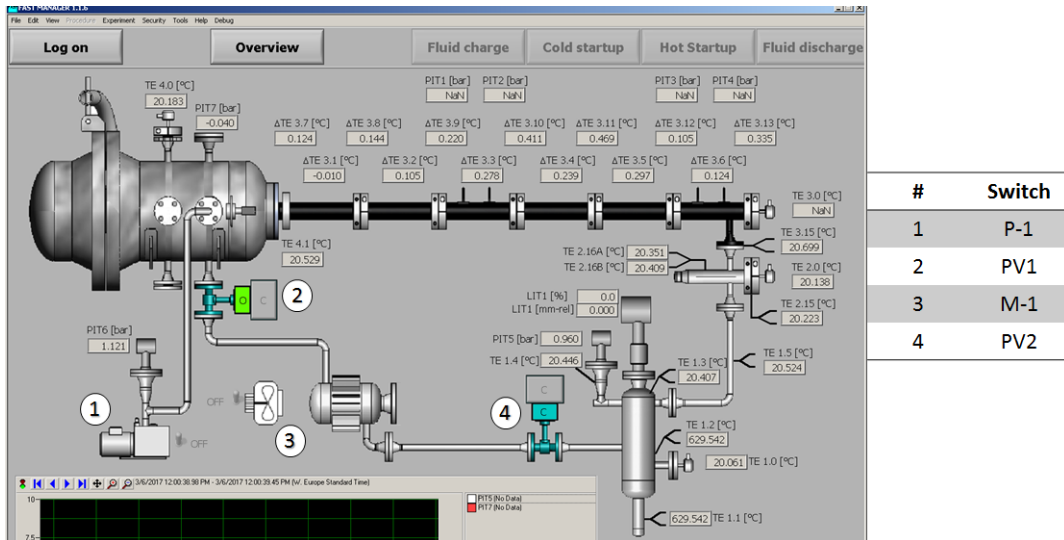


Figure A.1: Image of the manual valves MV4 (left) and MV5 (right)

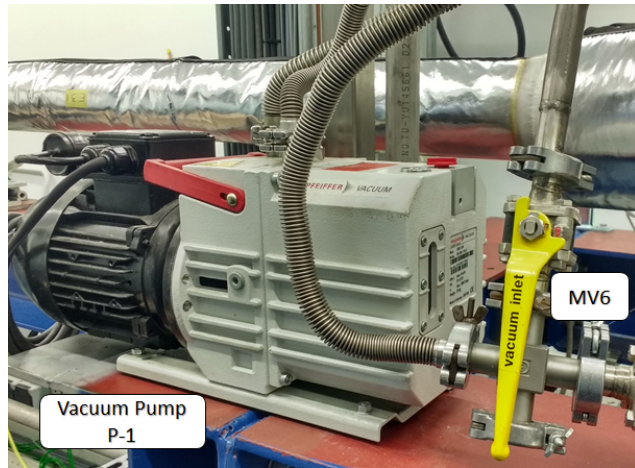


Figure A.2: Image of the vacuum pump P-1 and the manual valve MV6 (in open position)



Figure A.3: Image of the manual valves and pressure sensors MV4, PI5 (left) and MV5, PI6 (right)

- Next, immerse FFC-1 in liquid nitrogen for a few minutes till the fluid freezes. Once the siloxane is frozen, connect FFC-1 to a vacuum pump to remove the volatiles such as air that were dissolved in the fluid. Repeat this step a few times till the pressure above the frozen fluid is sufficiently low.



Figure A.4: Image showing the siloxane container (top left), the swagelok FFC-1 botte (right) and valve MV1 (bottom left)

- Connect FFC-1 to HFT-1. Open the manual valve MV2 and vacuum the system. Once this is done, either shut-down the pump P-1 or isolate HFT-1 by closing the valves MV4 and PV2. In the second case, P-1 needn't be turned off.
- After this, open MV1 so that the siloxane fluid can flow into HFT-1 under the influence of gravity as it melts.
- Once all the fluid has drained, close MV1 and MV2. FFC-1 can be disconnected from the system at this point.
- The setup is now charged with the test fluid and is ready for experimentation.

A.2. SETTING INITIAL CONDITIONS - COLD STARTUP

In this section, the steps that have to be followed to attain the initial experimental conditions for the case of a cold startup are described. Cold startup refers to the state where the fluid in HFT-1 is at room temperature. This situation is encountered especially when the rig is started for the first time.

- Isolate the vapour generator from the rest of the setup by closing the valves MV4 and PV2. Keep in mind that valves MV2, MV3, MV6, MV7 and PV1 should also be closed.
- Provide a set-point for the pressure in HFT-1 through the LabView program. This is the desired pressure that must be maintained in the CT. The control system turns on the heater E-1 if the liquid level indicator LIT1 indicates a sufficiently high fluid level in HFT-1. The control system also starts to heat

the RT, the CT and the LPP such that the temperature in the RT is 0.5-1 °C higher than that of HFT-1 and the temperatures in the CT and the LPP are the same as that in HFT-1. Siloxane vapours gradually start to develop in HFT-1.



Figure A.5: Image of the vapour generator HFT-1 (right) with the liquid level indicator LIT1 (top left) and valve MV2 (bottom left)

3. Slowly open MV4 when the set-point temperatures for both the LPP and the CT have been achieved. The siloxane vapours would now start to fill the CT and the LPP causing the pressure in HFT-1 to drop. However, since the heating continues, the pressure would rise again.
4. Close the FOV once the required pressure of approximately 1 bar is reached in the LPP. The LPP heating is now used to maintain the desired pressure. Heating of HFT-1 and the CT continues till the pressure increases to match the set value. The heating of the CT would continue till the temperature of the fluid in the CT equals the set super-heated temperature. The heating cycle continues for a long period of time in order to stabilize the temperature.
5. If the fluctuations in temperature and pressure are within an acceptable range, the experiment can be conducted. Close MV4 about a minute giving the trigger to open the FOV.

A.3. SETTING INITIAL CONDITIONS - HOT STARTUP

Hot startup refers to the condition when the fluid in HFT-1 is already at an elevated temperature. This condition usually occurs once a gasdynamic experiment has been performed. Once an experimental run is completed, the pressure in the LPP is raised from its initial value of 1 bar to a match the pressure in the CT. The procedure for attaining the initial conditions during a hot startup is as follows:

1. Start fan M-1, close the FOV and open valve PV1. The vapour from the LPP is sucked into VCT-1 owing to the fact that the condenser operates at a near-vacuum pressure. The low volatility of the siloxane fluid causes it to condense immediately in VCT-1 due to its lower temperature. Note that the wall tem-

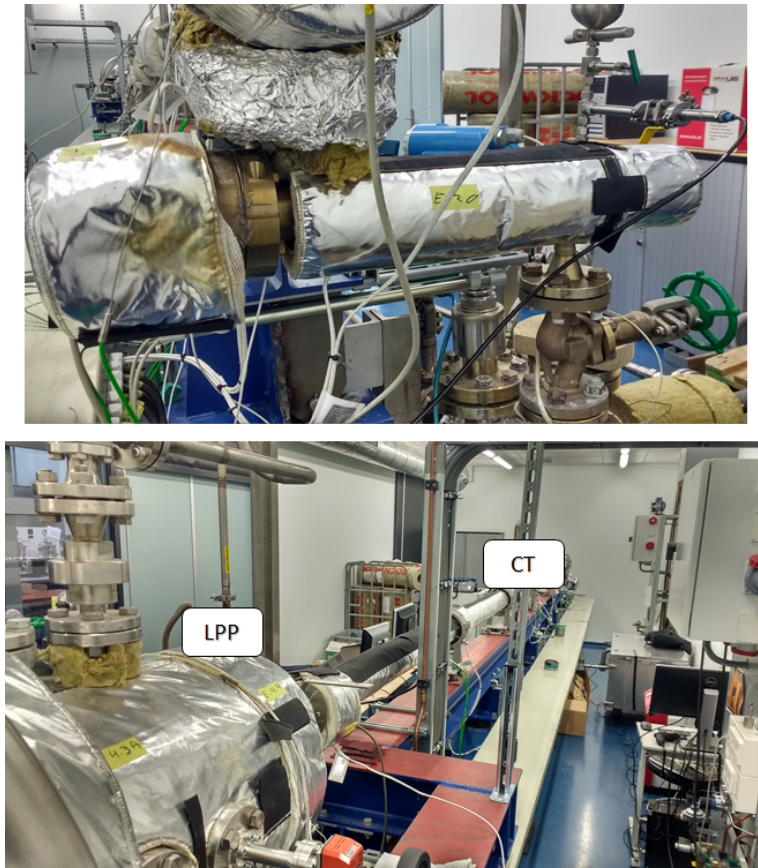


Figure A.6: Image of FAST facility showing the Reference Tube (top) and the LPP and the CT (bottom)

perature of the LPP, the CT and the RT are maintained at the same value as the initial conditions. The pressure in the LPP drops gradually due to the small size of VCT-1. Once the pressure in the LPP drops to 1 bar (set pressure for an experiment), close PV1. The remaining siloxane fluid in the condenser can be utilized in the next cold startup procedure.

2. The set-point pressure in HFT-1 can be achieved by heating provided that enough fluid is present in it. Open valve MV4 and wait till the experimental conditions are attained in the CT.
3. Once the pressure and temperature fluctuations are within an acceptable range, close off MV4 and wait for a few seconds before opening the FOV.
4. This procedure to restart the test runs can be repeated provided that there is enough siloxane fluid in HFT-1.

A.4. RUNNING A GASDYNAMIC TEST

Once the initial conditions have been reached and if they are stable over a considerable time period, e.g., at least 10 minutes, the test run can be initiated. In order to determine the formation of RSWs in the CT, it is necessary that the local sound speed in the CT can be measured prior to the experiment. Various methods to generate a weak perturbation and to measure it using the existing equipment have been devised. One such method is to hit the CT close to the adapter flange.

1. First, about 10 seconds before the opening of the FOV, record the pressures measured by PI5 of HFT-1 and PI6 on the LPP, and the temperature measured by TE3.0 on the CT. Also note down the difference in the temperatures measured by TE2.0 on the RT and TE1.0 on the HFT-1. This difference must be positive to ensure that the vapours entering the CT is superheated to the prescribed value.

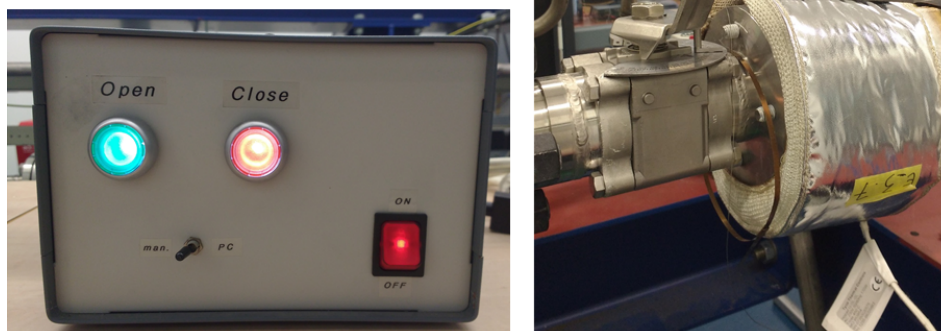


Figure A.7: Trigger Switch for FOV (left) and manual ball valve (right) connecting the LPP and the CT

2. About 1 second prior to the FOV opening, provide a trigger to initiate the simultaneous measurement and recording of the data from the dynamic pressure transducers PT1 to PT4 on the CT. The measurement is done in real time since the time difference must be recorded accurately in order to compute the wave propagation speed. It is to be noted that though the exact moment at which the FOV is open is not known, this is not an issue for the synchronized pressure transducers as only the time difference between the two signals is important. The time at which FOV is fully open can however be computed using the wave measurements in the CT.
3. The pressure data obtained from the pressure transducers can then be post-processed using a correlating algorithm to estimate the speed of the wave in the CT.

A.5. DISCHARGING OF THE SETUP

The following steps must be followed in order to evacuate the test fluid from the rig:

1. Open the FOV and switch-off the heater of HFT-1. Leave the other heaters on since this helps to remove the siloxane that has adhered on to the walls of the setup at high temperatures.
2. Turn on the fan M-1 and valve PV1. The vapours from the RT and the CT will start to flow towards VCT-1 where it will condense. The pressures in the CT, the LPP and the RT will also gradually decrease.
3. If the pressure in HFT-1 is lower than that of VCT-1, open valves MV4 and PV2 so that the liquid flows from the condenser into HFT-1. The fluid trapped in pipe 2 will also flow into HFT-1.
4. If the liquid level in HFT-1 is nearly equal to the level before the experimental run, then the other heaters can be turned off.
5. Isolate HFT-1 from the other parts of the setup by closing PV1, PV2 and MV4.
6. The siloxane test fluid can be drained from HFT-1 and removed from the setup by opening MV3.